Università degli Studi di Salerno

Dipartimento di Ingegneria dell'Informazione ed Elettrica e Matematica Applicata

Tesi di Dottorato/Ph.D. Thesis

Modelling and Experiment-Based Methods for Lithium-Ion Batteries SoH estimation

Brian Ospina Agudelo

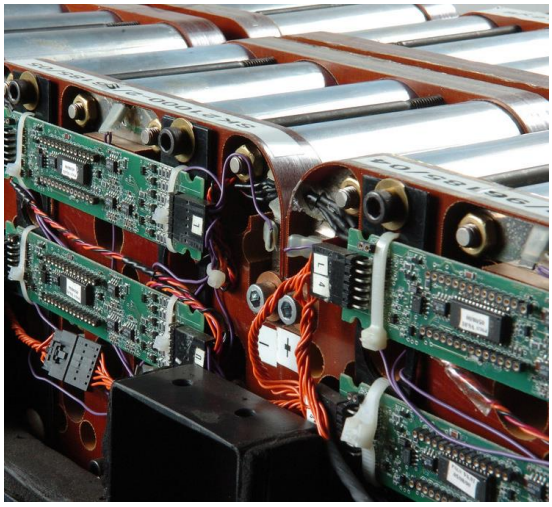

Supervisors: **Prof. Walter Zamboni & Prof. Eric Monmasson**

Ph.D. Program Director: **Prof. Pasquale Chiacchio**

Dottorato di Ricerca in Ingegneria dell'Informazione

Ciclo 34 – anno 2022

Università degli Studi di Salerno

CY Cergy Paris Université

Dipartimento di Ingegneria dell'Informazione ed Elettrica e Matematica Applicata

Laboratoire Systèmes et Applications des Technologies de l'Information et de l'Energie

Dottorato di Ricerca in Ingegneria dell'Informazione - Ciclo 34

Ecole Doctorale Sciences et Ingénierie, Spécialité: Génie électrique et électronique

PH.D. THESIS

Modelling and Experiment-Based Methods for Lithium-Ion Batteries SoH estimation

BRIAN OSPINA AGUDELO

SUPERVISORS: **PROF. WALTER ZAMBONI**
PROF. ERIC MONMASSON

JURY PRESIDENT: **PROF. GIANMARIA DE TOMMASI**

Academic Year 2021 - 2022

(Version 5.0 13th October 2022)

Abstract

This thesis addresses multiple issues regarding the on-board implementation of Lithium-Ion (Li-ion) batteries State-of-Health (SoH) estimation. Even if in the literature multiple model- and experiment-based SoH estimation methods are very well explored under laboratory conditions, their suitability for implementation in the framework of Battery Management Systems (BMSs) or battery chargers is still an open research topic.

Initially, the thesis explores the topic of on-board implementation and identification of battery impedance models. First the issue of impedance models fitting from Electrochemical Impedance Spectroscopy (EIS) data is addressed, by proposing an identification method with a suitable procedure for setting the initial values of the impedance model parameters. When tested using experimental EIS data, the method guaranties the convergence of the identification process, which is not always the case when considering fixed initial conditions, as it is typical in the literature.

Then, discrete time representations for three approaches for time domain response approximation of fractional-order battery models are proposed and evaluated in terms of performance and suitability for on-board implementation. Comparisons between the methods are made in terms of accuracy, computational burden and suitability for the identification of impedance parameters from time-domain measurements. The study was performed in a simulation framework and focused on a set of ZARC elements, representing the middle frequency range of Li-ion batteries' impedance. It was found that the multiple RC approach offers the best accuracy–complexity

compromise, making it the most interesting approach for real-time battery simulation applications. As for applications requiring the identification of impedance parameters, the Oustaloup approach offers the best compromise between the goodness of the obtained frequency response and the accuracy–complexity requirements.

Then, the Incremental Capacity (IC) analysis is proposed for characterising the capacity and the SoH of batteries aged by using cycling patterns built from current pulses with randomly selected levels and durations. The batteries are periodically characterised using a 1C charge, which is a high value with respect to the typical IC tests in pseudo-equilibrium condition. The high-current IC curves generation from raw voltage/current data includes two filtering stages, one for the input voltage and one for the IC curve smoothing, which are optimised for the application on the basis of the data characteristics. The correlations between the IC main peak features and the battery full capacity, for 28 Lithium-Cobalt oxide batteries with 18650 packaging, were evaluated, finding that the main peak area is a general feature for the evaluation of the SoH under high current tests and random usage patterns, and, therefore, it can be used as a battery health indicator in practical applications. The effects of the computational parameters on the relationship between the peak area and the battery capacity are also investigated. The results are confirmed by a further analysis performed over two additional sets of cells with different technologies, aged with a fixed driving profile and using fast charging regimes. Additionally, the performance of the peak area as a health indicator was compared with an ohmic resistance-based estimation approach.

Finally, several linear multifeature models for battery SoH estimation are proposed and their performance is evaluated. The models combine high current IC and dynamic resistance features, obtainable during partial constant current charges and discharges respectively. The models are constructed by including fixed sets of features or by applying features selection procedures based on statistical criteria. The proposed models are fitted and evaluated with data from two publicly available battery datasets, including

batteries cycled using driving and randomised profiles. During the test process, the estimation improvement introduced by each multifeature model is evaluated by computing the reduction on the mean squared error for the SoH estimation with respect to two reference single-feature models already used in recent literature. The collinearity for each model is quantified through the variance inflation factor to indicate the prediction reliability of each model. As main result of this analysis, a simple two-features model is proposed as the best compromise between estimation improvement, with respect to single feature models, and collinearity reduction.

Contents

List of Figures

List of Tables

List of publications

Journal

- Ospina Agudelo, B., Zamboni, W., Monmasson, E. **Application domain extension of incremental capacity-based battery SoH indicators** (2021) Energy, 234, art. no. 121224, https://www.sciencedirect.com/science/article/pii/S0360544221014729

  DOI: 10.1016/j.energy.2021.121224

- Ospina Agudelo, B., Zamboni, W., Monmasson, E. **A comparison of time-domain implementation methods for fractional-order battery impedance models** (2021) Energies, 14 (15), art. no. 4415, https://www.mdpi.com/1996-1073/14/15/4415

  DOI: 10.3390/en14154415

- (SUBMITTED) Ospina Agudelo, B., Zamboni, W., Postiglione, F., Monmasson, E. **Battery State-of-Health estimation based on multiple charge and discharge features** (2022) Submitted to Energy on 6th April 2022. First set of reviews received on 11th June 2022. Revised version submitted on 28th July 2022.

Conference

- Ospina Agudelo, B., Zamboni, W., Monmasson, E., Spagnuolo, G. **Identification of battery circuit model from**

EIS data (2019) Presented at Jeunes Chercheurs en Génie Électrique (JCGE) Conference 2019, Ile d'Oléron, France, 11th-14th June 2019. `https://hal.archives-ouvertes.fr/hal-02915697`

- Ospina Agudelo, B., Massi Pavan, A., Zamboni, W., Todd, R., Forsyth, A., Monmasson, E., Spagnuolo, G. **Experimental Analysis of Capacity Degradation in Lithium-ion Battery Cells with Different Rest Times** (2020) Proceedings - 2020 2nd IEEE International Conference on Industrial Electronics for Sustainable Energy Systems, IESES 2020, art. no. 9210657, pp. 44-49. `https://ieeexplore.ieee.org/document/9210657`

  DOI: 10.1109/IESES45645.2020.9210657

- (PRESENTED) Lombardi, L., Ospina Agudelo, B.,Zamboni, W., Monmasson, E. **Modeling battery aging through high-current incremental capacity features in fast charge cycling** (2022) Presented at ELECTRIMACS 2022, 14th International Conference of TC-Electrimacs Committee, Nancy, France, 16th-19th May 2022; accepted for publication in a MATCOM Special Issue.

Chapter 1

Lithium-Ion Batteries State-of-Health

1.1 Introduction

1.1.1 General Context

In order to mitigate the consequences of climate change, it has been estimated by the Intergovernmental Panel on Climate Change that it is necessary to halve the global greenhouse gas emissions by 2030 and to reach net-zero emissions by mid-century [1]. Two of the main strategies that may help to reach such goals are: the increase of electrification in the transport sector, including the migration towards electric vehicles (EVs), and the shift towards renewable power generation, mainly in the form of solar and wind plants.

The need for storing energy is one of the main issues that need to be addressed when considering EVs or power generation based on solar and wind technologies. Currently, those needs are normally met by employing battery-based energy storage systems. During the last three years, Lithium-Ion (Li-ion) batteries have represented over 80 % of the global installed energy storage capacity, placing them as the most widespread technology [2]. Li-ion technologies

tend to be favoured over others, due to their higher energy density and efficiency [3].

The main concerns about the widespread of Li-ion technologies, on high power applications, are related to the fact that they must operate between specific voltage and temperature ranges. Failing to met these requirements will lead to accelerated performance degradation and even to safety problems, as reaching temperatures over 120 °C will generate exothermic reactions, increasing the risk of fire [4]. Henceforth, a reliable Li-ion energy storage system needs to include battery management systems (BMSs) capable of monitoring the batteries operating conditions and reducing the risk factors.

Besides the thermal and power management of the battery, a BMS will also monitor the battery performance, mainly related to its usable capacity and internal resistance, and their variations over time. One of the main indicators quantifying the battery performance is known as the battery State-of-Health (SoH). This indicator is obtained by comparing the actual value of a specific battery parameter, such as the battery full capacity, with its initial value [5]. The estimation of the SoH and other battery performance indicators is an open research topic with great relevance for all integrated energy systems involving batteries, especially for their energy management and for the planning of the battery replacement [6, 7, 8]. Even if widely covered on the literature, SoH estimation is often performed considering laboratory conditions or with reliance on uncommon operating scenarios, such as full charges and discharges at low constant currents. There is still a gap concerning efforts oriented towards the implementation of SoH estimation on practical scenarios.

1.1.2 Li-ion Batteries Operation Principles and Ageing

Typically, battery cells contain four main components:

- **Negative electrode:** Often a pure metal or alloy. It gives

up electrons to the external circuit during discharge and accepts them while charging.

- **Positive electrode:** At this electrode the chemical reactions are inverted, it accepts electrons during discharge and gives them up at charge.

- **Electrolyte:** An ionic conductor that works as the medium for ionic charge transfer between the electrodes.

- **Separator:** A material that physically isolates the electrodes and prevents the direct internal conduction of electrons between them. It must be a good ions conductor but an electronic insulator.

Li-ion cells are insertion-electrode cells, meaning that, depending on the direction of the current flow, lithium is absorbed from the electrolyte and inserted into the structure of the electrode material, in a process called intercalation, or is taken from the electrode material into the electrolyte, process referred as deintercalation [3].

When a Li-ion battery is being discharged, on one side, the lithium atoms stored at the surface of the negative electrode oxidise, then the free electrons flow through the external circuit. Those lithium atoms become positive lithium ions and dissolve into the electrolyte. On the other side, the positive lithium ions that reach the positive electrode receive electrons from the external circuit. The generated neutral lithium atoms are then stored on the positive electrode structure. This whole process is reversible, meaning that the lithium ions move between electrodes during charge and discharge, with a reduction reaction taking place when the lithium is reinserted on the negative electrode during charge.

As devices designed to store and to deliver electrical charge, batteries are mainly characterised by their usable capacity Q defined as the quantity of electric charge a cell is able to hold, often presented in ampere-hour (A h). Nominally, the battery manufacturer specifies a rated value of Q, reported for the fresh cell under given operating conditions, mainly at fixed temperature and discharge

rate. The value of Q, at given operating conditions, will reduce over time due to unwanted chemical side reactions and physical changes to the components of the battery. For example, side reactions between the negative electrode and the electrolyte will lead to the creation of solid interphases between the two elements, which in term will increase the cell impedance and capacity fade over time [9]. The sum of the effects of these degradation processes will manifest as a global battery impedance increase and a decrease of the battery capacity.

Often the reduction on the battery performance due to ageing can be quantified using the SoH, which can be defined in terms of the battery capacity as:

$$\mathrm{SoH}(k) = \frac{Q(k)}{Q_0}, \tag{1.1}$$

where k is the point in time at which a new value of Q is measured or estimated and compared to the reference capacity Q_0, which can be selected as the nominal value or as the capacity at a given starting point. Ideally, the value of Q employed for the SoH computation would be measured at a reference full discharge of the battery, with fixed temperature and discharge current. During the typical usage of a battery for an EV or a stationary storage application, a full constant-current (CC) discharge is not a common occurrence. Hence, a direct measurement of the actual Q will only be available under very particular conditions, such as a reference discharge scheduled for characterisation purposes. Then, for an effective regular monitoring of Q, indirect estimations are required. They can be performed using a large variety of approaches, like model-based ones [10, 11], data-driven ones [12, 13, 14], and experiment-based methods [15, 16], as shown in several recently published survey papers [17, 18].

1.1.3 Battery Cell Frequency Response

The data obtained using electrochemical impedance spectroscopy (EIS) can be employed to analyse the impedance of battery cells

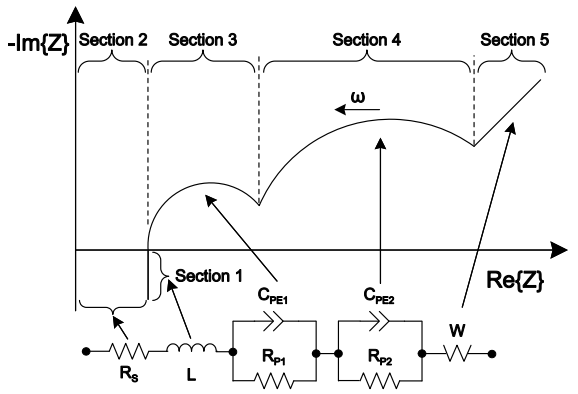

Figure 1.1: Qualitative impedance spectrum of a Li-ion cell and an equivalent circuit with ZARC and Warburg elements that can approximate it.

in a specific range of frequencies. In this way, it is possible to draw conclusions about internal electrochemical processes with different time constants. During a typical EIS test, the goal is to record the amplitudes ratio and the phase difference between the battery's voltage and current signals, which characterise the device impedance, at multiple frequencies. A general method for performing such test requires to apply a sinusoidal signal, which can be current (galvanostatic) or voltage (potentiostatic), and measuring the response (voltage for the galvanostatic case, and current for the potentiostatic case), repeating the process for all the frequencies of interest.

From the obtained battery impedance, in terms of magnitude and phase, it is possible to generate Bode plots and, by calculating the impedance real and imaginary parts, a Nyquist plot, which is often called impedance plot. If such procedure is performed for multiple battery operating conditions (temperature, SoC and DC operating point), it is possible to visualise and quantify their influences over the frequency response. For a Li-ion battery cell, a representation of a typical impedance plot is shown in figure 1.1[19].

In the qualitative impedance plot shown in Figure 1.1, it is possible to identify five sections that can be associated to particular electrochemical processes [19]. In the first part, an inductive behaviour can be seen at high frequencies, related to the inductive reactances of metallic elements in the cell and wires. The presence of an ohmic resistance is revealed by the intersection with the real axis at a non zero value. This corresponds to the sum of the current collectors, active material, electrolyte and separator resistances. The first semi-circle like section is typically associated with the solid electrolyte interface, which tends to be generated during the battery cycling. The fourth part is characterised by a second semi-circle that represents the double layer capacitance and charge transfer resistance at the electrodes. Finally, at low frequencies the main effect corresponds to the diffusion processes in the active material of the electrodes, which manifest as a section with a constant slope in the impedance plot.

It is worth noting that measured spectra often show variations with respect to the qualitative curve presented. For example the number of semi-circles can be reduced to one, or the inductive part can exhibit a slope with increments in the real part for increasing frequency. Moreover, the sections referred to as semi-circle like tend to present a depression at its mid-point (not constant radius) [9].

The form of the impedance spectrum plot can change significantly with the operating point and the ageing of the battery. Low temperatures widen both semi-circles, as consequence of slower chemical processes, and corresponding higher cell impedance. For elevated temperatures both semi-circles tend to merge. This means that the time constants of the internal processes associated with the semi-circles get closer. Moreover, it is worth noting that the real axis crossing point increases with decreasing temperature [19]. The first semi-circle does not show a significant SoC dependency. However, the radius of the second semi-circle increases strongly with the reduction of the SoC (this is especially true for SoC values under 30 %) [19]. The main effect of ageing over the frequency response of the battery is the displacement of the plot towards the

right, as a manifestation of the increase in series resistance. Some other increments in the radius of the semi-circle like sections are also reported in the literature [20, 21, 22].

1.1.4 Equivalent Circuit-Based Impedance Models

Circuital models can be used to represent the frequency response of a battery, but very often such impedance models can not be used directly for time domain simulations. In the literature, equivalent circuits like the one presented in Figure 1.1 are used for a relatively accurate and meaningful reproduction of the battery cell's impedance spectrum [23]. The behaviour of the cell at high frequencies is represented by an ideal inductor L and the resistor R_s represents the ohmic resistance of the cell elements. The two semi-circles can be represented using ZARC elements, which correspond to a parallel connection between a resistor and a constant phase element (CPE). The impedance of a CPE, Z_{CPE}, is presented in (1.2), where G corresponds to a generalised capacitance (in the literature Q is normally used, but in order to avoid confusion with battery capacity here G is employed instead), ϕ to the depression factor, ω to the angular frequency and j to the imaginary unity [24]. The response at low frequencies is represented by a Warburg element, characterised by a constant phase angle of 45° and its impedance can be represented using (1.3), in which A_w corresponds to the diffusion or Warburg coefficient [24]. It is worth highlighting that a Warburg element is a special case of a CPE, and therefore its impedance can be rewritten in the form of (1.2), as presented in (1.3). Then, $G_w = 1/(\sqrt{2}A_w)$ and $\phi_w = 0.5$ correspond to the generalised capacitance and depression factor for the Warburg impedance respectively.

$$Z_{CPE}(\omega) = \frac{1}{G\,(j\omega)^{\phi}} \tag{1.2}$$

$$Z_W(\omega) = \frac{A_w}{\sqrt{\omega}}\,(1-j) = \frac{\sqrt{2}A_w}{\sqrt{j\omega}} = \frac{1}{G_w\,(j\omega)^{\phi_w}} \tag{1.3}$$

CPEs are used instead of capacitors because, when connected in parallel with a resistor forming a ZARC element, the variations in ϕ allow to represent the depression often shown in the semi-circles of the Li-ion cell impedance plot. ϕ can take values between zero and one, when $\phi = 0$ the ZARC element represents only an ohmic resistance and with a value of $\phi = 1$ the response of a RC element is obtained. The ZARC impedance is represented by:

$$Z_{ZARC}(\omega) = \frac{R_p}{1 + R_p G\,(j\omega)^{\phi}}, \tag{1.4}$$

where R_p, G and ϕ characterise the resistance and CPE parameters.

The impedance of the circuit presented in Figure 1.1 is defined as:

$$Z_{bat}(\omega) = j\omega L + R_s + Z_{ZARC1} + Z_{ZARC2} + \frac{A_w}{\sqrt{\omega}} - \frac{A_w}{\sqrt{\omega}} j \tag{1.5}$$

where Z_{ZARC1} represents the impedance of the first ZARC element, with resistance R_{p1} and CPE parameters G_1 and ϕ_1. Similarly, Z_{ZARC2} corresponds to the second ZARC impedance, with R_{p2}, G_2 and ϕ_2 as parameters.

1.2 Capacity and SoH Estimation Methods

The SoH estimation methods presented in the literature may be classified according to the nature of the employed SoH features into the following categories:

- **Model-based methods** evaluate the SoH using the drifting of some parameters of battery models, fitted at different stages in the battery life. These models can be as simple as circuit models, used both to track the time-domain battery response under normal usage [25, 26], as well as for

frequency-domain impedance models, which have to be identified through specific experiments [27]. More complicated models, tightly linked to physics and electrochemistry principles, have been used also for SoH estimation [28]. Adopting model-based optimal state estimation techniques, such as least squares [29], Kalman filter and all its variants [10] and particle filters [11], the identification of battery parameters can also be performed online, by minimising the error between the considered model output and the operating data. Then, the identified parameters, such as the battery capacity or the model resistances, can be used for the estimation of the battery SoH [30].

- **Data-driven methods** do not require a detailed knowledge of the battery principles, nor of a battery model. Such approach is appealing for SoH estimation due to the complexity of the battery internal principles, as well as the high uncertainty on the operating conditions, which are difficult challenges to address when using model-based approaches. In this category, several methods have been implemented successfully, for instance: support vector machines [31, 32], Gaussian process regressions [33, 34], fuzzy logic [35], neural networks [36], and machine learning [37, 38]. In order to ensure an accurate SoH assessment with this kind of approach, a large amount of data, well representing a wide variety of operating conditions is required. This is the typical framework of a cloud-based centralised monitoring infrastructure, which is available in principle only in large scale applications, like EV fleets.

- **Experiment-based methods** are a third kind of estimation approaches, complementary to the previous ones. These methods do not need a battery model: they are based on measurements that can be performed during a specific stage of the battery operation or during a specific test. The measurements are aimed to find features that can be directly related to the battery SoH. This is done by analysing or

performing specific operations on selected data sections and studying the results. From this category, the length [39] or time duration [40, 41, 42] of specific operating ranges, such as voltage or current intervals, during charge or discharge appear as the most straightforward features for SoH estimation. Furthermore, additional features can be extracted from the measured data through differentiation operations, such is the case of the widely used IC and Differential Voltage (DV) analyses [43]. These techniques do not need any additional equipment beyond the usual voltage and current sensing and control, which are normally required during the battery charge and discharge cycles [44].

Table 1.1 lists the main methods and collects them into the aforementioned categories, highlighting their benefits and drawbacks. Unfortunately, in most cases the estimation methods have been only evaluated under laboratory conditions, with some of them requiring specialised tests such as EIS [20] or uncommon operating conditions, such as the low constant current charge required by traditional ICA [43]. In order to identify methods suitable for on-board implementation under common usage conditions, a review of methods implemented on automotive frameworks is presented in the following section.

1.2.1 Automotive Examples of On-Board SoH Estimation

The number of examples concerning real world applications of SoH estimation methods in the *automotive* field is very limited. This is the case due to market competition, leading to the non-disclosure by manufacturers of the methods employed on real products. Table 1.2 summarises several examples of SoH estimation methods reported in the literature and related to on-board implementation of SoH estimation techniques performed in the framework of an electric or hybrid vehicle, even if not in industrial-scale applications.

The examples listed hereinafter are based on on-board implementable approaches, and whose computations can be performed

Table 1.1: Summary of main benefits and drawbacks of the SoH estimation approaches.

Category	Methods	Benefits	Drawbacks	Considerations
Model-based	-ECM-based. -Electrochemical-based. -Least squares. -Kalman filter observer. -Particle filter.	-High estimation accuracy. -Strong robustness and scalability.	-Performance depends on the model accuracy. -Complex models will lead to high computational burdens. -The online identification of model parameters is computationally expensive. -The dependencies between the model parameters and the operating conditions need to be characterised.	-The accuracy of the online identification is limited by the characteristics of the usage data. -Often special experiments need to be considered for the model identification. -If the capacity is not directly estimated, the relationship between the models parameters and capacity needs also to be identified.
Data-driven	-Support vector machines. -Gaussian process regression. -Fuzzy logic. -Neural Networks. -Machine Learning.	-Detailed knowledge of the battery working principles is not required. -High flexibility.	-Usability limited by the lack of availability of suitable battery ageing datasets. -High computational requirements.	-The datasets required for the training need to well represent the full range of operating conditions. -The manufacturing variability between batteries of the same reference needs to by accounted for in the training datasets.
Experiment-based	-Ohmic resistance. -Impedance (EIS). -Ampere-hour counting. -Cycle number counting. -Differential voltage. -Incremental capacity	-Low complexity. -Easy to implement. -Good accuracy. -Can provide information regarding battery degradation mechanisms.	-Require of extensive characterisation processes for identifying relationships between indicators and SoH. -Often have especial operating requirements.	-Even if their implementation is relatively simple, extensive characterisation and identification processes need to be performed before deployment. -Can work as complementary methods, as they are often applied during specific stages and have low computational requirements.
	-High current incremental capacity.	-Low complexity. -Easy to implement. -Good accuracy. -Can be performed during a normal charge cycle.	-Requires of extensive characterisation processes for identifying relationships between indicators and SoH. -Information about degradation mechanisms is lost.	-As the method can be applied using the data acquired during the charge of the battery, it can work in conjunction with online methods.

on a microcontroller, or a DSP, or a single-board computer in an online fashion, that is, almost in real-time.

Internal resistance. The internal resistance has been used for years to assess the SoH of an electrochemical cell, as shown in many handbooks [45]. Such an approach is based on a direct measurement of the internal resistance, taken under specific operating conditions (e.g., with a pulsed current injection). The internal resistance is still successfully used in the literature, e.g. in [46], for the SoH assessment of a Volkswagen e-Golf by means of the identification of an electric circuit parameters. The robustness of methods based on the internal resistance estimation can be highly improved by including current steps detection, averaging filters and temperature dependencies, as illustrated in [30]. The main advantage of this method is that it is very straightforward and simple, suitable for real-time application. Moreover, it needs a small amount of data to process in order to determine the SoH from the internal resistance, and the obtained error reaches typical values of 2 %.

Kalman filter-based methods. Another class of SoH-assessment methods, widely used for EV batteries at the research stage, are the ones based on the Kalman Filter (KF). The KF is a well-known model-based optimal state estimator for linear systems, which works under very specific hypotheses. If the system is nonlinear, a linearisation process at each time step helps approximating the nonlinear system with a linear time-varying system, leading to the so-called Extended KF (EKF). Although an EKF is not necessarily optimal, it is proven to work satisfactorily for battery state estimation, especially in combination with a circuit model for the battery, or a more general state-space model. The SoH is often observed by tracking the electric resistances included in the models. Several enhancements to the filter, like the unscented or the sigma-point KFs have been successfully applied in the battery framework [47]. Sometimes, the KF-based methods are hybridised with other approaches [26]-[48]. The KF-based approaches have been applied on marketed automobiles, as in the case of the BMW i3, or on prototypes like a electric Fiat Panda [49]. Such a class of methods is characterised by a fair errors, below 5 %. Their intrinsic

closed-loop algorithm enables fast feedback. The algorithm is often developed in combination with State-of-Charge (SoC) estimation, as done, for instance, in [50].

Incremental Capacity. The ICA has been used for years to study the electrochemical properties of the cells. It is implemented basically through the differentiation of the battery capacity with respect to voltage during a full or partial charge or discharge, performed at low current levels in a laboratory environment. Some attempts have been made to bring it on-board for their intrinsic advantages: first, it is possible to extract information about battery degradation from external electrical measurements; second, the approach is suitable for describing battery ageing mechanisms over its lifetime; and third, a high accuracy is expected, with absolute errors below 1 %. This method has already been applied to vehicles produced by well-known car manufacturers, like the Nissan Leaf [4], [51], [52], the Chevrolet Volt [4], [53], [54], and the BMW i3 [52]. Furthermore, the ICA was also used in hybrid forms with the differential voltage, like for instance in the study [55]. However, the author clearly declares that the adoption of such hybrid method on a commercial scale is still a hard task, and keeps being a primary goal of car manufacturers. In is worth to notice that the ICA experiments require a low current charge/discharge phase, which is not so practical unless long stops are foreseen or programmable. But the method is definitely interesting and on-board applicable.

It is worth highlighting that all the three aforementioned sets of methods require a prior characterisation of the battery.

Data-driven approaches. Alternative methods include data-driven approaches, like for instance artificial neural networks (ANN), fuzzy logic, and Bayesian networks. They have a good estimation capability even in the presence of partial data, such as partial charges, and a good representation of battery non-linear effects, which may achieve good accuracy, with absolute errors below 2 %. Several attempts have been made to estimate battery SoH using such methods in on-board applications in [56], [57], and, [49] (such an approach is hybridised with EKF). A Bayesian Network is implemented on-board to study a car prototype based

on the BAIC EU260, produced by a Chinese car manufacturer and used for years as taxis [58]. Data-driven methods may not require a complicated model to represent a battery, but they need big training datasets and, therefore, require much more than a few characterisation tests to outperform model-based approaches.

Table 1.2: SoH estimation methods implemented on automotive framework.

EV model	**SOH estimation method**	**References**
Nissan Leaf EV	ICA	[4] [51] [52]
Chevrolet Volt	ICA	[4] [53] [54]
VW e-Golf	Discharge test (Ampere counting) and Internal resistance method (ECM fit)	[46]
Undefined BEV	Extended Kalman Filter (EKF)	[47]
BMW i3	ICA	[52]
300 BEVs 400 HEVs (unspecified)	ANN (feedforward neural network)	[56]
BAIC EU260	Bayesian network	[58]
10 FCHEV (Moby-post project)	Embedded (raw data on-board + EKF)	[26] [48]
Jaguar Land-Rover (undefined)	pOCV, IC-DV and EIS	[55]
Fiat Panda	Extended Kalman Filter (EKF) and Non-linear AutoRegressive with eXogenous input Neural Network (NARX-NN)	[49]
Volvo C30	ANN (artificial neural network)	[57]

According to the results of this review ICA is one of the main methods considered for on-board SoH estimation, but its limitations are related to the use of low current values during charge. Also the Coulomb counting between two known SoC values is still highly used. This requires of reference discharges of the battery. There is still a need for identifying methods capable of working under battery common usage, and in particular three lines of work are identified:

- When considering model based approaches, impedance models have shown to be an interesting bridge between time and

frequency domain behaviour of the batteries, allowing to characterise the battery ageing behaviour with higher accuracy. Even if observers and estimators are able to successfully identify the models parameters, little attention has been given to the implementation aspects of impedance models on time domain.

- In the case of methods such as ICA, exploration of application at conditions closer to normal usage of the battery have been performed, but always under standard CC-CV charge profiles and for very reduced numbers of batteries. A clear identification of SoH indicators at more general usage conditions is still missing.

- The combination of features extracted from different common usage conditions has not been addressed, multifeature approaches tend to rely on indicators extracted under uncommon or laboratory conditions.

Specific reviews for these particular lines of work are presented on the following section, aiming to identify possible research gaps.

1.3 Challenges for On-Board SoH Estimation

1.3.1 Challenges on Battery Modelling

State estimation and control algorithms in a BMS may require battery models capable of approximating the battery's response under given operating conditions [59]. Equivalent circuit models (ECMs) are preferred over electrochemical or empirical models, as they approximate the dynamic behaviour of a battery with relatively high accuracy [60], while offering simplified descriptions of the complex physical and chemical processes occurring within batteries, by representing them with a set of lumped elements, including resistors, capacitors and inductors. ECMs have been

widely used as parts of battery state estimation and charging control strategies. The adoption of ECM-based optimal state estimation, by directly solving the model-constrained optimisation problem [11] or using techniques such as the Kalman filter and all its variants [10], has enabled the implementation of online SoC and SoH estimations in battery systems frameworks. The implementation of online optimal charging strategies, known for their high computational burden, has also been enabled by algorithms including ECMs, by profiting from the accuracy–complexity trade off offered by such models [61].

The parameters of an ECM can be fitted from voltage and current data obtained during specific operating conditions [60]. However, these circuit components are often insufficient for modelling the dynamics of electrochemical processes such as charge and mass transfers and double layer capacitance in a battery, due to the spatial distribution of those processes [62]. This lack of physical significance may compromise the identification of relationships between health estimation and ECM parameters. Said drawback may be overcame by substituting capacitors in the ECM with CPEs, defined in the frequency domain and analytically derived from the electrochemical principles of the diffusion processes. Such elements are often used to fit EIS data [63]. The reduced number of parameters in ECMs using CPEs instead of capacitors is mainly attractive for SoH estimation approaches based on the analysis of variations in the parameters associated with specific electrochemical processes [64].

The direct time-domain implementation of such models is particularly challenging, because they represent dynamic systems with non-integer-order derivative operations, hence the name fractional order models (FOM) [62].

1.3.2 Challenges on Experiment-Based Methods

1.3.2.1 Incremental Capacity Analysis

In an IC analysis, the battery ampere-hour (A h) charge, or partial capacity, is computed using the Coulomb counting method for a charge or discharge process at *low current*, usually a fraction of the 1C current [65] (1C stands for a current whose value is numerically equal to the battery full capacity), as only at such low currents it is possible to properly identify the different electrochemical processes using IC analysis. The most significant information can be extracted from IC curves obtained at pseudo-equilibrium thermodynamic conditions, in the range of C/20 (that stands for a current equal to one twentieth of the battery capacity) [66]. Then, these data are differentiated with respect to the battery voltage, obtaining the so-called IC. The plot of IC against the battery voltage is characterised by the presence of peaks. The peak positions and areas are promising indicators for the SoH estimation [67, 68, 69], because they are very sensitive to specific electrochemical processes [70], including the various phases of the lithium ion insertion process [71] or some degradation mechanisms, like the loss of lithium inventory or active materials [72, 73, 74], and the conductivity loss [75]. As a general rule, Riviere et al. highlighted that a shift towards the right in all the peak positions can obviously be associated with an internal resistance increase [66].

The IC analysis technique is particularly useful for those batteries showing a particularly flat open circuit voltage (OCV)– SoC curve, such as the Lithium-Iron-Phosphate (LFP) cells. In this case, the IC analysis allows one to focus on the shape of the voltage curve, mainly in the curve slopes and plateaus [66].

Unfortunately, methods based on traditional ICA, performed under pseudo-equilibrium conditions [67, 68, 69], cannot be applied easily outside of a laboratory environment, as the required conditions can only be reached during laboratory tests such as a charge

process at a very low current value and for batteries aged with a uniform cycling, like a CC–constant voltage (CV) full charge/full discharge cycling profile. These conditions are rarely met in practical applications, such as smart grids or EVs. Furthermore, even for cases at which on-board EV application had been considered [66], the number of considered battery cells is always reduced.

Some authors had the intuition to go beyond the pseudo-equilibrium condition for battery diagnosis [70] or for the estimation of the capacity and SoH, extending the low current IC-based results beyond C/5, and up to 1C current, always in the presence of uniform battery cycling. For example, the area of the IC curve under one of its peaks obtained for C/3 current levels was used in [71]. Tang et al. [76] proposed to compute the IC curves at multiple degradation stages for a 1C CC charge of the battery. In [77], the peak area of the IC curve obtained with a C/2 charge current, computed in a fixed voltage range including the peaks, was used as one of the inputs to a fuzzy logic based SoH estimator. In [78], a fixed set of points including the main peak of the IC curve, extracted during a 0.75C charge, are used as the input of a capacity degradation model generated using a Gaussian process regression. For a set of batteries cycled using a fixed uniform pattern, the authors in [79] trained a support vector machine for health estimation using the peak features of IC curves obtained from a 1C charge as input. In a similar way, the authors of [80] define procedures for the estimation of the battery SoC and capacity from three specific points, namely peaks and valleys, of SoC against IC and DV curves obtained at C/2 for batteries cycled with fixed CC-CV charge and discharge profiles.

These kind of analyses are still far from being conclusive for the definition of a widely-applicable battery capacity indicator of practical interest. Two main limiting factors affect all the previously cited works using IC analysis for capacity estimation beyond low-current levels. First, very few batteries were considered (five or less), and, second, their usage pattern is always uniform among batteries, employing fixed rates during full charge and discharge ageing cycles. Therefore, the application domain of IC-related

capacity indicators, and the choice of the optimal one, still needs to be extended to batteries aged under more general usage patterns, and studied using a dataset with a higher number of batteries. The usage pattern could be far from the pseudo-equilibrium condition characterising typical laboratory tests.

1.3.2.2 Experiment-Based Multifeature Models

Experiment-based approaches are particularly interesting for on-board implementation, because they employ features extracted from the operating data and allow to develop models for Q estimation with low complexity, making them easy to implement and to interpret. They exploit the correlation between Q and features extracted from voltage, current and/or temperature data during specific usage stages. For instance, time durations of the CC charge over fixed voltage ranges have been explored as easy to extract SoH indicators [81]. Another well-known feature, is the dynamic resistance computed at fixed time intervals during a discharge current step [79, 82]. A family of features often mentioned in the most recent literature, are the IC features, such as the area under the main peak of an IC curve, which is obtained during a partial CC charge of a battery [15, 16]. Furthermore, the parameters of voltage-capacity models for IC curves have been recently explored as accurate SoH indicators [83]. Sometimes, features coming from different usage stages are used together in multifeature approaches [84, 85]. Despite their good accuracy, the on-board application of multifeature approaches is very limited at present.

In recent past, each feature has been used as an individual capacity indicator, obtaining single-feature models with acceptable estimation errors [15, 82]. Recent literature efforts are targeted to improve the estimation accuracy by using multiple Q indicators at once. The study in [85] considers 0.5C IC features as health indicators. These features are used for training and testing a Support Vector Regression (SVR) model for SoH estimation for 2 batteries on the *PL Sample CALCE dataset* [86]. RMSE with values under 1 % were obtained. Models based on multiple features

extracted from IC curves have also been proposed in [84, 78]. Mean RMSE results of 1.18 % were reported in [84] for 4 batteries from the *CS2 Battery CALCE dataset* [87]. For 4 batteries in the *NASA Battery Data Set* RMSE results in the order of 0.02 Ah are reported by [78]. The results in these works may be limited by the use of features coming from the same usage stage, namely a CC charge, and by the high uniformity in the cycling of the considered batteries.

The mean, maximum and minimum values of the charged capacity and temperature during different voltage ranges are considered as SoH indicators by the authors of [88]. A genetic algorithm (GA) is employed for feature selection and a SVR is used for SoH estimation. The method is tested for 3 batteries from the *Toyota Research Institute fast charging dataset* [89], obtaining a RMSE of 0.24 %. Even if these results are promising in the framework of Q estimation for batteries cycled using fast charging, the approach needs to be evaluated on a higher number of batteries. Paper [90] proposes three parameters from a model for the battery voltage during a reference CC charge as residual capacity indicators. A SVR model is evaluated using the charge voltage curves for 920 batteries retired from EVs (not available publicly). RMSE values for residual capacity estimation of the order of 2.2% are obtained. This study stands out due to the number of involved batteries, but is limited due to the fact that a reference discharge is required, as the proposed method is aimed as a characterisation experiment after retiring the batteries from their application.

Paper [91] considers multiple health indicators: the charged capacity, time duration and area under the temperature curves during both the CC and also CV stages of the battery charge. Features selection is performed by applying grey relational analysis and further dimensional reduction is obtained by using principal components analysis. These features are used for training and testing a Relevance Vector Machine (RVM) for the batteries on the *NASA Battery Data Set* [92]. The study considers a total of 18 batteries, which is a step up in terms of statistical units with respect to previous works, but the models are tested by employing

either single batteries or groups of three batteries. In general, they achieved capacity estimation errors under 10 %. Even if a fair accuracy is reached, considering the number of analysed batteries, the practicality of the resulting models is reduced by the dependency of the employed features on full CC-CV charges.

Lin et al. proposed a multi-model fusion approach for SoH estimation. The fused models are a multiple linear regression (MLR), SVM and GPR [93]. The three models are combined using a random forest regression (RFR). The considered features include: the voltage values and slope in a given time interval, and the peaks of the differential temperature and IC curves during a CC charge. The approach is evaluated on the *Oxford Battery Degradation Dataset 1* [94], using a leave-one-out cross-validation procedure. In general mean absolute error and RMSE results are under 1 % for the proposed approach.

Table 1.3 summarises the features introduced in the literature discussed above. IC features are the most widely adopted Q indicators, being used alone [85, 84, 78] or mixed with voltage and temperature features [93]. For models including such features, the performance evaluation is done using the data from a limited number of batteries, between 2 and 8 batteries, with highly uniform cycling profiles. Only the work presented by [90] considers a high amount of batteries, 920 decommissioned cells, but the capacity estimation method is developed in the framework of laboratory characterisation for second life applications, relying on a model fitted during a battery full charge. The approaches presented by [91, 93] mix features coming from different sources, namely different charge stages or type of signals, but the results are severely limited by the dependency on a full charge or the number and variety of the considered batteries respectively.

Such approaches achieve a good accuracy in capacity estimation by employing models with multiple features extracted from battery cycling data. However, three major issues limit their applicability on-board battery systems. First, most of the features depend on data from full charge or discharge cycles, making it difficult to extract them from normal usage data. Second, the models

Table 1.3: Summary of literature works on the topic of multiple features based battery capacity estimation

Ref.	Q model	Features	Set of batteries	Results
[85]	SVR	0.5C IC main peak height, position, area and energy	2 batteries on the *PL Sample CALCE dataset*	Average relative errors under 1 %
[84]	multi-kernel RVM	0.5C IC main peak height and area	4 batteries from the *CS2 Battery CALCE dataset*	Mean RMSE results of 1.18 %
[78]	GPR	0.75C IC main peak height, IC at 3.8 V and the slope and intercept of a linear fit for the IC curve between 3.8V and the main peak	4 batteries in the *NASA Battery Data Set*	RMSE results are in the order of 0.02 *Ah*
[88]	GA + SVR	Range and mean of Q_c and temperature in specific voltage ranges	3 batteries from the Toyota dataset	RMSE results down to 0.23 %
[90]	SVR	3 parameters from a mechanistic model for the voltage during a reference CC charge	920 retired batteries	RMSE for residual capacity estimation of the order of 2.12%
[91]	RVM	Charged capacity during CC, CV and CC+CV. CC and CV durations and their ratio. Area under the temperature signal during CC, CV and CC+CV. Ratios between temperature areas and their respective charged capacity	18 batteries from the *NASA Battery Data Set*	RMSE in the range of 0.014 - 0.042 *Ah*
[93]	RFR: MLR+ SVM+ GPR	Voltages after 200 and 500 s of the CC charge and the slope between those points. The peak and valley values of the differential temperature, and the voltage difference between those points. The main peak of the IC curve	8 batteries from the *Oxford Battery Degradation Dataset 1*	RMSE in the range of 0.42-0.86 %

are normally trained and tested using the data of few batteries, typically between 1 and 4. Finally, usually the considered batteries share laboratory cycling profiles, which highly limits the extension of the obtained results to real battery usage profiles.

1.4 Thesis Overview

The overview of recently published works on Li-ion batteries SoH estimation, presented on the precedent sections, revealed some critical issues when considering methods employing battery models and features that can be extracted during the battery normal usage.

In the case of model-based estimation methods, recently, FO impedance models have been adopted for the representation of the battery electrical behaviour. Such models, are still ECMs that include CPEs, defined in the frequency domain and analytically derived from the electrochemical principles of the diffusion processes [63]. FOMs represent a compromise between the lack of physical significance often encountered when using simpler equivalent circuit models, and the higher computational complexity of electrochemical models. FO models have been successfully used for SoH estimation in laboratory, often using computers for the model implementation, but little consideration has been given to how to implement such models on embedded systems suitable for on-board applications. This issue is addressed in Chapter 2, where three approaches for the implementation of the time domain response of FOMs are proposed and compared in terms of accuracy, complexity and suitability for parameters identification from time domain data. Additionally, when facing the problem of identifying impedance models directly in the frequency domain, there is still a lack of consensus on how to assign the initial values of the model parameters. Such decision is critical for the convergence of the identification processes and very often it is performed manually, limiting the applicability of EIS identification on automated characterisation campaigns. This issue is also faced on Chapter 2, where a method for the definition of the initial values is proposed.

Multiple methods for the analysis of the battery behaviour such as ICA and EIS are successfully used as battery diagnosis tools on laboratory environments. Unfortunately, these methods are not applicable when the batteries operate under cycling conditions typical of EV or stationary applications, mainly due to their specific operational requirements. In particular the success of ICA analysis for battery diagnosis depends on charging or discharging the battery using a very low constant current after a long rest period, conditions that will be rarely met on real applications. Recently some authors have considered employing higher currents [70, 71, 76, 77, 78, 79, 80], in order to make ICA suitable for battery performance assessment on-board, but those studies are limited to reduced sets of batteries under standard cycling profiles. The work presented on Chapter 3 aims to extend the applicability of ICA as a tool for on-board SoH estimation when considering batteries aged using profiles closer to real applications such as randomised cycling and fast charging scenarios.

Finally, Chapter 4 proposes several simple linear models that combine multiple features extracted during normal usage of the battery, including ICA and internal resistance features. Even, if similar models have been considered on the literature, they often rely on features that could be extracted with little periodicity on real applications, as they use the data from full battery charges and discharges. Evaluating models with features that could be extracted under common usage conditions enables a more consistent SoH monitoring over time.

Chapter 2

Battery Frequency and Time Domain Modelling for State-of-Health Estimation

Impedance models including CPEs are of particular interest for SoH estimation, as they are ECMs capable of accurately representing the battery frequency response. Such characteristics allow their use for bridging information coming from time and frequency domains. On the one hand, an impedance model fitted using frequency domain data, such as EIS spectra, can be used directly to represent the battery dynamic response to a particular current profile [23]. On the other hand, the parameters of the impedance elements identified from time domain data can be used to analyse the frequency domain response of the battery, which has been extensively linked to specific electrochemical processes in the literature [9, 95]. From the SoH estimation perspective, impedance models have been exploited using two approaches:

- After a characterisation process for the specific application, the relationships between impedance parameters, such as the model resistances, and SoH can be exploited for estimation. This requires a periodic estimation of the impedance model parameters at specific operating conditions, which can be

performed using frequency or time domain data. Such approach is often performed on laboratory conditions due to the need for EIS data at fixed SoC and rest conditions or the lack of methods for the implementation of FOM on-board [95].

- The implementation of state observers such as the EKF has previously allowed the on-board estimation of SoC and SoH [96, 97]. The most commonly used models are multiple RC ECMs, as their state space representation is very well known, but such models can fall short in representing the frequency domain response of the battery, often requiring multiple RC elements in series in order to fully capture the dynamics of the electrochemical processes on the battery, which may lead to model identification issues [98]. Recently FO and electrochemical models have been considered for use with state estimators, but their implementation on-board is still an open research issue.

For the first estimation approach, the accurate identification of the impedance model parameters is of paramount importance, when using either frequency or time domain data. When starting from frequency data, for the identification, a suitable selection of the initial values of the parameters has shown to be one of the critical issues for a successful identification [24]. This issue, is addressed on Section 2.1 of this chapter, where a fitting method with a suitable selection of the initial values is proposed and evaluated. Conversely, when the aim is to fit impedance FOMs from time domain data, there is still a lack of a clear method for their numerical implementation on-board, regardless of the recent interest on FO states observers [64]. Section 2.2 proposes three sets of state equations for the implementation of FOMs using different approximation methods: multiple RC, Oustaloup and Grünwald–Letnikov. The three implementation methods are then evaluated and compared in simulation, in order to identify their suitability for on-board implementation.

2.1 Method for the Identification of Battery Impedance Models from EIS Data

The implementation of an impedance model and a curve fitting procedure of its parameters are presented in this section. The proposed curve fitting procedure is based on the minimisation of the distance, in the complex plane, between the measured impedance and the impedance model. In this kind of procedures the selection of an adequate initial set of parameters is important, for convergence reasons. A set of initial model parameters is proposed, which improves the convergence of the procedure.

In order to simplify the implementation of the proposed fitting procedure, the impedance presented in (1.5) can be separated into its real and imaginary parts as follows:

$$\begin{aligned}\mathrm{Re}\{Z_{bat}(\omega)\} = R_s &+ \frac{R_{p1} + R_{p1}^2 G_1 \omega^{\phi_1} \cos\frac{\phi_1\pi}{2}}{a_1(\omega)} \\ &+ \frac{R_{p2} + R_{p2}^2 G_2 \omega^{\phi_2} \cos\frac{\phi_2\pi}{2}}{a_2(\omega)} + \frac{A_w}{\sqrt{\omega}} \qquad (2.1)\\ \mathrm{Im}\{Z_{bat}(\omega)\} = L\omega &- \frac{R_{p1}^2 G_1 \omega^{\phi_1} \sin\frac{\phi_1\pi}{2}}{a_1(\omega)} \\ &- \frac{R_{p2}^2 G_2 \omega^{\phi_2} \sin\frac{\phi_2\pi}{2}}{a_2(\omega)} - \frac{A_w}{\sqrt{\omega}} \qquad (2.2)\end{aligned}$$

in which a_1 and a_2 can be obtained by replacing i for 1 or 2 in (2.3) respectively.

$$a_i(\omega) = \left(1 + R_{pi} G_i \omega^{\phi_i} \cos\frac{\phi_i\pi}{2}\right)^2 + \left(R_{pi} G_i \omega^{\phi_i} \sin\frac{\phi_i\pi}{2}\right)^2 \qquad (2.3)$$

The equations for the real and imaginary parts of the impedance of the circuit presented in Figure 1.1 were implemented in Matlab®

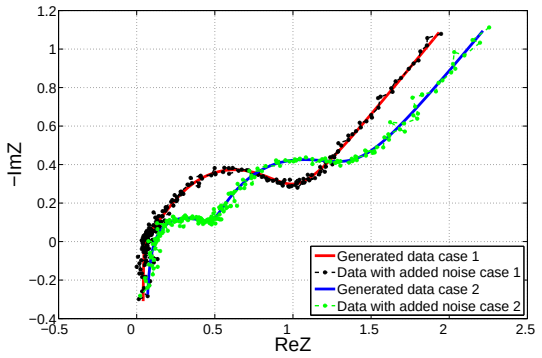

Figure 2.1: Impedance plots generated with the implemented model for two different sets of parameters.

using some parameters values within the ranges reported in the literature [99]. These kind of data, generated by simulation, may be useful for tests of identification algorithms. The addition of Gaussian noise to the data can be considered in order to get a better simulation of experimental data. Figure 2.1 presents the impedance plots generated using the implemented impedance model in the range of frequencies 10m-10k Hz for two different sets of parameters, introduced in Table 2.1. The curves obtained in both cases after adding Gaussian noise with a signal to noise ratio of 30 dB are also included in Figure 2.1. It is worth highlighting that a next step in this regard could be to add temperature, SoC, electric operating point and ageing dependencies to this model. Such improvements would allow to generate impedance plots for a given cell under multiple operating conditions.

Table 2.1: Parameters used for the generation of Nyquist plots with the implemented impedance model

Case	L (μH)	R_s $(m\Omega)$	R_{p1} $(m\Omega)$	G_1 (Ss^{ϕ_1})	ϕ_1	R_{p2} $(m\Omega)$	G_2 (Ss^{ϕ_2})	ϕ_2	A_w $(m\Omega/\sqrt{s})$
1	5	38	167.5	0.235	0.62	650	0.139	0.9	270.8
2	5	38	450	0.02	0.62	650	0.4	0.9	270.8

2.1.1 Circuit Parameters Estimation Procedure

The parameters of the circuit-based impedance model can be estimated by making use of a curve fitting procedure of equations (2.1) and (2.2) to experimental impedance data, obtained by performing an EIS test for a given set of cell operating conditions. A least squares-based fitting procedure was implemented in order to estimate the value of the parameters of the circuit in Figure 1.1 from experimental impedance results.

The proposed procedure works on data obtained from an EIS test performed for a set of N frequency values:

$$\boldsymbol{\omega} = \begin{bmatrix} \omega_1 & \omega_2 & \cdots & \omega_N \end{bmatrix}, \tag{2.4}$$

where the frequencies ω_i are sorted in an increasing order. The data obtained during the EIS test can be organised in a matrix as follows:

$$\mathbf{Y} = \begin{bmatrix} \boldsymbol{z_1} & \boldsymbol{z_2} & \cdots & \boldsymbol{z_N} \end{bmatrix} = \begin{bmatrix} Re_{z_1} & Re_{z_2} & \cdots & Re_{z_N} \\ Im_{z_1} & Im_{z_2} & \cdots & Im_{z_N} \end{bmatrix} \tag{2.5}$$

where z_i correspond to the impedance measurement taken at frequency ω_i with real and imaginary parts Re_{z_i} and Im_{z_i} respectively. Considering the model of the real and imaginary parts of the impedance:

$$\boldsymbol{Z_{bat}}(\omega, \boldsymbol{\theta}) = \begin{bmatrix} Re_{bat}(\omega, \boldsymbol{\theta}) \\ Im_{bat}(\omega, \boldsymbol{\theta}) \end{bmatrix} \tag{2.6}$$

in which $Re_{bat}(\omega, \boldsymbol{\theta})$ and $Im_{bat}(\omega, \boldsymbol{\theta})$ correspond to equations (2.1) and (2.2) respectively evaluated for the parameters in vector $\boldsymbol{\theta}$, defined as:

$$\boldsymbol{\theta} = \begin{bmatrix} L & R_s & R_{p1} & G_1 & \phi_1 & R_{p2} & G_2 & \phi_2 & A_w \end{bmatrix}^T \tag{2.7}$$

where the operator $\boldsymbol{x}^T$ corresponds to the transpose of array $\boldsymbol{x}$. The problem of finding the values of the circuit parameters

that approximate the experimental data can be established as the problem of minimising:

$$\begin{aligned}&\min_{\boldsymbol{\theta}} \sum_{i=1}^{N} \left([\boldsymbol{z_i} - \boldsymbol{Z_{bat}}(\omega_i, \boldsymbol{\theta})]^T \cdot [\boldsymbol{z_i} - \boldsymbol{Z_{bat}}(\omega_i, \boldsymbol{\theta})] \right) \\ &= \min_{\boldsymbol{\theta}} \sum_{i=1}^{N} \left((Re_{z_i} - Re_{bat}(\omega_i, \boldsymbol{\theta}))^2 + (Im_{z_i} - Im_{bat}(\omega_i, \boldsymbol{\theta}))^2 \right)\end{aligned} \tag{2.8}$$

which basically correspond to minimising the sum of the squares of the euclidean distances between the experimental data and the complex point obtained by evaluating the impedance model at the same frequency. This optimisation problem can be solved using a non-linear least squares method, such as trust region reflective. The selection of the initial parameters is crucial for the convergence of the solution.

2.1.1.1 Definition of Initial Values for the Impedance Model Parameters

The proposed procedure for the estimation of the initial impedance parameters relies on the identification of a few critical points on the impedance plot. Once identified, the critical points can be used for defining initial parameters values as follows:

- For L and R_s the initial values, L_0 and R_{s0}, are determined from the imaginary and real parts of the impedance measured at the highest frequency value $\omega_{max} = \boldsymbol{\omega}[N]$. L_0 and R_{s0} can be taken from the impedance data matrix $\mathbf{Y}$ (2.5) as follows:

$$L_0 = \frac{\mathbf{Y}\,[2, N]}{\boldsymbol{\omega}[N]} = \frac{Im_{z_N}}{\omega_{max}} \tag{2.9}$$

$$R_s 0 = \mathbf{Y}\,[1, N] = Re_{z_N}, \tag{2.10}$$

it is worth mentioning, that this relations will only apply if the imaginary part of the impedance data includes a zero crossing. Otherwise, if only negative values of $Im_{Z_{bat}}$ are available L needs to be fixed as zero and (2.10) can still be used as an initial value for R_s.

- For defining an initial value for A_w, namely A_{w0}, first the low frequencies inflection point, at frequency ω_{LF}, needs to be identified. This can be done by computing the numerical derivative dIm_{z_i}/dRe_{z_i}, then ω_{LF} can be identified as the first value for which the derivative approaches zero. Then the initial approximation can be calculated as the mean value of the slope in the plot Re_{z_i} vs $1/\sqrt{w}$ at frequencies under ω_{LF}. Numerically, from the experimental data, namely $\boldsymbol{\omega}$ and $\mathbf{Y}$, A_{w0} can be computed as:

$$A_{w0} = \frac{1}{i_{LF}} \sum_{i=1}^{i_{LF}-1} s_i, \tag{2.11}$$

where i_{LF} is the index of ω_{LF} in $\boldsymbol{\omega}$, and s_i is the numerical derivative:

$$s_i = \frac{Re_{z_{i+1}} - Re_{z_i}}{\frac{1}{\sqrt{w_{i+1}}} - \frac{1}{\sqrt{w_i}}}. \tag{2.12}$$

- The two CPE elements are initially approximated as RC parallel elements by assuming $\phi_1 = \phi_2 = 1$, which allows to approximate initial values of the respective R_p and G by making use of the imaginary part and frequency values at the highest point in the corresponding semi-circle in the impedance plot.

2.1.2 EIS Fitting Results

The procedure was tested using EIS results taken from the *Sandia Cell EIS Testing Data* repository [100]. The data corresponds to

a $LiCoO_2$ cell LGDBHE21865, with a nominal capacity of 2.5 Ah. The considered impedance measurements were obtained for the cell with a SoC of 0 % using sine signals with an amplitude of 5 mV around to open circuit condition at five different cell temperatures. In this work only the impedance values in the range between 0.1 and 10000 Hz, considering 10 points per decade, were used for the tests performed under 25, 35 and 45°C.

The fitting results for the described experimental EIS data are presented in Figure 2.2. For the three temperature values a good approximation of the experimental data was found when the initial parameters were set according to the proposed considerations. In the other hand, when the initial condition was set with all the parameters equal to zero a solution with high errors in the approximation was reached as seen in Figure 2.2. It is worth mentioning that even when considering more practical fixed initial parameters, such as the average between the maximum and minimum expected values for each parameter, the proposed method with dynamic initial values reaches solutions with lower errors. For the three temperatures, the euclidean distance between the experimental and the estimated impedance points was calculated. For all the impedance points in the three cases, the relative values of the distances with respect the experimental impedance values were under 1.6%, evidencing the goodness of the reached fittings. The main differences between the experimental and approximated data are observed at low frequencies, at which the experimental data presents a curvature that can not be fully represented using the Warburg element.

2.2 Time-Domain Implementation of Fractional-Order Battery Impedance Models

Time-domain implementations of FOMs' electrical responses have been employed in applications such as online SoC estimation using

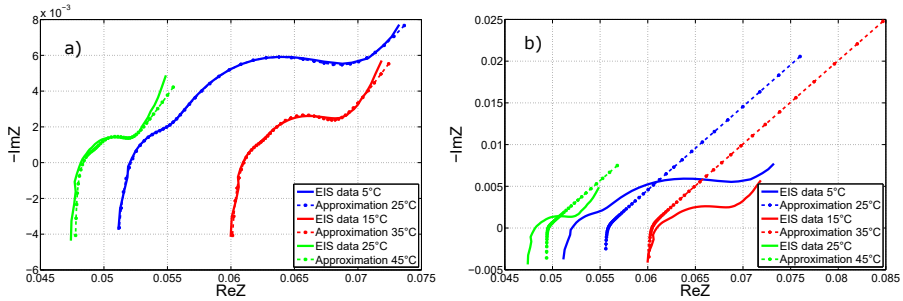

Figure 2.2: Results obtained for the proposed fitting procedure using the described experimental EIS data: a) Results obtained using the proposed initial parameters b) Results obtained using zero as initial condition for all the parameters.

FO KFs [101] and time-domain characterisation of battery diffusion dynamics [102]. Three main implementation approaches have been identified in the literature: the multiple RC (mRC) circuit [98], the high-order integer transfer function [103] and the Grünwald–Letnikov (GL) fractional derivative [104] approximations. However, the literature is rather obscure about the implementation considerations for the three approaches as well as about the motivation for the selection of one approach over the others. This section aims to fill this gap by proposing discrete equations for the implementation of the three approaches. Furthermore, a comparative study of the three approaches is also performed. The comparisons are made in terms of:

- *Accuracy:* by analysing the error of each implementation with respect to a reference analytical model for given input signals;
- *Complexity:* by writing the sets of equations required by each approach using similar structures and comparing the sizes of the arrays involved and the numbers of required additions and multiplications, in view of an embedded use of the FOMs;
- *Suitability for identification of impedance parameters* from

time-domain measurements.

The comparison was performed using a simulation environment with a set of FOMs representing the middle-frequency range impedance of Li-ion batteries, normally represented by ZARC elements as discussed on Section 1.1.3. This study identifies which of the analysed approaches offers the best compromise between accuracy and computational burden for applications such as real-time simulations. The second goal was to understand for which of the three cases the time-domain identification of the FOM leads to a correct frequency-domain response, keeping the impedance model meaningful. This analysis may serve as a guide for the selection of implementation approaches for FOMs in BMS applications.

For the sake of simplicity, the discussion that follows focuses on the computation of the voltage $v(t)$ of one of the ZARC elements in (1.5) for a given current signal $i(t)$. The presented results can easily be extended to the Warburg element using similar principles, and from there, to the whole battery's impedance.

2.3 Time-Domain Implementation of the ZARC Element Response

In the framework of battery modelling, three main approaches for approximating the time-domain response of elements with FO transfer functions have been proposed.

1. *Approximation (1).* The FO impedance is approximated with a series of parallel RC branches [105, 106, 107]. In [105], the mRC approximation was used for the implementation of two battery diffusion impedance models. A comparison in terms of the accuracy of the two models is presented. Similarly in [106], a CPE was used for approximating the diffusion dynamics of Li-ion batteries. A comparison of the identification performances of multiple implementations of the CPE based on the mRC approach is presented. The authors of [107] used the mRC approach for the approximation

of the response of a ZARC element, in the framework of time-domain-based identification of impedance models for batteries.

2. *Approximation (2).* The approximation of the FO transfer function with a high-degree integer-order system, the Oustaloup (OU) approach being the most widely adopted [62, 108, 102]. In [62] and [108], this implementation was used for FOM identification with time-domain measurements. In [102], the approximation was used for studying and identifying the diffusion dynamics of Li-ion batteries.

3. *Approximation (3).* The approximation of a derivative of FO with a specific definition that allows one to implement difference equations, mainly based on the GL definition of the FO derivative [99, 101, 96]. The study presented in [99] analysed the performance of a FOM, implemented using the GL definition of the FO derivative, for the approximation of the battery voltage, and compared the results with a typical single RC model. Additionally, a method for the time-domain identification of the FOM was provided to the readers. In [101], the implementation was used in conjunction with a FO KF for online SoC estimation. Similarly, in [96], a GL-based implementation was used with an EKF scheme for online estimation of SoC and SoH.

Flowcharts for the three implementation approaches are given in Figure 2.3. In the three approaches, the time response of the FOM is approximated by a set of discrete equations, corresponding to discrete state-space representations for the mRC and OU approaches and to a difference equation for the GL approach. These discrete implementations were evaluated in a simulation environment in terms of accuracy and complexity, as presented in the following sections. The main differences between the approaches lie in the parametrisation processes. For the GL approach, the coefficients in the difference equation are computed directly from the impedance parameters using predefined mathematical relationships, which are

introduced in Section 2.3.3. As illustrated in Figure 2.3, the other two approaches require an initial approximation of the FO transfer function with an integer-order system, for which a discrete state-space representation can be obtained. The main difference between the mRC and OU approaches is the structure of the integer-order transfer function and the method used for the approximation of the FO transfer function, which are introduced in Sections 2.3.1 and 2.3.2, respectively.

Initially, this work focuses on defining difference equations for the computation of the ZARC voltage $v(t)$ for each one of the mentioned approaches. The resulting expressions have the form given by:

$$v[k] = Cx[k] + Di[k]. \tag{2.13}$$

Equation (2.13) allows one to compute the ZARC element voltage in the discrete instant k as a function of the input value i and the vector x. The vector x may be the states' vector or a set of previous values of v, depending on the implementation approach. The values of vector C and scalar D are functions of the parameters of each approximation, as is discussed in the following subsections.

2.3.1 Approximation (1): Multiple RC

In the literature, series connections of multiple parallel RC circuits have been considered for the approximation of the ZARC element impedance [98]. The values of the components for this kind of approximations are normally fitted from time measurements directly, by minimising the differences between experimental data and the model voltage output. However, for the case in which the initial point for the model identification is an impedance model, the process requires fitting the impedance spectra. The idea is to approximate the transfer function of the ZARC element with a set of RC parallel elements:

$$Z_{ZARC}(s) = \frac{R_{p1}}{1 + R_{p1}G_1 s^{\phi_1}} \approx \sum_{h=1}^{n_{RC}} \frac{R_h}{1 + R_h C_h s} = Z_{RC}(s). \tag{2.14}$$

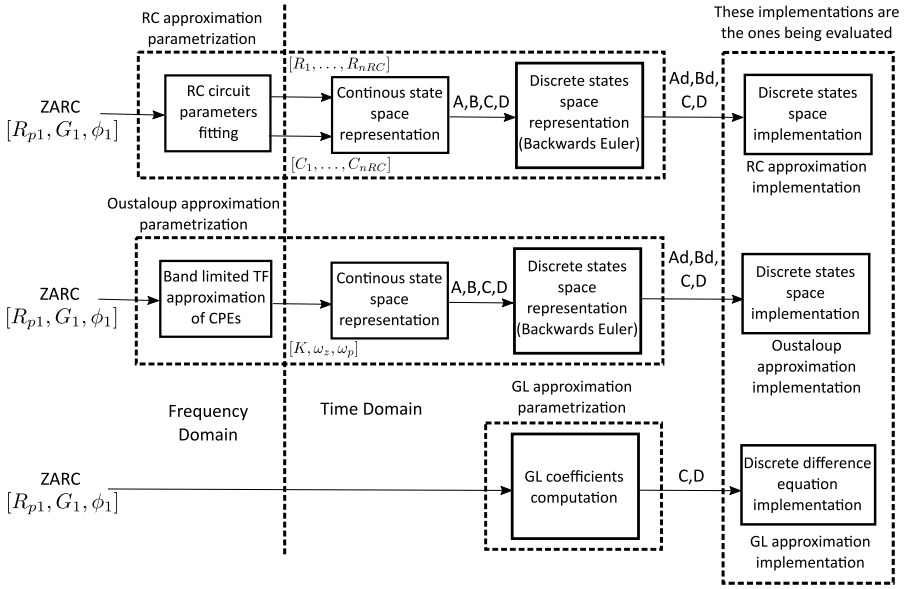

Figure 2.3: A summary of the considered FOM implementation approaches.

In (2.14), a transfer function representation is used for the impedance, using s as the Laplace complex variable. The approximation of the ZARC impedance $Z_{RC}(s)$ employs a set of n_{RC} RC branches. The parameters R_h and C_h represent the resistance and capacitance of the h-th RC parallel branch in the approximation of the ZARC impedance presented in (2.14), accounting for $2n_{RC}$ parameters to fit.

The values for the resistance and capacitance in (2.14) can be computed by minimising the difference between the ZARC impedance, given in (1.4), and the mRC approximation.

Once the values for R_h and C_h have been fitted, the continuous time response of the mRC circuit can be written in state-space representation:

$$\dot{x}_{RC}(t) = A_{RC}x_{RC}(t) + B_{RC}i(t) \tag{2.15}$$

$$v_{RC}(t) = C_{RC}x_{RC}(t) + D_{RC}i(t), \tag{2.16}$$

where the states' vector x_{RC} contains the RC elements voltages, $\dot{x}_{RC}$

represents the states' derivatives and v_{RC} is the approximation of the ZARC voltage using the mRC approach. Additionally, the matrices A_{RC}, B_{RC}, C_{RC} and D_{RC} are $n_{RC} \times n_{RC}$, $n_{RC} \times 1$, $1 \times n_{RC}$ and 1×1 matrices, respectively, given by:

$$A_{RC} = \text{diag}\left(-\frac{1}{R_1 C_1}, -\frac{1}{R_2 C_2}, \cdots, -\frac{1}{R_{n_{RC}} C_{n_{RC}}}\right) \tag{2.17}$$

$$B_{RC} = \begin{bmatrix} \frac{1}{C_1} & \frac{1}{C_2} & \cdots & \frac{1}{C_{n_{RC}}} \end{bmatrix}^\top \tag{2.18}$$

$$C_{RC} = \begin{bmatrix} 1 & 1 & \cdots & 1 \end{bmatrix} \tag{2.19}$$

$$D_{RC} = 0. \tag{2.20}$$

For the discretisation of this set of equations, the derivatives are approximated using the backward Euler approximation for stability reasons [109]. The obtained set of difference equations can be rewritten and used for estimating the value of the ZARC element voltage in a discrete instant k, $v_{RC}[k]$, as a function of the current $i[k]$ and the RC elements voltages $x_{RC}[k]$:

$$\begin{aligned} x_{RC}[k] = {} & (I_{n_{RC}} - T A_{RC})^{-1} x_{RC}[k-1] \\ & + T (I_{n_{RC}} - T A_{RC})^{-1} B_{RC} i[k] \end{aligned} \tag{2.21}$$

$$v_{RC}[k] = C_{RC} x_{RC}[k] + D_{RC} i[k], \tag{2.22}$$

in which $I_{n_{RC}}$ is the $n_{RC} \times n_{RC}$ identity matrix, and T is the sampling period. Equations (2.21) and (2.22) can be used for implementing the response of the RC approximation given a current signal and a set of initial values for the RC branch voltages.

2.3.2 Approximation (2): Oustaloup

This approach relies on approximating the transfer function of the CPE in the ZARC element using a transfer function with integer order n_{OU} (the same number of zeros and poles) in a given frequency range. One of the most popular methods for the approximation of the CPE transfer function with a rational transfer function of odd order n_{OU} was presented by Oustaloup et al.

[103]. The approximation is valid in the frequency range $\omega \in [\omega_l, \omega_h]$, where ω_l and ω_h are the lower and higher frequency limits, respectively. Following this method, the transfer function of the CPE can be rewritten as:

$$\begin{aligned} Z_{CPE}(s) &= \frac{1}{G_1 s^{\phi_1}} = K_{CPE}\left(\frac{s}{\omega_c}\right)^{-\phi_1} \\ &\approx K_{CPE}\left(\frac{\omega_l}{\omega_c}\right)^{-\phi_1} \prod_{h=-N}^{N} \frac{1+\frac{s}{\omega_{z(CPE)h}}}{1+\frac{s}{\omega_{p(CPE)h}}} \\ &= Z_{OU(CPE)}(s), \end{aligned} \tag{2.23}$$

where $Z_{OU(CPE)}(s)$ is the integer-order approximation of the CPE impedance using the OU approach; $\omega_c = \sqrt{\omega_l \omega_h}$ is the central frequency between the bounds of the range of interest; and K_{CPE} and N are given by $K_{CPE} = \frac{1}{G_1 \omega_c^{\phi_1}}$ and $N = \frac{n_{OU}-1}{2}$. In order to estimate the n_{OU} zeros $\omega_{z(CPE)h}$ and n_{OU} poles $\omega_{p(CPE)h}$ in (2.23), Oustaloup et al. proposed [103]:

$$\begin{aligned} \omega_{z(CPE)h} &= \omega_l \left(\frac{\omega_h}{\omega_l}\right)^{\frac{h+\frac{n_{OU}+\phi_1}{2}}{n_{OU}}}, \\ \omega_{p(CPE)h} &= \omega_l \left(\frac{\omega_h}{\omega_l}\right)^{\frac{h+\frac{n_{OU}-\phi_1}{2}}{n_{OU}}}. \end{aligned} \tag{2.24}$$

The transfer function can be used to approximate the frequency response of the CPE. Then, the approximation $Z_{OU}(s)$ of the whole ZARC impedance using the OU approach is:

$$Z_{ZARC}(s) = \frac{R_{p1}}{1 + R_{p1} G_1 s^{\phi_1}} \approx \frac{R_{p1}}{1 + \frac{R_{p1}}{Z_{OU(CPE)}(s)}} = Z_{OU}(s). \tag{2.25}$$

In order to obtain a time representation of the response of this approximation, the transfer function $Z_{OU}(s)$ needs to be rewritten in zero-pole-gain form, as expressed in:

$$Z_{OU}(s) = K_{ZARC} \prod_{h=1}^{n_{OU}} \frac{(s-\omega_{zh})}{(s-\omega_{ph})}, \tag{2.26}$$

where K_{ZARC}, ω_{zh} and ω_{ph} represent the gain, zeros and poles of the $Z_{OU}(s)$ transfer function, respectively. A time-domain state-space representation for the OU approximation with the structure presented in (2.26) was introduced in [109]:

$$\dot{x}_{OU}(t) = A_{OU}x_{OU}(t) + B_{OU}i(t) \tag{2.27}$$

$$v_{OU}(t) = C_{OU}x_{OU}(t) + D_{OU}i(t), \tag{2.28}$$

where x_{OU} and $\dot{x}_{OU}$ represent the system states and their derivatives, and v_{OU} is the approximation of the ZARC element voltage. The matrices A_{OU} $n_{OU} \times n_{OU}$, B_{OU} $n_{OU} \times 1$, C_{OU} $1 \times n_{OU}$ and D_{OU} 1×1, are given by:

$$A_{OU} = \begin{bmatrix} \omega_{p1} & 0 & 0 & \cdots & 0 \\ (\omega_{p2} - \omega_{z2}) & \omega_{p2} & 0 & \cdots & 0 \\ (\omega_{p3} - \omega_{z3}) & (\omega_{p3} - \omega_{z3}) & \omega_{p3} & \cdots & 0 \\ \vdots & \vdots & \vdots & \ddots & \vdots \\ (\omega_{pn_{OU}} - \omega_{zn_{OU}}) & (\omega_{pn_{OU}} - \omega_{zn_{OU}}) & \cdots & (\omega_{pn_{OU}} - \omega_{zn_{OU}}) & \omega_{pn_{OU}} \end{bmatrix} \tag{2.29}$$

$$B_{OU} = K_{ZARC}\begin{bmatrix} (\omega_{p1} - \omega_{z1}) & (\omega_{p2} - \omega_{z2}) & \cdots & (\omega_{pn_{OU}} - \omega_{zn_{OU}}) \end{bmatrix}^{\top} \tag{2.30}$$

$$C_{OU} = \begin{bmatrix} 1 & 1 & \cdots & 1 \end{bmatrix} \tag{2.31}$$

$$D_{OU} = K_{ZARC}. \tag{2.32}$$

Again, the backward Euler approximation was used to discretise the obtained state-space system. This discrete representation is obtained by replacing A_{RC}, B_{RC}, C_{RC} and D_{RC} with A_{OU}, B_{OU}, C_{OU} and D_{OU} in (2.21) and (2.22).

2.3.3 Approximation (3): Grünwald–Letnikov

The ZARC element response can be approximated by adopting a FO derivative definition in the time domain. The FO differential equations representing the ZARC voltage can be obtained from the transfer function (1.4) by replacing $Z_{ZARC}(s) = V(s)/I(s)$ and rewriting the equation as:

$$s^{\phi_1}V(s) = \frac{I(s)}{G_1} - \frac{V(s)}{R_{p1}G_1}, \tag{2.33}$$

where $V(s)$ and $I(s)$ represent the Laplace transform of the ZARC voltage and current, respectively. Then, by applying inverse Laplace transform, the FO differential equation is rewritten as:

$$\mathscr{D}^{\phi_1} v(t) = \frac{i(t)}{G_1} - \frac{v(t)}{R_{p1} G_1}. \tag{2.34}$$

$\mathscr{D}^{\phi_1}$ represents the derivative of ϕ_1 order. Among the multiple definitions of the FO derivative, the GL one is of particular interest, as it allows one to directly obtain difference equations, which can be used for the approximation of the FO system's time response [104]. The considered definition is:

$$\mathscr{D}^{\alpha} f(t) = \lim_{T \to \infty} \frac{1}{T^{\alpha}} \sum_{h=0}^{\left\lfloor \frac{t}{T} \right\rfloor} (-1)^h \binom{\alpha}{h} f(t - hT), \tag{2.35}$$

where the derivative of FO α of the causal function $f(t)$ is computed between 0 and t. In (2.35), T is the sampling period, $\left\lfloor \frac{t}{T} \right\rfloor$ represents the integer part of t/T and $\binom{\alpha}{h}$ represents the Newtonian binomial coefficients generalised to real numbers, computed as:

$$\begin{aligned} \binom{\alpha}{h} &= \frac{\alpha(\alpha-1)(\alpha-2)\cdots(\alpha-h+1)}{h!} \\ &= \frac{\Gamma(\alpha+1)}{\Gamma(h+1)\Gamma(\alpha-h+1)}, \end{aligned} \tag{2.36}$$

where $\Gamma(\cdot)$ stands for the gamma function, which works as a generalisation of the factorial operator for real numbers.

It is worth noting that, according to the GL definition in (2.35), the derivative of order α of the function at time t depends on all the values of that function in $[0, t]$, which is due to the non-local property of fractional derivatives [110].

By fixing the value of T to an appropriately low value for the application, and adopting the discrete variable k instead of the continuous time t, it is possible to obtain the first order discrete approximation of the FO derivative:

$$\mathscr{D}^{\alpha} f[k] = \frac{1}{T^{\alpha}} \sum_{h=0}^{k} (-1)^h \binom{\alpha}{h} f[k - h]. \tag{2.37}$$

This approximation may be used to obtain a difference equation for the numerical evaluation of function $f[k]$. The discrete version also requires all the data points of $f[k]$ since $k = 0$ for the computation of the derivative approximation, which may imply large memory requirements for simulations using this approach. This drawback may be addressed by applying the short-memory principle reported in reference [104], taking into account the behaviour of the signal in only the recent past, i.e., in the interval $[k-L, k-1]$, where L is the memory length. Applying this principle, (2.37) can be rewritten:

$$\mathscr{D}^{\alpha} f[k] = \frac{1}{T^{\alpha}} \sum_{h=0}^{L} (-1)^h \binom{\alpha}{h} f[k-h]. \tag{2.38}$$

This short-memory approximation allows one to implement numerical difference equations in cases in which the required memory is a critical constraint. Obviously, this introduces some inaccuracy, mostly manifested in the form of static error [111].

By replacing (2.38) in (2.34), the following difference equation is obtained:

$$\begin{aligned} v_{GL}[k] =& T^{\phi_1} \frac{R_{p1}}{R_{p1}G_1 + T^{\phi_1}} i[k] \\ & - \frac{R_{p1}G_1}{R_{p1}G_1 + T^{\phi_1}} \sum_{h=1}^{L} (-1)^h \binom{\phi_1}{h} v_{GL}[k-h], \end{aligned} \tag{2.39}$$

which allows one to compute the approximation of the ZARC element voltage using the GL approach v_{GL}. For the sake of comparison with the other implementation approaches, (2.39) can be written in matrix form:

$$v_{GL}[k] = C_{GL} x_{GL}[k] + D_{GL} i[k], \tag{2.40}$$

where $x_{GL}[k]$ is a $L \times 1$ vector with the L previous values of the ZARC voltage:

$$x_{GL} = \begin{bmatrix} v_{GL}[k-1] & v_{GL}[k-2] & \cdots & v_{GL}[k-L] \end{bmatrix}^{\top}. \tag{2.41}$$

The matrices C_{GL} and D_{GL}, having size $L \times 1$ and 1×1, respectively, are given by:

$$C_{GL} = -\frac{R_{p1}G_1}{R_{p1}G_1 + T^{\phi_1}}\left[-\binom{\phi_1}{1} \quad \binom{\phi_1}{2} \quad \cdots \quad (-1)^h\binom{\phi_1}{h} \quad \cdots \quad (-1)^L\binom{\phi_1}{L}\right] \tag{2.42}$$

$$D_{GL} = T^{\phi_1}\frac{R_{p1}}{R_{p1}G_1 + T^{\phi_1}}. \tag{2.43}$$

It is worth noting that for the matrix C_{GL}, the coefficients $(-1)^h\binom{\phi_1}{h}$ for the previous samples can be precomputed for the implementation of the ZARC voltage equation.

2.3.4 Accuracy Comparison

Ideally, the data required for the validation of approximations of the responses of FO battery impedance models must consider EIS and pulsed current tests, both performed under similar SoC, SoH and temperature conditions. Due to the lack of availability of such data in the known datasets, and in order to perform accuracy comparisons between the analysed approximations, a reference model based on the analytical solution of FO differential equations was utilised for the generation of the reference data.

2.3.4.1 Reference Data Generation from the Analytical Solution of Fractional Differential Equations

Assuming that the current signal can be written as a set of steps:

$$i(t) = \sum_{h=1}^{N_u} U_h u(t - t_{uh}), \tag{2.44}$$

where $u(t)$ corresponds to the unit step function. Each one of the N_u current steps in $i(t)$ is characterised by an amplitude U_h and application time t_{uh}.

The ZARC element voltage can be expressed as [104]:

$$v(t) = \sum_{h=1}^{N_u} \frac{U_h}{G_1}(t - t_{uh})^{\phi_1} E_{\phi_1,\phi_1+1}\left(-\frac{1}{R_{p1}G_1}(t - t_{uh})^{\phi_1}\right) u(t - t_{uh}), \tag{2.45}$$

where the function $E_{\alpha,\beta}$ is the two-parameter Mittag–Leffler function, defined by a series expansion:

$$E_{\alpha,\beta}(t) = \sum_{h=0}^{\infty} \frac{t^h}{\Gamma(\alpha h + \beta)}, \tag{2.46}$$

and it can be seen as a generalisation of the exponential function e^t, which can be considered as a particular case of the $E_{\alpha,\beta}(t)$ function with $\alpha = \beta = 1$ [104].

Equation (2.45) was implemented in Matlab® for the generation of the reference data. For the Mittag–Leffler function, the implementation introduced in [112] was employed. It is worth mentioning that such an analytical voltage representation is not suitable for online implementation, due to the limitations imposed by the assumed input signal and to the iterative nature of the Mittag–Leffler function computation, which makes the evaluation of a single data point highly demanding from a computational point of view.

2.3.4.2 Analysis of the Voltage Approximation Signals

The evaluation of the accuracy of the considered approximations requires one to perform an analysis of the differences between the responses of the reference model and the approximation of interest, for given ZARC element parameters and while using the same input current signal, as illustrated in Figure 2.4.

The test proposed in Figure 2.4 requires one to define an input current signal, a set of ZARC elements parameters and the order or memory length of the approximations. Tests such as this one were performed for six sets of ZARC element parameters, for currents generated with different sampling and dynamic characteristics and with variations of n_{RC}, n_{OU} and L. In order to generate the input currents and select the ZARC elements to be employed, first, the

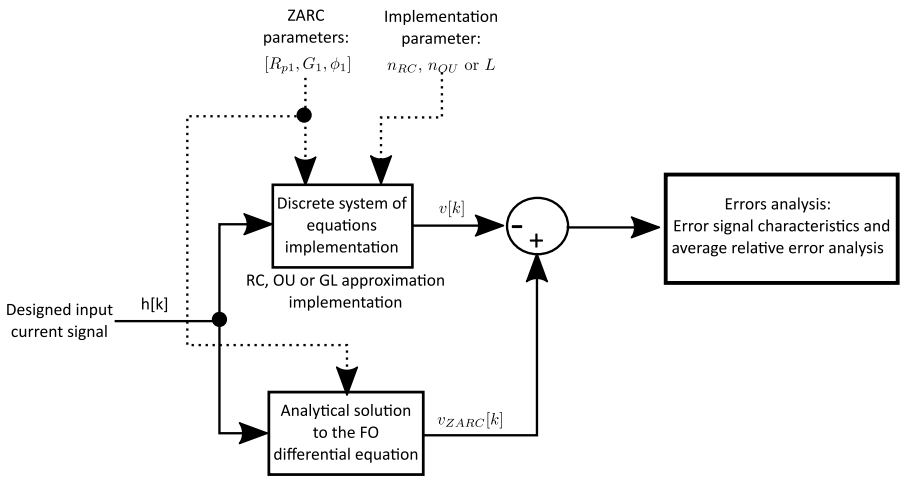

Figure 2.4: A schematic diagram representing the accuracy tests performed.

analysis is focused on the typical middle-frequency range of the dynamic response of Li-ion batteries, namely, the range between 0.01 and 200 Hz. This dynamic range is normally associated with the response of the double layer capacitance and the charge transfer resistance [19].

The considered input signals contained two stages: one aimed at evaluating the transient responses of the different approximations, and the second stage was for testing the steady state error. An input signal sample is presented in Figure 2.5. In this signal, the first stage has a total duration of 200 s, for which the amplitude and duration of each current pulse were selected randomly in the ranges $[-1, 1]$ A and $[0.5, 10]$ s, respectively. The second stage contains one single 0.5 A step with a duration of 500 s, with fixed 150 s rests before and after the step.

The six sets of ZARC parameters used for the analysis are presented in Table 2.2. The ZARC parameters were selected for obtaining characteristic frequencies $\omega_0 = (1/(R_{p1}G_1))^{1/\phi_1}$ covering the frequency range of interest, with $\omega_0 = 2\pi f_0$, while keeping the parameters' values inside typical ranges—namely, $R_{p1} \in [0.1, 100]$ mΩ, $G_1 \in [1, 1000]$ F s$^{\phi_1 - 1}$ and $\phi_1 \in [0.5, 0.9]$ [113, 114].

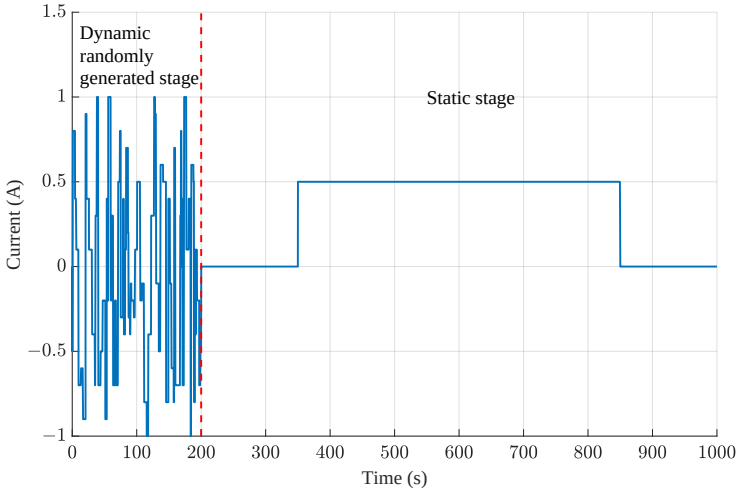

Figure 2.5: An example of the current profiles used during the accuracy tests.

The evaluation of accuracy was performed for:

- Nine mRC-based approximations, employing n_{RC} values corresponding to the odd numbers between 3 and 19;
- Nine OU-based implementations, with odd orders n_{OU} between 3 and 19;
- Fourteen GL-based approximations, with L values between 5 and 10,000 samples (which correspond to time windows between 0.05 and 100 s).

Figures 2.6 and 2.7 present some examples of the voltage computed by mRC, OU and GL approximations for ZARC 4 employing $T = 0.01$ s. The plots in Figure 2.6a present the reference voltage and the voltages obtained for three mRC-based approximations during the first 20 s of the random stage of the accuracy test. In general, all the implementations were able to approximate the dynamics of the reference signal, with only appreciable differences for the approximation being of the lowest order. The error signals,

Table 2.2: Values of the parameters for the ZARC elements considered during the accuracy tests.

ZARC id	f_0 **(Hz)**	R_{p1} **(mΩ)**	G_1 **(F s$^{\phi_1-1}$)**	ϕ_1
1	0.034	59.2	55	0.77
2	0.090	8.4	193	0.86
3	0.487	60.4	8	0.65
4	0.787	5.8	55	0.72
5	2.444	0.3	722	0.56
6	8.215	0.8	122	0.59

presented in Figure 2.8a for this set of implementations, show spikes always under a few hundreds of microvolts during all the current steps, which reduce in magnitude as the order increases. Similar results can be observed for the OU-based implementations, as shown in Figure 2.6b and the first 200 s of the error signal in Figure 2.8b. The low-order OU approximations resulted in higher error magnitudes than the mRC ones. In the case of the GL approximations, as seen in Figure 2.6c, the lower L values caused higher offset errors. This is further illustrated by the error signal in Figure 2.8c during the first 200 s on which the spikes, at least for the lower memory lengths, seem to be wider than those in the mRC and OU approximations. An increase in L led to decreases in the magnitudes of the error signal, showing that adding terms to the sum in (2.39) leads to a better approximation of the analytical response, as expected.

As it is shown in the static state results presented in Figure 2.7a for three mRC-based implementations, increasing the order of the approximation reduced the errors during this stage. A higher value of n_{RC} allowed a better approximation of the distribution of time constants represented by the FO element, leading to an extension of the validity of the approximation over a wider frequency range. Similar considerations apply for the OU approximations, presented in Figure 2.7b, except for the worse performance at low orders, under nine, with respect to the mRC case. The offset error for the

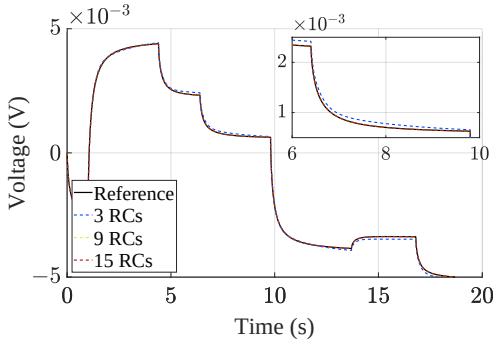

(**a**)

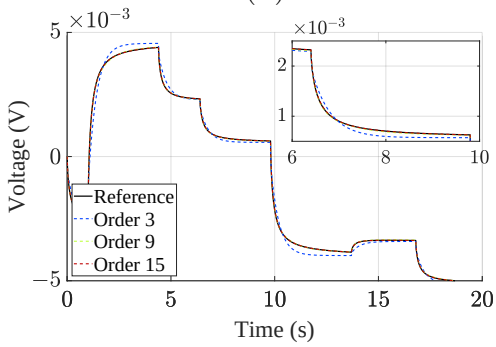

(**b**)

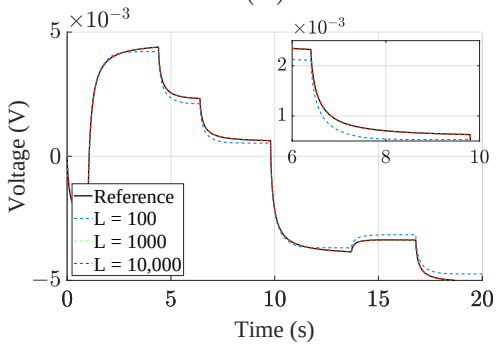

(**c**)

Figure 2.6: Examples of ZARC 4 voltages during the dynamic stage of the accuracy test. (**a**) mRC; (**b**) OU; (**c**) GL.

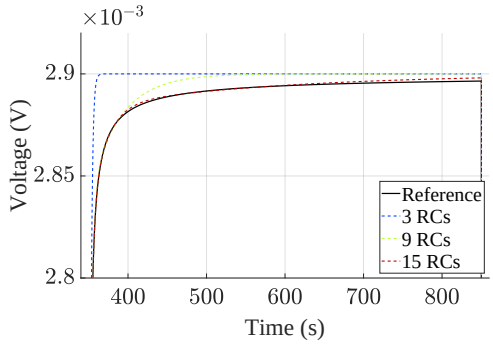

(**a**)

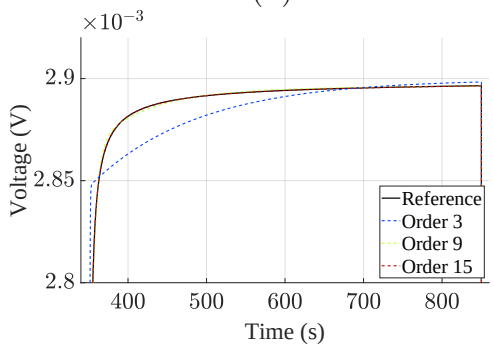

(**b**)

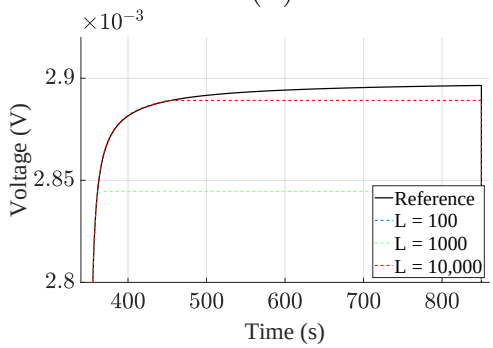

(**c**)

Figure 2.7: Examples of ZARC 4 voltages during the static stage of the accuracy test. (**a**) mRC; (**b**) OU; (**c**) GL.

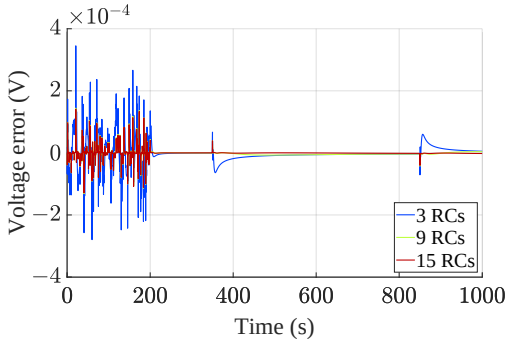

(a)

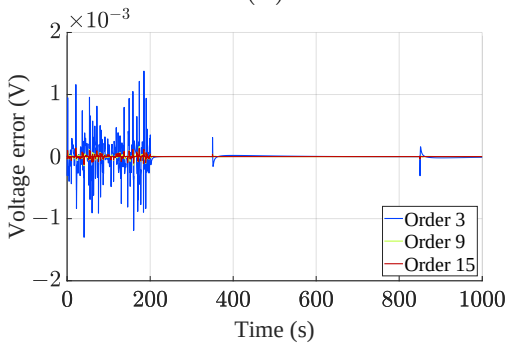

(b)

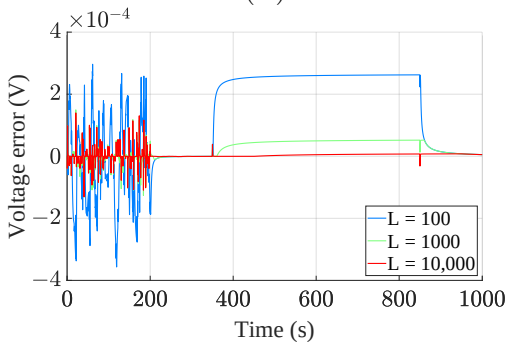

(c)

Figure 2.8: Examples of ZARC 4 voltage errors during the accuracy test. (**a**) mRC; (**b**) OU; (**c**) GL.

GL approximations is more evident during the static stage of the test, as shown in Figures 2.7c and 2.8c. The static error obtained for GL implementations with L under a few thousand for ZARC 4 is considerably higher than the errors obtained for the other approximations. This highlights the main drawback of the GL approximations using the short memory principle: by reducing the number of previous samples that are used for the computation, some level of inaccuracy appears, particularly in static state. For the sake of completeness, it is worth mentioning that Podlubny [104] proposed a relationship for estimating a suitable memory length for the approximation of the FO derivative presented in (2.37), given an expected error level.

2.3.4.3 Effects of the Approximation Order and Memory Length on The Accuracy

In order to analyse the effects of the parameters in each implementation approach, namely, n_{RC}, n_{OU} and L, on the approximation accuracy, the mean relative errors during the dynamic and the static stages were used as indicators. For ZARCs 1, 3 and 6, the mean relative errors during the dynamic and the static stages are presented in Figures 2.9a and 2.10a, respectively. The very similar results for the other ZARC elements are not reported for the sake of brevity.

The error during the static stage of the tests for the RC approximations remained under 1%, even for the approximations with fewer RC branches. This result was expected, as in the fitting procedure adopted in this work for the mRC approach, the sum of the resistances in the mRC approximation was set to match the value of R_{p1}, leading to similar voltage drops in the response after the initial transitory. On the other hand, even if the values of the relative error during the dynamic stage tended to decrease with the number of employed RC elements, considerable improvements were only obtained up to $n_{RC} = 9$. After that point, further improvements could be achieved by decreasing the value of T. The observed behaviour at the highest orders may be associated

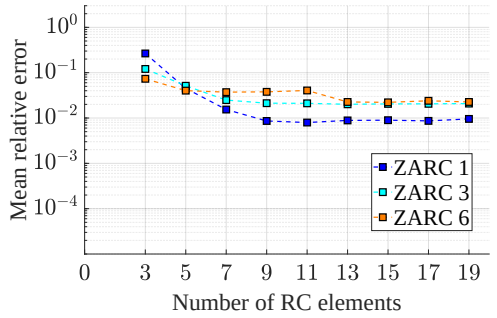

(**a**)

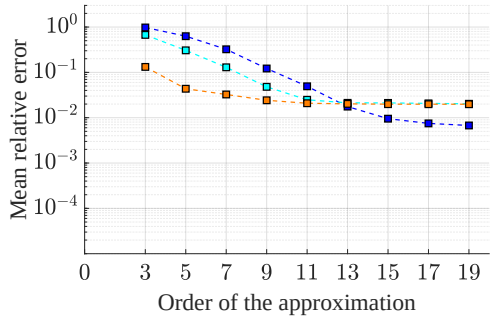

(**b**)

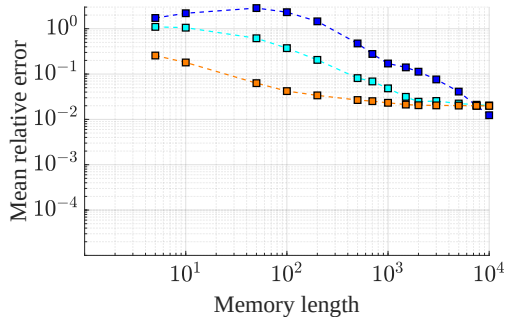

(**c**)

Figure 2.9: Average relative errors during the dynamic stage of the test. (**a**) mRC; (**b**) OU; (**c**) GL.

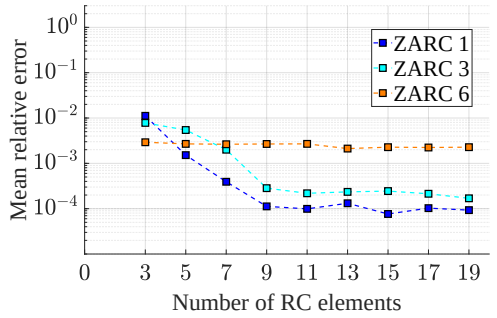

(**a**)

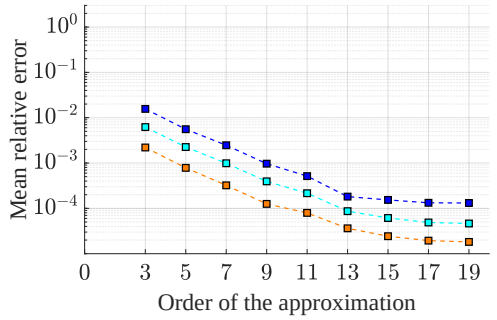

(**b**)

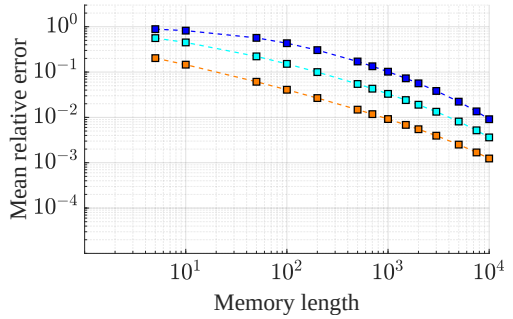

(**c**)

Figure 2.10: Average relative errors during the static stage of the test. (**a**) mRC; (**b**) OU; (**c**) GL.

with the variability introduced by the fitting procedure required for the computation of the parameters of the mRC case from the ZARC parameters. Nevertheless, for cases over $n_{RC} = 5$, the mean relative errors were always under 5%.

In the case of the OU-based approximations, the mean relative errors during the dynamic and the static stages are presented in Figures 2.9b and 2.10b, respectively. In general, for the OU approximations during the dynamic stage, orders n_{OU} higher than nine are required for reaching average relative errors under 5%. It is worth noting that, compared with the mRC approach, similar average relative errors were achievable in general, but with approximations of higher order. Again, the average relative errors for the static tests were almost always below 1%. For both stages of the accuracy tests, a monotonic reduction in the errors could be observed with increases in the approximation order, highlighting the advantage of computing the integer order approximation of the FO transfer function with a set of predefined equations instead of performing a fitting. This behaviour can be useful when trying to select the approximation order by analysing the accuracy–complexity trade off.

Then, for a set of GL-based approximations, with L values between 5 and 10,000 samples (which correspond to time windows between 0.05 s and 100 s), a similar accuracy analysis was performed. Figures 2.9c and 2.10c show the results obtained for the dynamic and static average relative errors obtained for this set of approximations. Regarding the results in the dynamic stage, only the higher memory lengths, over 500 samples, allowed to reach values in the same order of magnitude as the ones obtained for the other approaches. In the case of the static stage, the average relative error is always about one order for magnitude higher, and it is evident that higher memory lengths or sampling times need to be considered for reducing the static error to a similar range. The errors were higher for the ZARC elements with slower dynamics, showing that slower systems require longer memory lengths to reach an acceptable accuracy level.

2.3.5 Computational Burden Comparison

A battery ECM can be used as a part of the BMS state estimation structure or for battery simulation purposes during validation of energy management algorithms, particularly in real-time simulation scenarios. In both cases, considering that normally middle to low-end processing devices are often favoured due to budgetary restrictions, care needs to be taken in regard to the computational requirements of the battery model implementation. Here, those requirements are analysed in a general sense, by addressing the sizes of the matrices and the number of operations for each FOM implementation approach as indicators of required memory and computational complexity, respectively, in a possible deployment.

For the three approaches, the time implementation relies on a set of matrix additions and multiplications. For mRC and OU-based approaches, the implementations consist of sets of equations in the form of (2.47) and (2.13) for the state and output equations, respectively. The discrete state equation established for the mRC approach can be generalised as:

$$x[k] = A_d x[k-1] + B_d i[k], \tag{2.47}$$

where A_d and B_d, namely, the discrete state and input matrices, are given by:

$$A_d = \left(I_{n_{RC}} - TA_{RC}\right)^{-1} \tag{2.48}$$

$$B_d = T\left(I_{n_{RC}} - TA_{RC}\right)^{-1} B_{RC}. \tag{2.49}$$

Conversely, the GL-based implementation relies only on a difference equation with the structure of (2.13), but in which $x[k]$ does not represent the system states vector but a vector with L previous values of the ZARC voltage.

Table 2.3 presents the sizes of the matrices and vectors used in the three approaches. Even if the mRC and OU approaches seem to be equivalent in terms of memory requirements, the simpler structure of the mRC can be exploited for the reduction of its memory requirements. Additionally, even if the number of arrays

required for a GL implementation is lower and its size dependency given L seems simpler than those for the matrices in the other approaches, it is worth keeping in mind that in general for a given accuracy level L will take values in the range of hundreds or thousands, while n_{RC} or n_{OU} will be under 20.

Table 2.3: Sizes of the matrices in the state and output equations in the analysed implementations.

Element	**mRC**	**OU**	**GL**
A_d	$n_{RC} \times n_{RC}$ (Diagonal)	$n_{OU} \times n_{OU}$ (Lower triangular)	–
B_d	$n_{RC} \times 1$	$n_{OU} \times 1$	–
C	$1 \times n_{RC}$ (All-ones)	$1 \times n_{OU}$ (All-ones)	$L \times 1$
D	1×1 (zero)	1×1	1×1

Table 2.4 summarises the numbers of additions and multiplications required by each implementation approach. The specific structures of the matrices can be also exploited in the mRC and OU-based implementations, to refine the results presented in Table 2.4 by skipping the multiplications by zero and expressing the multiplication of column vectors by row vectors full of ones as an addition. The new operations count with this considerations is presented in Table 2.5.

Table 2.4: Numbers of additions and multiplications required for the analysed implementations.

Approach	**Additions**	**Multiplications**	**Total**
RC	$n_{RC}^2 + n_{RC}$	$n_{RC}^2 + 2n_{RC} + 1$	$2n_{RC}^2 + 3n_{RC} + 1$
OU	$n_{OU}^2 + n_{OU}$	$n_{OU}^2 + 2n_{OU} + 1$	$2n_{OU}^2 + 3n_{OU} + 1$
GL	L	$L + 1$	$2L + 1$

Similarly to what was concluded for the array dimensions discussion, the expressions in Table 2.5 show that for the same order,

Table 2.5: Numbers of additions and multiplications with simplifications.

Approach	**Additions**	**Multiplications**	**Total**
RC	$2n_{RC} - 1$	$2n_{RC}$	$4n_{RC} - 1$
OU	$\frac{n_{OU}^2+3n_{OU}}{2}$	$\frac{n_{OU}^2+3n_{OU}+2}{2}$	$n_{OU}^2 + 3n_{OU} + 1$
GL	L	$L + 1$	$2L + 1$

a mRC implementation will require fewer operations than an OU one. It is worth mentioning that for the GL approach, even if there is not dependence on the square of L in the expressions for the number of operations required, the value of L needs to be considerably higher than the order for the other approaches to reach a given accuracy level.

The number of multiplications required for the evaluation of each type of implementation was used for assessing the computational burden in each case. Figure 2.11 plots the accuracy against the computational burden in terms of the number of multiplications for ZARC 4. The errors in static and dynamic stages are shown in Figure 2.11a,b, respectively.

The curves for $T = 0.01$ s in Figure 2.11a show clearly how for a fixed mean relative error level in the dynamic stage of the accuracy tests, the number of required multiplications is always lower for the mRC approach, followed by the OU one. It is worth mentioning that the three approaches converge to values in the same order of magnitude for the mean relative error when increasing the complexity of the implementation; this may be an effect of the local truncation error due to the discretisation process. The asymptotic values of the analysed errors are comparable for a fixed sampling time. This can be ascribed to the fact that both the backward Euler and the GL derivative approximations are first-order approximations, leading to an $O(T)$ local truncation error, using big O notation [104]. To show the dependency on the sampling time of the identified error asymptotic values, the accuracy test was repeated using the current signal in Figure 2.5, but downsampled

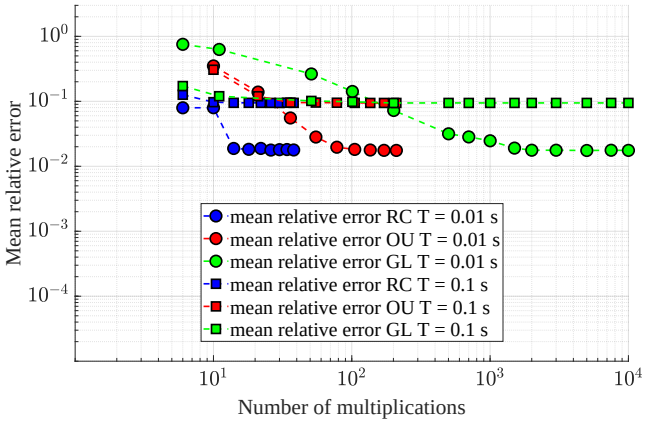

(**a**)

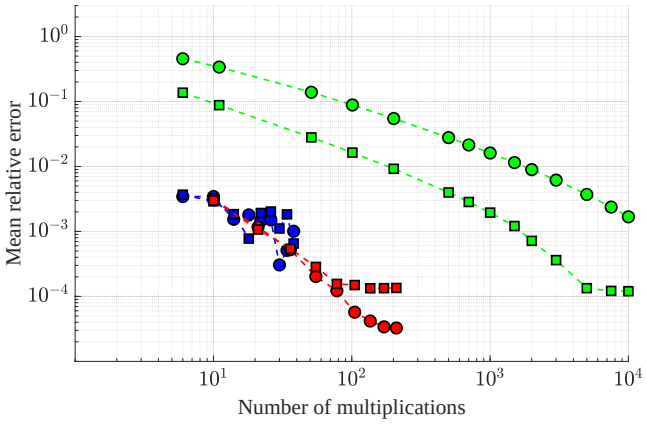

(**b**)

Figure 2.11: Average relative errors vs. numbers of multiplications for mRC, OU and GL. (**a**) Dynamic stage; (**b**) static stage.

using $T = 0.1$ s. Those results are also summarised in Figure 2.11a, showing how the limit in the mean relative error is reached at a higher value, confirming the relationship between the sampling time and the maximum achievable accuracy.

The results presented in Figure 2.11b show that an increase in complexity has a more pronounced effect on the accuracy under static conditions, which tracks back to the requirement of higher orders or memory lengths for covering a wider time-constant range in the response approximation. In this case the previously observed oscillatory behaviour for higher orders in the mRC implementations is more evident for the two considered values of T. The effect of the local truncation error due to the discretisation process is also observed in this case, even if for lower values of the mean relative error.

From the results of the accuracy against complexity analysis, it can be clearly observed that the best accuracy–complexity compromise is offered by the mRC approach, allowing one to reach low error levels with a small computational burden. It is worth mentioning that this is the case provided good fitting of the ZARC element in the frequency domain can be performed. This is true for applications in which the model is used for battery simulation, but it is not the case when identification of impedance models from time measurements is required. In such instances, a good relationship between the parameters fitted from time-domain experiments with the frequency response is required. Thus, it is worth checking the suitability of the implementations for the time-domain identification of impedance parameters.

2.3.6 Suitability for Time-Domain Identification

One of the main reasons for adopting battery FOMs is the capability of accurately approximate the voltage response while requiring a low number of parameters, which is of interest for tasks such as state estimation and battery characterisation. For this reason, in order to illustrate the applicability of the considered FOM implementation

approaches in the framework of battery model identification using time-domain measurements, a set of time-domain FOM fitting tests were performed.

For the fitting tests, the reference voltage data $v[k]$ correspond to the random stage of the accuracy tests as the reference voltage signals presented in Figure 2.6. For all the ZARC elements and the implementations considered in the accuracy analysis, the associated parameters were fitted by minimising the mean square error between the reference voltage $v[k]$ and $v_x[k]$, which corresponded to $v_{RC}[k]$, $v_{OU}[k]$ or $v_{GL}[k]$ depending on the evaluated approximation. For all cases, the minimisation problem was solved in Matlab® using the default particle swarm optimisation (PSO) algorithm, implemented by the Matlab® function "particleswarm". The default PSO algorithm employs a number of particles automatically selected as the minimum between 10 times the number of parameters to be fitted and 100 particles; a function tolerance of 10^{-6}; and a maximum iteration number of 200 times the number of parameters to find [115].

The set of identified parameters changes depending on the approach evaluated. In the case of the GL-based implementations, the three parameters of the ZARC element, namely, R_{p1}, G_1 and ϕ_1, can directly be identified due to the nature of this implementation, where the time response of the FO element is directly approximated, as presented in Section 2.3.3. This can be observed in the schematic of the identification procedure presented in Figure 2.12c, where the parametrisation process takes the identified values of the ZARC parameters as inputs for generating the vectors required for the time-domain implementation. Similarly, for the OU approach, the direct identification of the ZARC element parameters from time measurements is possible due to the direct relationship between R_{p1}, G_1, ϕ_1 and the poles and zeros of the implemented integer-order transfer function, as introduced in Section 2.3.2. Figure 2.12b shows the implementation based on the OU approach, which was not modified for the fitting tests; only the source of the ZARC element parameters' changes, now being generated by the minimisation algorithm.

For the mRC approach, an initial frequency-domain fitting of the FO element impedance is required. For identification using time-domain measurements, this step cannot be performed. The resistance and capacitance values need to be fitted directly, as represented in the flowchart in Figure 2.12a.

On the one hand, for the OU and the GL approaches, the number of parameters to be identified was always 3, independently of the order n_{OU} or memory length L. On the other hand, the number of parameters to identify with the mRC approach increased with the order, being equal to $2n_{RC}$. This highlights the main drawback of the mRC approach: when fitting the time response of the FO element, overfitting issues may arise due to the high number of parameters.

For all the fitting tests, the mean of the relative error between the reference voltage and the response of the fitted approximation was computed as an indicator of the goodness of the time-domain fit. Additionally, the indicator of how close the obtained impedance is to the expected one in the range from 0.01 to 20 Hz is the following:

$$\delta_Z(\omega) = \frac{|Z_{ZARC}(\omega) - Z_{app}(\omega)|}{|Z_{ZARC}(\omega)|}. \tag{2.50}$$

Here, δ_Z corresponds to the relative distance between the impedance of the fitted approximation, called Z_{app}, and the one of the original ZARC element, Z_{ZARC}.

The results obtained for ZARC 3 are summarised in Figure 2.13 as a plot of the relative error in time against the one in frequency. Even if relative errors in time under 5% were obtained for multiple instances of each approach, similar results in frequency were only reached for OU and GL approximations. In the case of mRC-based approximations, a good fitting in time is not necessarily translated to a low distance between the approximation impedance and the original one. It is worth mentioning that the minimisation algorithm was not optimised, but despite this, good accordance between the original and approximated impedance was reached for the OU and the GL approximations and not for the mRC case. Similar results were reached for all the other ZARC elements, illus-

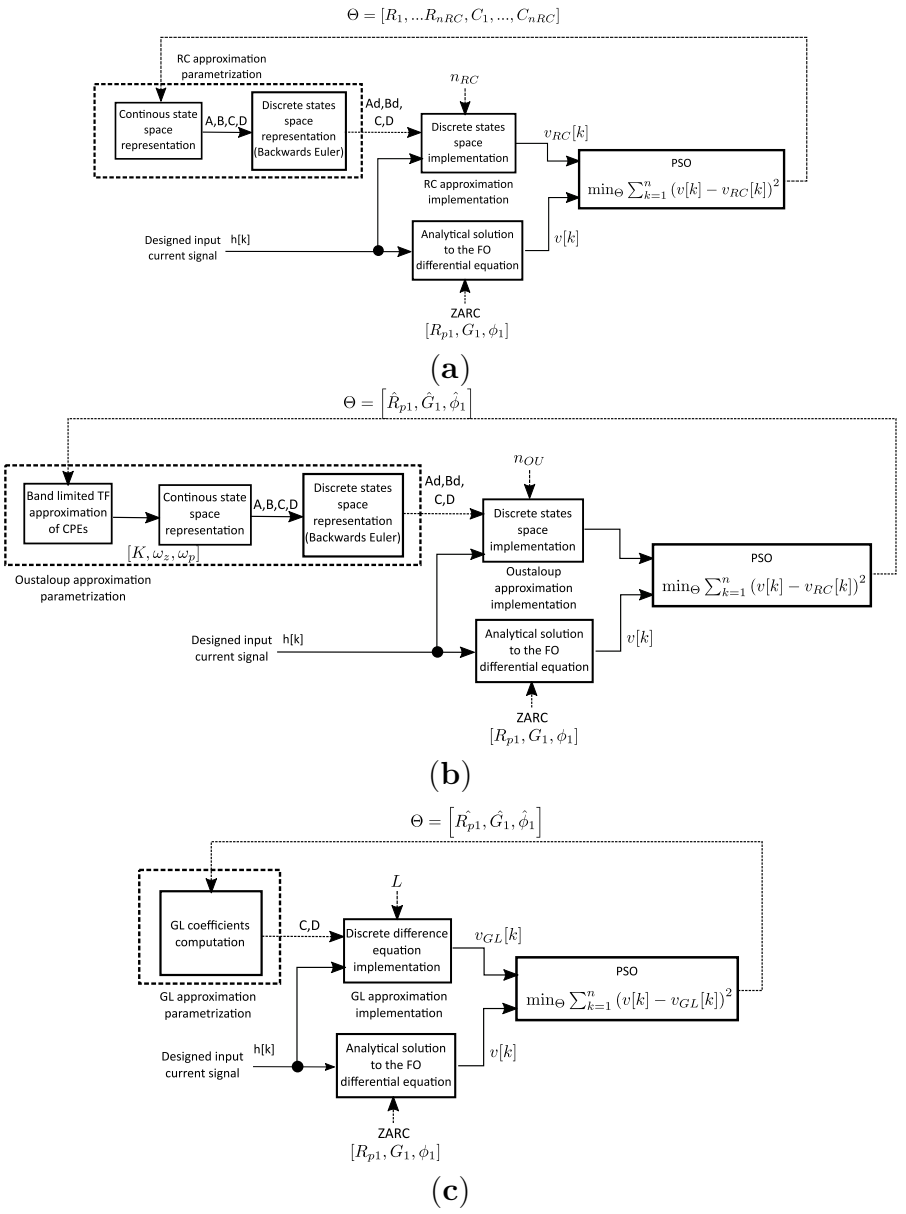

Figure 2.12: Block diagrams of the fitting procedures for the (**a**) mRC, (**b**) OU and (**c**) GL approximations.

trating how for the mRC approach, the lack of a direct relationship between the approximation parameters—namely, the resistance and capacitance values—and the ZARC impedance parameters reduces the possibility of identifying an approximation in time domain that also has a frequency response close to the real one.

An on-board-oriented implementation of these identification methods should address additional issues. One of them is the noise affecting the current and voltage measurements. Such noise contributes to causing a bias in the identified parameters, which should be compensated for with advanced fitting algorithms, as shown, for instance, in reference [116]. The noise compensation is worthy to be a matter of future study.

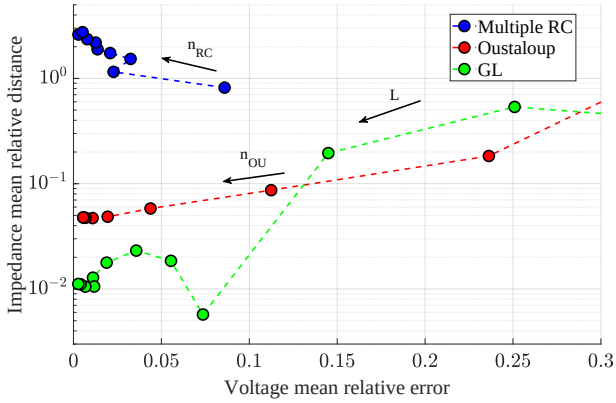

Figure 2.13: Fitting ZARC 3: average relative voltage error vs. average relative impedance distance.

2.4 Conclusions

In this chapter, initially, a fitting procedure for the parameters of impedance models was presented. This procedure is based on the minimisation of the sum of the squares of the euclidean distances between experimental and approximated values for the impedance points at the frequencies of interest. Approximations

with maximum relative distances to the experimental values under 2% were obtained, when the procedure with the proposed initial conditions was tested using experimental EIS data from the "Sandia Cell EIS Testing Data" repository.

Additionally , the three main approaches adopted in the literature for the implementation of the time-domain response of battery FOMs were introduced and compared in terms of accuracy, computational requirements and suitability for the time-domain identification of battery impedance. The study was performed in a simulation framework with six different ZARC elements, which are normally used for the approximation of battery impedance in the middle-frequency range. The reference solution was an analytical expression for the response of a ZARC element under a multiple-step current. The proposed expression, obtained using FO calculus theory, was used for generating the reference data required for the accuracy analysis of the considered implementations. Even if the discussion focused on ZARC elements, the results can be extended to the Warburg element and to the total battery impedance.

The primary results of the study can be summarised as follows.

- In terms of *accuracy under static conditions*, average relative errors under 0.1% were reached for all the evaluated ZARC elements using the three evaluated approaches. From the *computational complexity viewpoint*, these results were achieved with the mRC and OU approaches having similar computational requirements, whereas the GL approach often required a number of multiplications two orders of magnitude higher.

- In terms of *accuracy under dynamic conditions*, the mean relative errors converged to values in the same order of magnitude for the three approaches, when increasing the *complexity* of the implementation. The asymptotic errors were comparable for a fixed sampling time. For instance, the best mean relative error was around 2% using a sampling time of 0.01 s for all the methods.

- In terms of *suitability for identification from time-domain*

data, all approaches well fit the time-domain voltage responses of the ZARC elements, with errors under 5%.

- However, in terms of *suitability to reproduce the frequency-domain impedance spectrum* from the parameters achieved in the time-domain identification, only OU and GL approximations reached errors of a few percent.

- The *best accuracy–complexity relationship* is offered by the mRC approach. It reached low error levels with the smallest computational burden. This should be the case as long as good fitting of the ZARC element in the frequency domain can be performed. This conclusion does not hold up if the starting point for the ZARC identification is time-domain measurements. In this latter case, the RC parameters may not lead to a correct frequency-domain response, and therefore, the best compromise for identification from time-domain data is represented by the OU approximation, which outperforms GL in terms of computational complexity.

The selection of the FOM implementation method depends on the application requirements. On the one hand, if the interest is only in the battery response simulation, the mRC approach offers the best accuracy–complexity compromise, which is desirable for real-time simulations oriented towards the validation of energy management algorithms. On the other hand, if the application requires accurate identification of the impedance parameters from time-domain measurements, the OU approach offers the best compromise among identifying the impedance model parameters, the complexity and the accuracy requirements.

Chapter 3

Application Domain Extension of Incremental Capacity-Based Battery SoH Indicators

This chapter addresses the open issues identified for the application of the IC analysis under normal usage conditions. In this study, the technique is applied under the following conditions that, to the best of author's knowledge, have never been used before for this kind of analysis.

- The current levels used for the IC are significantly higher than those used in the pseudo-equilibrium condition, and higher than the large majority of those used in all the previously cited works. These charging currents levels are closer to the ones used in practical applications. For the sake of brevity, hereinafter, these currents will be referred as High-Current IC (HCIC) to highlight that they are far beyond the pseudo-equilibrium condition.
- The battery cycling is characterised by a randomised current profile that differs among batteries, with battery groups sharing only the probability distribution of the ageing patterns.

This kind of usage profile is much more general than the uniform one used in the literature and it is more suitable to identify a general and robust HCIC-related health indicator.

- The number of batteries included in the considered dataset is much higher than those used in all the works cited above.

More specifically, the analysis focuses on various randomised usage batteries ageing experiments, in which the batteries are cycled with charge and discharge current levels varying with time by taking randomly selected values. Periodically, a high-current characterisation test is performed, allowing us to compute the battery actual capacity during discharge and the HCIC at 1C current level in charge mode. The reference dataset is the *NASA randomised battery usage dataset* [117], including tests on 28 batteries subject to 7 different randomised cycling patterns. On the basis of the HCIC curves, computed for batteries from fresh state down to aged around 80 %, some IC-curve features are extracted from raw battery data. The adopted feature extraction procedure is inspired by the techniques used for low-current IC in laboratory environment, taking benefits of the results on [34] and [67] for the filtering stages. Two filtering stages are included, one for the voltage signal and the other for the partial capacity derivative with respect to the voltage, deeply affecting the IC curve shape. An IC curve characterised by only one main peak is obtained, after tuning the two stages for the NASA dataset. From this curve, three features are extracted: the peak position, peak height and peak area. The sensitivity of the features with respect to various computational parameters is also investigated, optimising the extraction. Then, the correlation between the features and the capacity change due to battery ageing under various cycling conditions is studied, finding that the area under the main peak of the HCIC curve is the most promising battery capacity indicator for the health assessment in the presence of random cycling patterns.

To further confirm these results, the HCIC analysis is applied to another set of 8 batteries, from The University of Oxford Battery Intelligence Laboratory, differing from the ones in the NASA

dataset in terms of the cell technology, shape, and capacity, and aged with a fixed cycling pattern typical of a driving schedule. Despite the strong differences, the results confirm the robustness of the peak area as a general IC-related battery capacity indicator. The performance of the HCIC peak area as health indicator is compared with an ohmic resistance-based method, highlighting the higher robustness of the proposed approach. The advantages and drawbacks of the proposed method are briefly summarised in Table 1.1 with respect to the state of the art.

3.1 The Reference Dataset

The randomised battery usage dataset [117], from the NASA Ames Prognostics Data Repository, contains cycling data considering a random usage of batteries under various operating conditions. 28 Lithium-Cobalt oxide-graphite (often called LCO) 18650 cells from LG Chem, having cutoff voltages of 3.2 V/4.2 V, are grouped in 7 sets of 4 batteries each. The cells are characterised by high energy density, a short lifetime and a nominal capacity $Q_n = 2100\,\mathrm{mA\,h}$. The full capacity is close to its nominal value for all cells in fresh state, and it decreases to a minimum value of 800 mA h in about 150 days.

The main load profile for each battery is called *Random walk* (RW). In each particular RW, the current levels are randomly selected in a specific current range, for instance between −4.5 A and 4.5 A, or between 0.5 A and 4 A. The duration of the current pulses can either be fixed *a priori*, or randomly selected in a specific time range. Within the same set, the RW current profile of the cells differs the one another, even if they are all generated according to the same rule. Due to the restrictions imposed by the current profile generation rules, an acceptable degree of uniformity in the obtained degradation tendencies is expected between the batteries in each group.

Periodically, a set of *Characterisation tests* is performed after a number of RW cycles, which is variable depending on the experi-

ment. It usually consists of at least one full charge or one reference discharge. The reference charge/discharge cycles are aimed at computing the actual battery full capacity in a reference condition. This study uses the A h battery full capacity Q, obtained by numerically integrating the battery current with the trapezoidal integration rule. Table 3.1 presents brief descriptions of the test protocols used for the seven battery groups.

It is worth mentioning that the RW profiles employed for cycling battery groups 2 and 4-7 include full 1C CC-CV charge and randomised full CC discharge subcycles, the profiles for group 3 include partial 1C CC-CV charges (with randomly selected duration) and randomised full CC discharges and the batteries in group 1 are cycled with a sequence of charge and discharge steps randomly selected, accounting for a sequence of partial charges and discharges.

In order to evaluate the average impact of the load profile (and, therefore, of the operating mode) on the battery degradation tendency, the total Ampere-hour throughput computed at 80 % capacity is used as a reference number. The throughput of batteries belonging to groups 1 and 3 overtakes 1000 A h, which is much greater than the one for groups 4-7. This fact can be ascribed to the specific operating mode characterising groups 1 and 3, which avoids consecutive full-charge and full-discharge phases thanks to the presence of partial charges and discharges. Conversely, batteries in groups 4-7 work with a regular Depth-of-Discharge (DoD) ranging from 0 to 100 %, with deep charge and discharge, which appears as the most important battery stress factor, leading to a faster degradation in terms of equivalent full cycles [118]. Average temperature and discharge rate variations were also introduced in groups 4-7, but the differences between them were not sufficient to produce such a deep degradation effect.

Table 3.1: Test protocol descriptions for the battery groups in the NASA RW dataset

Group (cells id)	Test protocol description
1 (RW9 - RW12)	Continuously operated using a randomised sequence of charging/discharging currents between −4.5 A and 4.5 A lasting 5 min each. A series of reference *Characterisation tests* is carried out after 1500 current steps.
2 (RW3 - RW6)	Continuously operated by repeatedly charging them up to 4.2 V, and then discharging them down to 3.2 V using a randomised sequence of discharging currents between 0.5 A and 4 A. A series of reference *Characterisation tests* is carried out every 50 cycles.
3 (RW1 - RW2, RW7 - RW8)	Continuously operated by repeatedly discharging them down to 3.2 V using a randomised sequence of discharging currents between 0.5 A and 4 A. After each RW discharge, they are charged using a randomly-selected current pulse having a duration between 30 min and 3 h. A series of reference *Characterisation tests* is carried out every 50 cycles.
4 (RW25 - RW28)	Continuously operated by repeatedly charging them up to 4.2 V and then discharging them down to 3.2 V using a randomised sequence of discharging currents between 0.5 A and 5 A, while holding the ambient temperature at approximately 40 °C. A customised probability distribution, skewed towards selecting high currents (the peak probability is set at 4.0 A), is used in this experiment to select a new load set point every 1 min during RW discharging operation. A series of reference *Characterisation tests* is carried out every 50 cycles.
5 (RW17 - RW20)	Similar to the one performed for Group 4, but with uncontrolled ambient temperature that ends up being, on average, lower than 40 °C.
6 (RW21 - RW24)	Similar to the one performed for Group 4, with custom probability distribution designed to be skewed towards selecting low currents (the peak probability is set at 2.0 A).
7 (RW13 - RW16)	Similar to the one performed for Group 4, with custom probability distribution designed to be skewed towards selecting low currents, with uncontrolled ambient temperature that ends up being, on average, lower than 40 °C.

3.2 High-Current Incremental Capacity Analysis and Features Extraction

3.2.1 High-Current Incremental Capacity Computation

In order to find a suitable IC-related indicator of the overall capacity degradation with practical interest for batteries in random usage, the HCIC computed during the CC phase of the battery charge process is employed. This kind of charging process is used in many applications, from EV-charging to stationary systems.

The HCIC curve is computed and processed by taking inspiration from what is done for the low-current IC applications, both in terms of features computation approaches as well as of signal filtering. Various stages are required to generate the HCIC curve from the voltage v and current i signals, acquired during the CC section of the battery charge. The HCIC curve extraction procedure proposed in this work can be described as follows:

- Initially, a Savitzky-Golay (SG) filter is applied to the voltage data. The SG filter operates as a moving window filter by replacing each data point with the result of a least-squares fit of an order N-polynomial function performed in a neighbourhood of the same point, namely the window. This approach filters out the noise, preserving the position of crucial points of the curve [119]. The application of this filter to the voltage signal is particularly suitable for IC analysis due to the high sensitivity of differential curves to the discretisation resolution and measurement noise [43]. In the NASA dataset, the voltage data of the reference charge CC stage are affected by very little noise, but often consecutive voltage samples have the same numerical value due to discretisation. It was found empirically that a window of 5 samples was enough for solving this problem without major modifications of the other data

points. A higher value of this window may be necessary in the presence of more significant measurement noise. Schafer et al. in [119] pointed out that an under-smoothing problem may occur when the order of the SG filter approaches the window size. Therefore, in our case, a second-order polynomial function optimises the filter performance while keeping the lowest possible order.

- The battery A h charge q (or, alternatively, partial capacity) is computed by numerically integrating the battery current i by a trapezoidal scheme.

- Once the filtered voltage v_{SG} and the partial capacity q vectors are available, the IC points are computed using the following backward difference approximation for the capacity derivative with respect to the voltage:

$$\mathrm{IC}_0(k) = \frac{dq}{dv_{\mathrm{SG}}}(k) = \frac{q(k) - q(k-1)}{v_{\mathrm{SG}}(k) - v_{\mathrm{SG}}(k-1)}. \tag{3.1}$$

  where k is the discrete time step.

- In order to extract useful information from the obtained IC data, such as the peaks positions and heights, a smoothing stage is required. In the proposed framework, this smoothing stage corresponds to a Gaussian-Weighted Moving Average filter (GWMA). The GWMA outperformed simpler alternatives, like the moving average one or the SG, because it reaches the desirable smoothing levels with a very low distortion of the IC curve features, such as the peaks, by suitably tuning its window. The effectiveness of such an approach is confirmed by [67] for low-current IC.

For the analysis presented hereafter, the HCIC curve extraction procedure was implemented using Matlab®. The SG filtering stage is implemented with the function `smoothdata`, employing the second-order Savitzky-Golay method: `sgolay`. The same function was used for the implementation of the GWMA filter, but employing the Gaussian smoothing method: `gaussian`. This function

takes as argument the window w over which the moving average is performed. The relationship between the GWMA filter window w and the standard deviation σ of the Gaussian distribution used for computing the weights of the filter is: $w = 5\sigma$ [120].

3.2.2 High-Current Incremental Capacity Peak Features Extraction

The procedure described above can be repeated for all CC charge curves of the same battery. Each HCIC curve must be taken from a different *Characterisation test* and, therefore, it will be associated to a specific value of the battery full capacity Q. Figure 3.1 (a) shows seven smoothed IC curves $\mathrm{IC_G}$, corresponding to seven decreasing battery full capacity values for battery RW9. Each of them is above the 80 % of the initial full capacity Q_0.

The curves allow one to identify three main features that change with the capacity fading:

- the peak position PP;
- the peak height PH;
- the area PA under the peak, evaluated on an interval centered on PP and having semi-width ΔV, that is:

$$\mathrm{PA} = \int_{\mathrm{PP}-\Delta V}^{\mathrm{PP}+\Delta V} \mathrm{IC_G}(v_{\mathrm{SG}})\, dv_{\mathrm{SG}}. \tag{3.2}$$

Again, the integral is numerically evaluated with the trapezoidal integration rule. The features are represented in a pictorial way in Figure 3.1 (b).

It is worth to notice an important aspect of the peak area feature. Taking the area under the IC curve in a given voltage range, that is the integral of the IC curve over the same range, is in fact an inversion of the derivative defining the IC. Hence, the computed integral is an approximation of the partial A h capacity injected into the battery while its voltage is within the considered

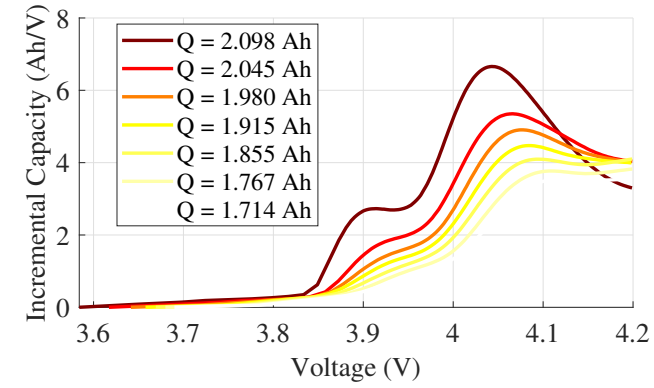

(a)

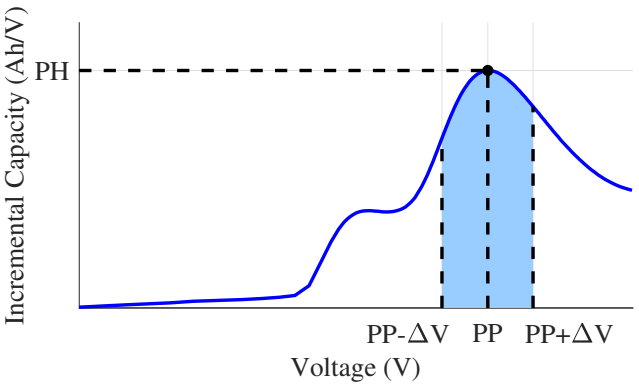

(b)

Figure 3.1: (a) IC plots obtained before reaching $0.8Q_0$ for RW9. (b) Peak position, peak height and peak area of a HCIC curve.

voltage range. The GWMA filtering stage may obviously affect this approximation, and its influence must be carefully investigated.

The flow chart of Figure 3.2 summarises the procedure used for extracting a HCIC curve and, from it, the features. The first part, highlights how to process the v and i signals to achieve the filtered IC curve, while the second part, including one stage, allows one to extract the proposed features (PH, PP, and PA) from the filtered IC curve.

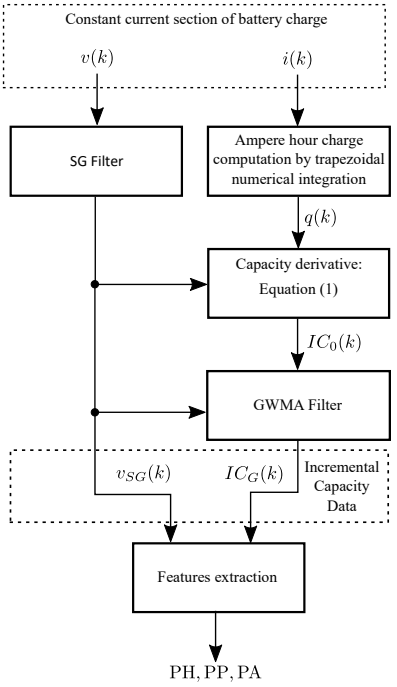

Figure 3.2: Block diagram of the proposed method for the HCIC features extraction

3.3 Application of the Method to the NASA Random Walk Dataset

3.3.1 Peak Features: Position, Height and Area

The IC curves obtained from the 1C reference charge cycles in the NASA random walk dataset contain one major peak, as shown in Figure 3.1. For all the 28 batteries considered in the RW tests, and for all the *Characterisation test* cycles available for each battery, the battery discharge capacity Q and the three IC features were evaluated. The PA was computed using $\Delta V = 50\,\text{mV}$. The choice of this value will be motivated in Section 3.3.2.

On the basis of these computations, a regressions analysis was performed to investigate how each feature PH, PP, and PA, is linearly related to the battery full capacity Q. In other words, a search for the most reliable capacity degradation indicator for the considered set of batteries was conducted.

Table 3.2 summarises the R^2 coefficient, that is the square of the correlation coefficient ρ, obtained for each linear fit of a capacity feature with respect to the battery full A h capacity Q in the typical battery first-life range. The coloured cell on each row highlights the maximum R^2 achieved in the line, that is also the best linear fit. Concluding that, for the large majority of batteries, 19 over 28, the PA feature clearly outperforms the others in terms of correlation with the capacity degradation. In some of the cases in which the PP is better correlated to Q with respect to PA, the PA fit R^2 coefficients are still over 0.75. Therefore, PA can be used as the main indicator of the battery degradation in the presence of a randomised load. In particular, the PA shows a good correlation coefficient for almost all batteries of the groups from 3 to 7.

The PA R^2 for batteries in group 2 are the lowest in Table 3.2. The feature PP seems to have a better correlation with Q for this group, but the values achieved are far below the best cases in the table. After checking the data points for the batteries in group 2,

an outlier point in the $Q - \mathrm{PA}$ data was identified, for $Q \simeq 1.6\,\mathrm{A\,h}$. The plot is not shown here for the sake of compactness. This value deeply affects the quality of the obtained linear fit, ending up with such low R^2 values. Removing manually this outlier point would produce results comparable to those of the other battery groups, rising up the R^2 over 0.9. This phenomenon can be due to errors in measurements of the capacity for that specific point in the battery group. In the following, rather than presenting modified data, the original values are still reported, discarding further discussion on the poor results achieved by this battery group.

3.3.2 Evaluating the Peak Area

The reference voltage window used in Table 3.2 for the PA computation is $2\Delta V = 100\,\mathrm{mV}$. Considering the right-shift of the peak with ageing, a higher value of ΔV may cause the integration interval to fall out of the available voltage range for an aged battery. Indeed, the peaks are located at relatively high voltages, very close to the upper voltage threshold that determines the transition from CC to CV charge control. In this zone, the higher ΔV the higher the probability of exceeding the voltage threshold. Therefore, in this latter case the PA cannot be computed, and it is worth not to use values of $\Delta V \geq 50\,\mathrm{mV}$, to ensure an accurate computation of the PA for all available curves, without loosing any point.

In order to investigate the sensitivity of the PA fit to the voltage integration window, the following three values for ΔV are considered: 25 mV, 37.5 mV, and 50 mV. The values of R^2 achieved in the fitting of the full capacity Q with respect to PA, $Q(\mathrm{PA})$, are compared in Table 3.3. Here, the highest value on each row is highlighted.

From a practical point of view, the fits for PA_1, PA_2, and PA_3 are computed on the same number of points. In these three cases, Table 3.3 shows that the larger the voltage interval considered, the better the fit, making PA_3, that is for $\Delta V = 50\,\mathrm{mV}$, the most suitable option for the estimation of the full capacity in the majority of cases.

Table 3.2: Square of the correlation coefficient (R^2) obtained for the linear fits of the capacity Q as a function of PH, PP, and PA, computed with $\Delta V = 50\,\mathrm{mV}$.

Group	Battery	PH	PP	PA
1	RW9	0.8712	0.9761	0.8783
1	RW10	0.907	0.9726	0.9117
1	RW11	0.9662	0.9775	0.9589
1	RW12	0.5593	0.5954	0.7793
2	RW3	0.7367	0.9248	0.8145
2	RW4	0.7153	0.8843	0.7645
2	RW5	0.681	0.9426	0.7738
2	RW6	0.8451	0.7989	0.8799
3	RW1	0.8211	0.1324	0.9861
3	RW2	0.9912	0.9566	0.9975
3	RW7	0.935	0.9581	0.9491
3	RW8	0.9508	0.9216	0.9525
4	RW25	0.9101	0.08292	0.9353
4	RW26	0.9488	0.8937	0.9657
4	RW27	0.9348	0.0262	0.9423
4	RW28	0.98	0.9231	0.991
5	RW17	0.9629	0.8592	0.9794
5	RW18	0.8896	0.9504	0.9509
5	RW19	0.91	0.7856	0.95
5	RW20	0.9803	0.818	0.9872
6	RW21	0.978	0.814	0.9927
6	RW22	0.9624	0.8002	0.9804
6	RW23	0.9816	0.2988	0.9832
6	RW24	0.9417	0.06529	0.9917
7	RW13	0.9837	0.9695	0.9868
7	RW14	0.9939	0.9765	0.9944
7	RW15	0.973	0.9795	0.9779
7	RW16	0.9713	0.9885	0.985

Table 3.3: Linear fit of the battery capacity Q as a function of PA for multiple ΔV values: R^2 coefficient.

Group	Battery	PA_1 25 mV	PA_2 37.5 mV	PA_3 50 mV
1	RW9	0.8731	0.8753	0.8783
1	RW10	0.9078	0.9094	0.9117
1	RW11	0.964	0.9617	0.9589
1	RW12	0.5286	0.5127	0.7793
2	RW3	0.7588	0.7836	0.8145
2	RW4	0.7267	0.7424	0.7645
2	RW5	0.7038	0.7337	0.7738
2	RW6	0.8417	0.8409	0.8799
3	RW1	0.8278	0.8352	0.9861
3	RW2	0.993	0.9953	0.9975
3	RW7	0.9402	0.9451	0.9491
3	RW8	0.9518	0.9524	0.9525
4	RW25	0.9208	0.9293	0.9353
4	RW26	0.9535	0.9566	0.9657
4	RW27	0.9424	0.9446	0.9423
4	RW28	0.985	0.9888	0.991
5	RW17	0.9693	0.9744	0.9794
5	RW18	0.91	0.9302	0.9509
5	RW19	0.9212	0.934	0.95
5	RW20	0.9828	0.9856	0.9872
6	RW21	0.985	0.9897	0.9927
6	RW22	0.9695	0.9754	0.9804
6	RW23	0.9833	0.9834	0.9832
6	RW24	0.9495	0.9554	0.9917
7	RW13	0.9856	0.9864	0.9868
7	RW14	0.9941	0.9944	0.9944
7	RW15	0.9731	0.9752	0.9779
7	RW16	0.9757	0.9807	0.985

3.3.3 Effectiveness of Using Peak Features

From its definition, the peak area can be considered as an approximation of a partial capacity, and the fit $Q(\mathrm{PA})$ can be seen as a way of evaluating the battery full capacity from an estimation of a partial one. Besides, the partial capacity evaluated as a peak feature, PA, is much more effective that other kinds of partial capacities evaluated in other voltage ranges far from the peak. Indeed, for these areas, the IC analysis could not be required, because the integration of the current can be carried out in a specific voltage window whose bounds could be fixed *a priori*.

In order to show that the choice of a peak-related area PA is the most effective one for a capacity fit, the NASA random walk dataset is analysed, computing IC curve areas in various off-peak voltage windows. These areas are denoted as S_{-3}, S_{-2}, S_{-1}, while S_0 stands for PA. All areas are computed on voltage windows A_{-k} having semi-width $\Delta V = 50\,\mathrm{mV}$, and located before PP. The area S_1 is located after PP, but for some curves it sometimes exceeds the voltage range and cannot be evaluated. A graphical representation of the range selection and area computation is given in Figure 3.3(a) on a sample IC curve.

First of all, for a sample battery (RW9), the distribution of data points is checked for all the considered voltage ranges. The distribution is plotted in Figure 3.3(b). The large majority of points, that is, the highest information density, is located around the peak. Considering the ranges from A_{-3} to A_0, the analysis is carried out by computing the area for all the available 1C IC curves. The results of the linear fit of Q with respect to these new features are summarised in Table 3.4, where, again, the R^2 of each fit is reported. The Table clearly shows that, again, for the majority of batteries, 21 over 28, the peak area $S_0 = \mathrm{PA}$ keeps being the best feature for the fit. This may be explained by thinking of the areas under the HCIC curve as partial capacities. In this case the partial capacity associated to the curve main peak covers the highest fraction of the full capacity. Comments on group 2 results have already been provided in the previous subsection, so there is

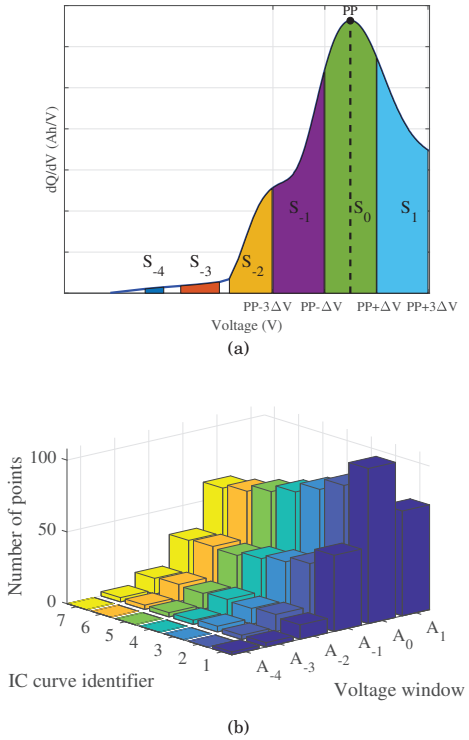

Figure 3.3: (a) Example of the voltage range split considered for the area position analysis. (b) IC curve points distribution between the considered voltage areas for RW9.

no reason to be worried by the poor results achieved by group 2 in Table 3.4.

3.4 Battery Capacity Degradation as a Function of HCIC Features

The results of the previous section show that the most promising battery health-related HCIC feature in the presence of RW profiles is PA, that is the area under the main peak covering a voltage range of $2\Delta V = 100\,\text{mV}$ centred on the peak position. With the

Table 3.4: Linear fit of the battery capacity Q as a function of areas computed in correspondence of various 100 mV-width voltage ranges: R^2 coefficient.

Group	Battery	S_{-3}	S_{-2}	S_{-1}	S_0
1	RW9	0.6794	0.7113	0.7676	0.8783
1	RW10	0.4104	0.5112	0.7298	0.9117
1	RW11	0.3381	0.5074	0.7479	0.9589
1	RW12	0.2618	0.1303	0.497	0.7793
2	RW3	0.9233	0.939	0.7541	0.8145
2	RW4	0.907	0.9237	0.7956	0.7645
2	RW5	0.8323	0.8848	0.6059	0.7738
2	RW6	n.a.	n.a.	0.9213	0.8799
3	RW1	0.03076	< 0.01	0.8994	0.9861
3	RW2	0.5839	0.7846	0.8991	0.9975
3	RW7	0.6269	0.8388	0.8785	0.9491
3	RW8	0.9014	0.8791	0.9067	0.9525
4	RW25	n.a.	n.a.	0.9275	0.9353
4	RW26	n.a.	n.a.	0.6454	0.9657
4	RW27	n.a.	n.a.	0.7751	0.9423
4	RW28	n.a.	n.a.	0.83	0.991
5	RW17	n.a.	n.a.	0.953	0.9794
5	RW18	n.a.	n.a.	0.9943	0.9509
5	RW19	n.a.	n.a.	0.9536	0.95
5	RW20	n.a.	n.a.	0.9741	0.9872
6	RW21	n.a.	n.a.	0.8644	0.9927
6	RW22	n.a.	n.a.	0.9226	0.9804
6	RW23	n.a.	n.a.	0.8078	0.9832
6	RW24	n.a.	n.a.	0.9234	0.9917
7	RW13	n.a.	n.a.	0.9923	0.9868
7	RW14	n.a.	n.a.	0.9108	0.9944
7	RW15	n.a.	n.a.	0.9505	0.9779
7	RW16	n.a.	n.a.	0.9189	0.985

goal of battery health estimation in mind, an investigation of all the relationships of Q with PA was conducted for all available batteries in the NASA random walk dataset. In the following graphs, for each battery, the values of PA are normalised by computing the ratio between PA and PA_0, that is the fresh-state PA value. This normalisation allows to compare the results and superimpose the graphs of different batteries. The symbol PA is also used for the normalised quantity.

3.4.1 Peak Area as a Feature for the Capacity Estimation

From the NASA dataset, all the HCIC curves are processed to evaluate PA values, and associate them to the actual full capacity Q, getting several $Q - \text{PA}$ pairs and, in whole, a $Q(\text{PA})$ function for each battery. Then, for each battery, a linear fit using the `polyfit` Matlab® function is performed for the $Q(\text{PA})$ function for each battery. The results of the fitting are summarised in Table 3.5, where the linear fit slope, intercept and R^2 are shown for each battery. Obviously, the R^2 column coincides with the one in Table 3.2. For 22 out of the 28 batteries, the fit is very good, with R^2 values over 0.9, showing a satisfactory correlation between Q and the normalised PA in 78.57 % of the cases. This number rise up to over 90 % when excluding group 2, for the reasons discussed in Section 3.3.1.

The $Q(\text{PA})$ fits are plotted in Figure 3.4. For the sake of compactness, the odd plot of group 2 is omitted. The linear fitting lines are almost parallel the one another for various battery groups, especially for groups 1 and 4-7. The slopes of the fits for batteries in group 3 are much more dispersed, causing intersections in their plots. This could be due to the peculiar charge pattern, characterised by frequent partial charges of randomised duration. From a practical point of view, the batteries are rarely fully charged, and operate on different average DoD, possibly yielding drastically different degradation rates.

Table 3.6 shows the average and standard deviation of the

Table 3.5: Experimental data and linear fits of the battery capacity Q as function of the normalised PA computed with $\Delta V = 50\,\mathrm{mV}$.

Group	Battery	Slope	Intercept	R^2
1	RW9	0.8518	1.3061	0.8783
1	RW10	0.9088	1.2440	0.9117
1	RW11	0.9648	1.1718	0.9589
1	RW12	0.8881	1.2878	0.7793
2	RW3	1.0858	0.8698	0.8145
2	RW4	1.0920	0.8543	0.7645
2	RW5	1.0912	0.8456	0.7738
2	RW6	1.0354	0.9217	0.8799
3	RW1	0.9070	1.0671	0.9861
3	RW2	1.1908	0.8047	0.9975
3	RW7	1.1627	0.8606	0.9491
3	RW8	1.3875	0.6197	0.9525
4	RW25	1.5603	0.6358	0.9353
4	RW26	1.5353	0.6270	0.9657
4	RW27	1.5845	0.5962	0.9423
4	RW28	1.6868	0.4053	0.9910
5	RW17	1.4592	0.6833	0.9794
5	RW18	1.5483	0.6201	0.9509
5	RW19	1.6422	0.5121	0.9500
5	RW20	1.5705	0.5609	0.9872
6	RW21	1.5807	0.5669	0.9927
6	RW22	1.5941	0.5652	0.9804
6	RW23	1.5266	0.6104	0.9832
6	RW24	1.5036	0.6006	0.9917
7	RW13	1.6951	0.4188	0.9868
7	RW14	1.5714	0.5291	0.9944
7	RW15	1.4888	0.6019	0.9779
7	RW16	1.7539	0.3374	0.9850

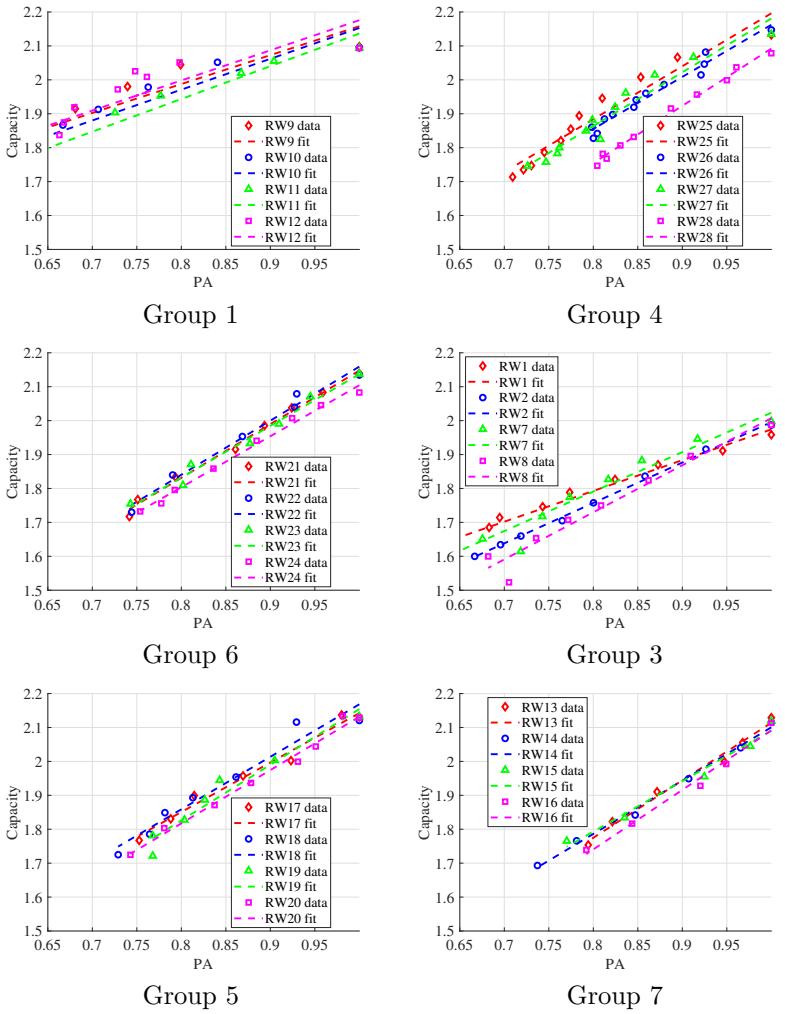

Figure 3.4: Linear fits for capacity Q as a function of the normalised peak area PA. Plots for Group 2, also characterised by an outlier point that affects the presented results, are not shown for the sake of compactness.

Table 3.6: Analysis of the battery group slope of the linear fitting of Q as function of the normalised PA. Average and standard deviation of the capacity.

Group	Average slope	Standard deviation (%)
1	0.9034	5.2272
2	1.0761	2.5341
3	1.1620	16.9728
4	1.5917	4.1766
5	1.5551	4.8501
6	1.5512	2.7798
7	1.6273	7.3510

slopes within each battery group. For the five battery groups 1, 2, 4, 5 and 6, the standard deviation is below 6 %. This enables the generalisation of the relationship Q(PA) from the battery level to the group level, with a single linear equation. This statement is further reinforced by the inspection of the Q(PA) plots for the batteries in each group shown in Figure 3.4. This result also highlights that the PA is a good capacity indicator even in the presence of the various degradation stress factors mentioned in Section 3.1.

Furthermore, considering the groups from 4 to 7, the overall standard deviation of the slopes falls to 5.01 %, showing that a further grouping can be made to obtain a single model representing the whole set of 16 batteries. These groups are rather similar in terms of load and recharge, but take into account a change in the temperature and average current, with a limited impact on the Q(PA) relationships. The full capacity Q estimated using the relationship Q(PA) can be used for the computation of the SoH, using (1.1), where Q is the actual battery capacity, and Q_0 is a reference value. For instance, Q_0 can be chosen as the nominal capacity Q_n. This value is the same for all the batteries in the dataset, and its use in (1.1) yields to a scale change in all graphs of Figure 3.4. A more accurate definition of SoH, much more related to each battery, could be obtained by choosing Q_ref as the battery fresh-state capacity Q_0. This value is computed for the

first available reference discharge cycle. In this case, the same normalisation factor holds for all points of a single battery, but each battery has its own normalisation factor, and they differ from one another. This makes the fresh state point of each battery curve the point at normalised PA = 1 and SoH = 1.

Assuming $Q_{\text{ref}} = Q_0$ for all batteries, the linear fits for the SoH(PA) relationships are generated. Obviously, ending up with the same R^2 factor already computed for Q(PA) relationship and reported in Table 3.5. The reason of this perfect match is that Q and SoH differs from one another from a y-axis scale change. Therefore, the slope and the intercept change from Q to SoH, but the fit accuracy is kept equal. The detailed results, that from a graphical point of view look very similar to those presented for the capacity, are omitted for brevity. By computing the slope dispersion for the SoH(PA) fits for all battery groups, very similar results to those reported in Table 3.6 for Q(PA) fits were found. The differences with respect to Table 3.6 are within 1 %.

3.4.2 Sensitivity of the Fit with Respect to the GWMA Filter Window

Finally, it is worth to investigate the sensitivity of the Q(PA) relationship with respect to the computation parameters. In particular, let us analyse the impact of a variation in the value of the GWMA filter window w over PA. For all the unfiltered HCIC curves obtained from the dataset, filtered versions using voltage windows $w = 75\,\text{mV}$, $100\,\text{mV}$, and $125\,\text{mV}$ are computed. Then, for each filtered HCIC curve, the peak feature PA, considering a voltage integration window equal to $2\Delta V = 100\,\text{mV}$, is computed. In this way, three values for PA are obtained and used to compute the corresponding linear fits.

The results achieved for one of the battery groups (group 6) are depicted in Figure 3.5. They look very similar to those achieved for all other groups, not reported here for the sake of compactness. The tendencies in the variation of PA with battery degradation are very well preserved. Both slopes and intercepts are affected

by tiny variations, such that the linear fits are extremely close the one another for each battery. This allows us to conclude that the PA feature is almost insensitive with respect to the GWMA window in a neighbourhood of the voltage range used to compute the peak area. After a similar analysis for the other peak features: PH and PP, analogous sensitivity results were obtained. It is worth mentioning that the validity of these results is limited to the analysed dataset. In the case of HCIC curves with narrower peaks, the GWMA window should be tuned according to the typical peak width to avoid an undesirable peak flattening.

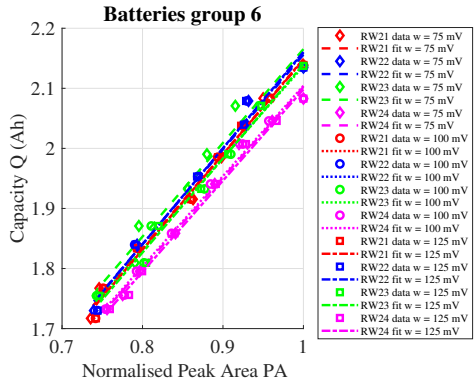

Figure 3.5: Linear fits for Capacity as a function of the selected peak area normalised obtained for HCIC filtered using different windows for the Gaussian filter - Group 6.

3.5 Evaluation of the Method Performance

3.5.1 Application of the Method to a Second Dataset

The presented HCIC analysis technique was also applied to the *Oxford Battery Degradation Dataset 1* [121, 122], in order to illustrate

the suitability of the peak feature PA as a capacity indicator also for batteries cycled and tested under conditions different from the ones present in the NASA dataset. The Oxford dataset contains battery ageing data from 8 small Lithium-Nickel Manganese Cobalt oxide pouch cells reference Kokam SLPB 533459H4, with a nominal capacity of 740 mAh. All the cells were tested in a thermal chamber at 40 °C and exposed to the same cycling profile: a CC-CV charging stage, followed by a drive cycle discharging stage that was obtained from the urban Artemis profile. Characterisation measurements were taken every 100 cycles, by performing 1C and C/20 CC charge and discharge cycles.

For the 8 cells in the Oxford dataset the procedure introduced in subsection Section 3.2.1 was applied, taking the 1C reference charge cycles data as input and obtaining HCIC curves as the ones presented in Figure 3.6 for each battery. A visual comparison between the IC curves presented in figure Figure 3.6 with those in Figure 3.1, allows one to conclude that the main peaks for the Oxford cells curves are in general narrower and appear at lower voltage values, highlighting the effects of the differences in the used cells and test conditions. In terms of ageing the effects over the curves are the same in both datasets, the main peak presents a shift towards higher voltages and a height decrease.

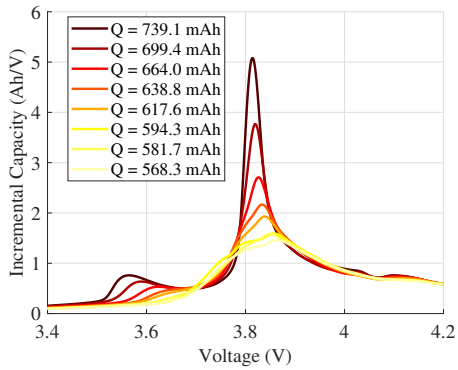

Figure 3.6: IC plots obtained for the cell 1 in the Oxford dataset

It is worth mentioning that the value for the SG filter window

had to be increased to 15 samples, due to the higher noise content of the voltage measurements in the Oxford dataset. Additionally, as the peaks obtained in the Oxford dataset are narrower, in order to have a filtered IC curve that represents better the area under the curve of the original data, a smaller window size of 40 mV is used for the GWMA filter.

The same procedure applied in subsection 3.3.1 for the batteries in the NASA dataset, was also applied to all cells in the Oxford dataset, by evaluating the discharge capacity Q, and the peak features PP, PH, and PA computed with $\Delta V = 50\,\text{mV}$, and investigating the correlation between Q and the peak features. Again, the PA is characterised by the best correlation with Q for this set of batteries, with R^2 coefficients over 0.99 for all the cells but cell 2 (0.97) and cell 5 (0.92).

For the sake of comparison, Figure 3.7 depicts the values of the SoH versus the normalised PA taken from both datasets. For the range of SoH over 0.8, the relationship between the normalised peak area and the SoH is similar for the batteries in both datasets. Indeed, the slopes of the linear fits of the Oxford dataset cells are close to those of the NASA dataset groups 1-2-3, characterised by fully random stages. The cycling profiles of these groups in the NASA dataset are the closest ones to the Artemis driving profile. The low dispersion of the Oxford data can be ascribed to the same cycling profile being used in a repeated way, with no randomisation, for all batteries in this set. The obtained results demonstrate the possibility of extracting the studied peak feature and using it as a promising capacity indicator for batteries of a different technology and with a different usage pattern with respect to those initially considered in this thesis. Only a few modifications of the filter parameters are required to successfully repeat the procedure.

It is worth mentioning that, in the stream of Section 3.4.2, the sensitivity analysis performed on this new dataset confirms the previously obtained results, provided that the analysis is performed with GWMA window values proportional to those ones reported in Section 3.4.2.

The usage pattern adopted in the Oxford dataset is based

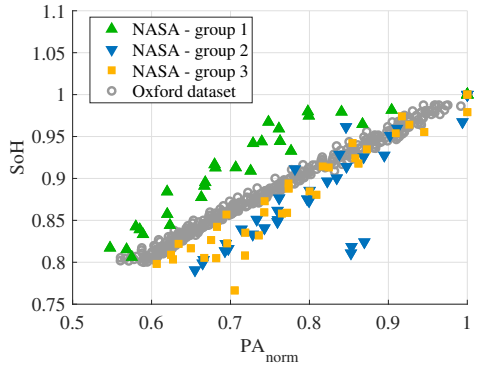

Figure 3.7: SoH vs normalised PA from the Oxford dataset (grey circles) compared with those from the NASA dataset, groups 1-2-3.

on a driving profile, highlighting the good applicability of the methods also in vehicular applications. Vehicles may interact with modern power grids according to the well-known vehicle-to-grid (V2G) and grid-to-vehicle schemes, including additional discharge or charge phases. According to Petit et al. [123], a strong V2G scenario is characterised by a full discharge of the battery due to the driving and grid requirements, a rest and, then, a full charge. Such a profile is far from the ones of the Oxford Dataset 1, but resembles the cycling profiles employed in groups 4-7 of the NASA RW dataset used in the previous Sections. The main difference between them lies in the length of the rests, which are longer in the strong V2G scenario. Then, the results obtained in this work, associated to the effect of the average operating DoD on the battery degradation and over the PA capacity estimation, may be extended to a V2G scenario where the cycle ageing is dominant, that is, the PA keeps being valid as a capacity indicator. Unfortunately, the calendar ageing associated to the rest periods, which is integral to the discussion of the effect of V2G schemes on the battery life [123, 124], cannot be evaluated on the available dataset, as the rest periods are short and fixed, and no conclusion can be drawn in this regard.

3.5.2 Comparison Between HCIC and Ohmic Resistance

The effectiveness of the HCIC PA as SoH indicator was additionally assessed by comparing its performance with the battery ohmic resistance method, listed in Table 1.1 as one of the experiment-based methods. For given SoC and temperature conditions, the approximated battery ohmic resistance is well-known to be directly related to the capacity fade [27].

Several methods are available to evaluate the ohmic resistance: pulsed current tests, EIS, dynamic model fitting, and observer-based estimation are some of the popular ones. For this study, the characteristics of the available battery usage data allowed us to use the pulsed current test-based approach, as introduced in [125]. This method is very simple, but requires a fast sampling of the voltage and current signals, which is actually met by the available experimental data. Alternative approaches have more complex requirements in terms of the operating conditions and signal characteristics, and therefore have not been chosen. The ohmic resistance R_Ω is approximated by the ratio between the variations in voltage Δv and current Δi, when the current pulse is applied: $R_\Omega = \Delta v / \Delta i$. Barai et al. suggest that a good approximation requires a short sampling time, typically below 100 ms [125]. The periodic characterisation of the NASA RW dataset batteries include a CC 1 A discharge, performed immediately after the reference charge employed for the HCIC computation, with a typical sampling time of 40 ms. As the current pulse of interest is always applied after a full charge, a SoC condition of 100 % is always met for the resistance computation. These conditions are good to compute R_Ω at 100 % SoC.

The computation of R_Ω was performed for almost all batteries in correspondence with the HCIC computation, thanks to the high uniformity of the sampling time, normalising the results with respect to the initial value of R_Ω for each battery. For the sake of example, a plot of Q as a function of R_Ω for batteries in Group 6 is shown in Figure 3.8, where the inverse linear relationship is

evidenced. Similar results were obtained for almost all the battery groups, but they are not shown for the sake of compactness.

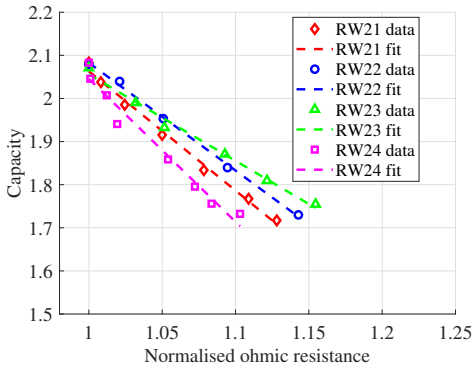

Figure 3.8: Linear fits for capacity as a function of the normalised ohmic resistance computed in a reference discharge pulse (group 6).

Table 3.7 summarises the average results for all battery groups. A few batteries were excluded from this analysis due to an evident inconsistency in the sampling time, which is far from the 40 ms that characterises the majority of cases (RW7, RW19, RW28). For those atypical cases, it was not possible to compute R_Ω in a consistent way. For almost all groups, the average R^2, which is obtained for the linear fittings of Q as a function of the R_Ω, is always under the average one obtained for the PA fittings of Table 3.5. The mismatch from the two is always under 6%, except for group 1, where the results for RW12 are considerably lower than those for all the other batteries within the group.

On average, the PA seems to slightly outperform R_Ω as a capacity indicator. This average behaviour can be ascribed to the high sensitivity to noise of the R_Ω computation, which brings down the average R^2. In most cases, lower values for the standard deviation of the fittings slopes were observed for PA (this holds in particular for groups 4-7), showing that the proposed HCIC PA has a higher generalisation potential in each group. Despite the advantages shown by the PA indicator, it is worth mentioning that the ohmic

Table 3.7: Analysis of the battery groups slope and R^2 of the linear fitting of Q as function of the normalised ohmic resistance.

Group	Average R^2	Average slope	Slope standard deviation (%)
1	0.7729	-1.6892	34.9945
2	0.8017	-3.2188	10.2868
3	0.9329	-3.3799	14.2894
4	0.9090	-2.3782	41.8735
5	0.9093	-2.6683	31.4144
6	0.9869	-2.6470	20.6562
7	0.9299	-2.4608	25.6150

resistance method offers complementary advantages for health estimation. Indeed, even if it has shown higher sensitivity to noise, its simplicity both in terms of implementation and requirements make it attractive for a more reliable combined estimation.

3.5.3 Application on a Fast Charging Scenario

In order to extend the performance evaluation of PA as a SoH indicator, the method was also applied to a set of batteries aged under a multistep fast charging scenario. The study is conducted over 94 batteries from a publicly available dataset shared by the Toyota research institute, including the data from 140 batteries cycled under fast-charging conditions [37].

3.5.3.1 Toyota fast charging dataset description

The dataset includes data for 140 Lithium-Iron-Phosphate (LFP) /graphite battery cells cycled under fast-charging conditions [37, 126]. The cells have a nominal capacity of 1100 mA h and a nominal voltage of 3.3 V. The upper and lower cutoff voltages are 3.6 V and 2.0 V, respectively.

The batteries underwent a cycling profile characterised by the presence of fast charging, while placed in a forced convection thermal chamber set to 30 °C. An example of a typical cycling profile is shown in Figure 3.9 (the example refers to battery 36 of the dataset). The profile includes the following phases.

1. Fast charging in CC mode using one or two current steps (red and green steps in Figure 3.9);
2. rest phase (very small current) lasting typically around a minute;
3. 1C CC charging followed by a constant voltage (CV) stage, ending when the current is sufficiently low;
4. discharge at 4C down to the lower cutoff voltage;
5. rest phase before the next cycling step, having typical lengths in the order of some minutes.

Phase 1 characterises the experiment. Each policy is described by a string with the format:

$$\{C_1\}\texttt{C-}\{q_1\}\texttt{PER\_}\{C_2\}\texttt{C}.$$

Here, the three fields $\{\cdot\}$ define the experiment policy for each battery. The CC value C_1 is used to charge the battery in the first step up to the SoC value q_1, which is expressed as a percentage. The second CC step current C_2 brings the battery up to 80 % SoC. In the case of a single charging step, C_1 is set equal to C_2, and $q_1 = 80\,\%$. The values for C_1 and C_2 are formatted as `x_d`, where `x` is the integer part and `d` is the decimal part.

Figure 3.10 shows a typical cycle for battery 1, which is characterised by a single fast charging step of 3.6C up to 80 % SoC (`3_6C-80PER_3_6C`).

The dataset is divided into three "batches" of 46, 48 and 46 batteries each. In this work, only the first two batches are used, because they include tests showing the main peak of the IC curves. So, the analysis focuses on 94 batteries, cycled under 63 different fast-charging policies, with first-step currents from 1C to 8C, and second-step currents from 3C to 6C. The batteries have a widely varying cycle life ranging from 148 to 1227 cycles.

Figure 3.9 shows an example of the charging and discharging cycles for battery 36, which has a `7C-30PER_3_6C` policy. Considering the string defining the policy, the cycle is characterised by a

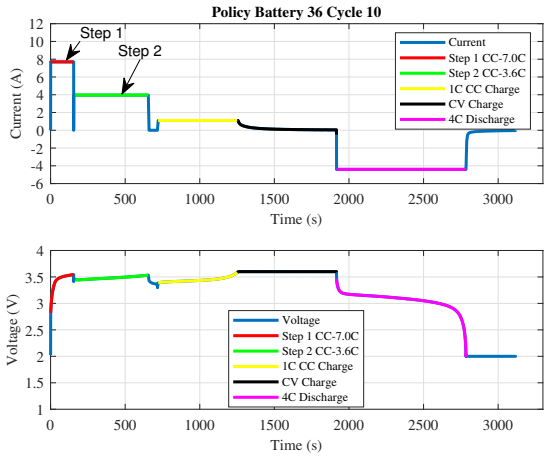

Figure 3.9: Two step charge and discharge policy of battery 36 cycle 10.

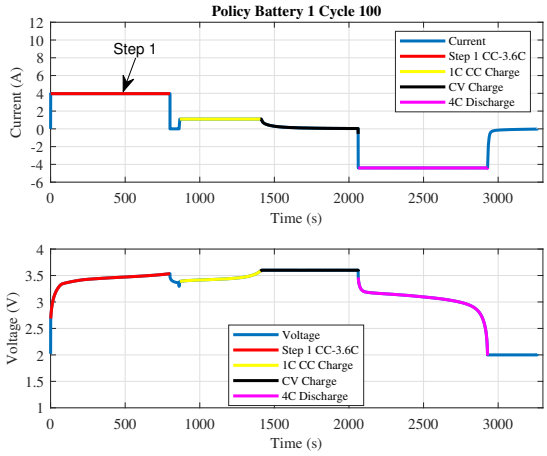

Figure 3.10: One step charge and discharge policy of battery 1 cycle 100.

first step current at 7C up to 30 % SoC and a second step current at 3.6C up to 80 % SoC.

In order to analyse the ageing trends in the dataset, it is worth to group batteries characterised by similar cycling conditions.

Therefore, the 94 batteries are divided into 15 groups with similar fast charging policies. The groups labelled 1, 2 and 3 have a one-step charging policy, whose current increases with the group id. The other groups have a two-step charging policy with a first-step current that grows with group id. Groups 1, 8, 9, 11, 12 and 15 are characterised by equal values for both C_1 and C_2; for groups 7, 10, 13 and 14, C_1 is the same within each group, while C_2 varies. The remaining groups collect the remaining batteries (2-6). Table 3.8 collects all the information about the groups.

3.5.3.2 Incremental Capacity Features as Capacity Indicators Under Fast Charging

The procedure introduced in Section 3.2 was applied to the data available on the fast charging dataset. The filters parameters have been adjusted for the dataset. The window of the SG filter is set equal to 5 samples, the window for the GWMA filter is 35 mV, and $\Delta V = 25\,\text{mV}$. The value of ΔV was selected empirically, by aiming to maximise the correlation between PA and SoH while avoiding that the voltage range used for the area computation fell outside of the available voltage data points. Furthermore, it is worth highlighting that the use of a fixed ΔV during the whole battery first life aims to enable the PA computation even when the data for the whole peak is not available. A sample IC curve obtained for this set of batteries is presented in Figure 3.11 for battery 30, during its 10th cycle.

3.5.3.3 Ageing Models

The procedure described in the previous subsection is applied to all the cycles for all the batteries. Obviously, some cycles are affected by errors, like missing sections of time-domain data, and must not be processed for IC extraction to avoid unnecessary outlier points. After the removal of the irregular cycles, the discharge capacity Q of the battery, computed in the 4C-discharge phase, can be related, cycle by cycle for each battery, to the IC peak area PA. It is worth noting that the computation of Q through

Table 3.8: Division of batteries into groups with instructions on the charging policy.

Group	**Batteries**	**N.Step**	C_1	C_2	**Comments**
1	1,2,3,54,55,56	1	$3.6C$		same policy current for all batteries
2	4,5,6,62,63	1	$[4C, 4.4C]$		C_1 equal to 4C or 4.4C
3	7,8,21,22,71,72,73	1	$[4.8C, 5.4C]$		C_1 equal to 4.8C or 5.4C
4	47,48,49,50,51,52,53,57	2	$[1C, 3.6C]$	$[4.85C, 6C]$	C_1 and C_2 very variable
5	58,59,60,61,64,65,66,67	2	$[4C, 4.4C]$	$[4.85C, 6C]$	C_1 equal to 4C or 4.4C, C_2 very variable
6	68,69,70,74,75,76	2	$[4.64C, 4.9C]$	$[4.25C, 6C]$	C_1 and C_2 very variable
7	77,78,79,80,81,82	2	$5.2C$	$[3C, 4.75C]$	same C_1, C_2 variable
8	11,12,15,16,19,20	2	$5.4C$	$3C$	same policy currents for all batteries
9	9,10,13,14,17,18	2	$5.4C$	$3.6C$	same policy currents for all batteries
10	83,84,85,86,87,88	2	$5.6C$	$[3C, 4.75C]$	same C_1, C_2 variable
11	25,26,29,30,33,34,94	2	$6C$	$3C$	same policy currents for all batteries
12	23,24,27,28,31,32	2	$6C$	$3.6C$	same policy currents for all batteries
13	89,90,91,92,93	2	$6C$	$[3.5C, 4.75C]$	same C_1, C_2 variable
14	35,36,37,38,39,40	2	$7C$	$[3C, 3.6C]$	same C_1, C_2 equals 3C or 3.6C
15	41,42,43,44,45,46	2	$8C$	$3.6C$	same policy currents for all batteries

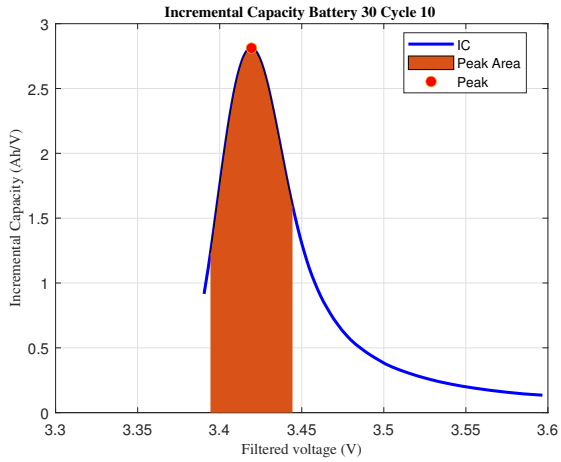

Figure 3.11: IC curve and peak features for battery 30, cycle 10.

a 4C CC discharge current, which is the only one available in all tests, leads to lower capacity values that those expected using typical characterisation currents, such as 1C or C/20. Nevertheless, despite the underestimation, it is expected that the conclusions obtained for this scenario, regarding the PA-Q relation, hold for typical characterisation cases.

The ageing trend of the function $Q = Q(\mathrm{PA})$ is analysed by using four different models. The first model links PA and Q in a *linear* way:

$$Q = a\mathrm{PA} + b, \tag{3.3}$$

where a and b are the fitting coefficients, representing respectively the slope and intercept of the line. The second is a second degree *polynomial* function:

$$Q = a\mathrm{PA}^2 + b\mathrm{PA} + c, \tag{3.4}$$

where a, b and c are the fitting coefficients. The third model is a *power law* model:

$$Q = a\mathrm{PA}^b + c, \tag{3.5}$$

with fitting coefficients a, b, and c. The shape of the ageing curve

suggests to consider also the *logarithmic* model:

$$Q = a + b \log \mathrm{PA}. \tag{3.6}$$

The model is again characterised by two fitting coefficients a and b.

Figure 3.12 shows an example of the performance of the four fitting models for battery 36. In this case, as well as in the large majority of the others, the linear model has the worst fitting performance.

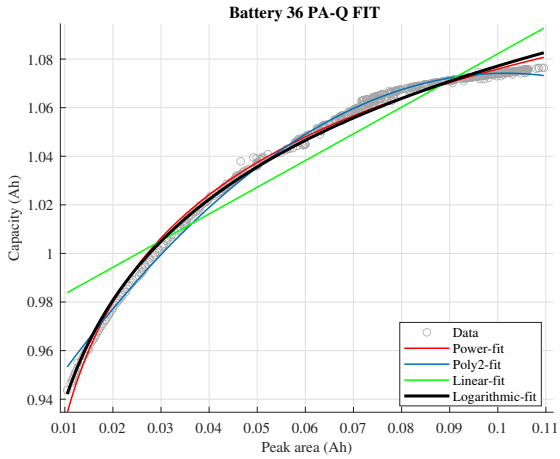

Figure 3.12: Example of linear, 2nd order polynomial, power law and logarithmic (solid line) fitting of battery no. 36 data (markers).

Fitting coefficients are computed for each battery in Matlab®, by using the built-in function `fit`. The function gives as output the fitting coefficients of the models, the square of the correlation coefficient R^2, and the Root Mean Squared Error (RMSE). In order to show the results of the fit for all models and compare them, aggregated indicators for the fitted parameters were computed, for the R^2 and RMSE: the mean over all batteries, and the standard deviation, reported in Table 3.9.

The *linear* models performance is the worst one, showing the lowest values of average R^2, which does not reach 0.9, and the highest values of average RMSE (around 12 mA h).

Table 3.9: Average values and standard deviation of the parameters of the linear, polynomial, power and logarithmic models of all 94 batteries.

Parameter	Mean	Standard deviation
Linear model		
a	1.384	24.1 %
b	0.958	2.4 %
R^2	0.889	8.2 %
RMSE (mA h)	11.896	46.3 %
Polynomial model		
a	-17.217	−48.8 %
b	3.193	25.8 %
c	0.921	2.4 %
R^2	0.98	2.2 %
RMSE (mA h)	4.442	65.1 %
Power law model		
a	0.185	1488.2 %
b	0.088	438.5 %
c	1.192	218.2 %
R^2	0.99	1.7 %
RMSE (mA h)	2.879	52.2 %
Logarithmic model		
a	1.218	2.4 %
b	0.06	17.9 %
R^2	0.976	4.3 %
RMSE (mA h)	4.573	47.8 %

The average R^2 is satisfactorily high for the *polynomial* (0.98), the *power law* (0.99) and *logarithmic* models (0.98). The *power law* model is also characterised by very low RMSE (less than 3 mA h). Unfortunately, its coefficients deeply vary among batteries, as

shown by the highest values of standard deviation for the fitting coefficients (overtaking 200 %). Such values indicate that the parameter values are strongly dispersed, and this model has poor generalisation capabilities. Conversely, the *logarithmic* model has acceptable values for R^2 and RMSE, and, in addition, the values of the standard deviations for a and b are relatively low. This result suggests to use the *logarithmic* model to represent the link Q-PA under the considered fast charging scenario.

3.5.3.4 Numerical Results

In order to analyse in detail the performance of the model for the representation of aggregated sets of data, the data from each battery group listed in Table 3.8 is fitted. Table 3.10 shows the results of the logarithmic fit for each battery group, and Table 3.11 reports on the average results, which are similar to the aggregated results reported above. Figure 3.13 shows the plots of Q as a function of PA for six battery groups (4, 5, 6, 7, 15, 1). For the sake of compactness, the plots related to the remaining groups are not included, being them very similar to what is already shown in the figure.

In Figure 3.13, it can be observed that he logarithmic model well approximates experimental data for groups 4-7. Similar results are achieved for groups 8-9, although they are not shown. In particular, for groups 4-5, which have two-step policies and $C_1 < 4.5C$, the model is better at approximating the data points at the top of the curve (initial cycles) and at the bottom (final cycles), while a larger deviation affects the central part of the fit. A larger deviation for 6 and 7 at the top of the curve is observed. The value of the fast charge current C_1 is never above 5.5C for groups 4-9. Group 15 collects batteries characterised by the highest value of C_1 (8C). The output data is less homogeneous. Similar results are observed for high C_1 battery groups 10-14. Such results suggest that the use of higher fast-charging currents, over 6C, leads to higher variations in the IC curves among batteries. Group 1 is characterised by a single fast charging step. In this case, the ageing trend is more

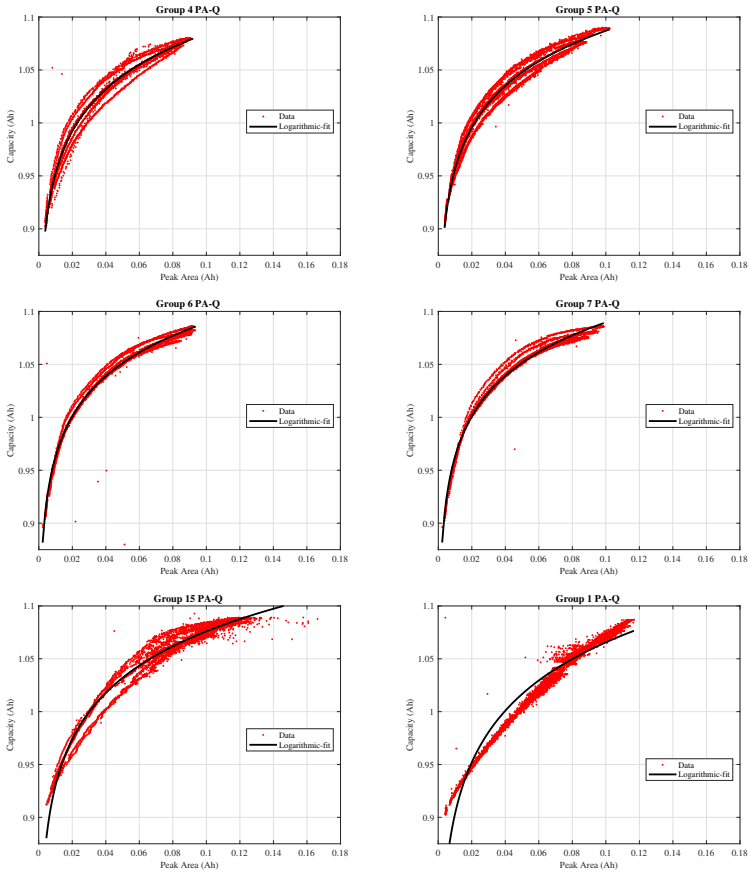

Figure 3.13: Capacity Q as a function of peak area PA in various battery groups. Experimental results (markers); logarithmic fit (solid line).

linear, and the results of the logarithmic model are less satisfactory, as clearly shown by the figure as well as by the largest RMSE and lowest R^2 among groups. The same results hold for group 2 and group 3.

Table 3.10: Values of a, b, R^2, and RMSE of the logarithmic model; calculated for the 15 groups.

Group	a	b	R^2	**RMSE** (mA h)
1	1.2282	0.0706	0.9418	10.7255
2	1.229	0.0688	0.9464	10.0125
3	1.2449	0.0708	0.9491	9.9996
4	1.2161	0.0572	0.9715	7.849
5	1.2176	0.0567	0.9787	6.4867
6	1.2157	0.0549	0.9747	6.6205
7	1.2163	0.055	0.9829	5.2962
8	1.2197	0.064	0.9626	7.2232
9	1.2362	0.0687	0.9742	6.267
10	1.2144	0.0534	0.956	8.7128
11	1.2211	0.0631	0.9804	5.8037
12	1.2362	0.0684	0.9818	5.1812
13	1.212	0.0525	0.9616	7.93
14	1.2221	0.0622	0.9854	4.0221
15	1.2221	0.0635	0.9633	7.7653

Table 3.11: Mean value and standard deviation of parameters a, b, R^2, and RMSE calculated by groups.

Parameter	**Mean**	**Standard deviation**
a	1.223	0.8 %
b	0.062	10.6 %
R^2	0.967	1.5 %
RMSE (mA h)	7.33	26.5 %

3.5.4 Towards an On-Board Implementation

In the perspective of a real-life application, where the signals are acquired on-board, the data quality could be worse than the one obtained in a laboratory environment, due to the lower performance of the voltage and current sensors and the lower resolution of the analog-to-digital converters. The signals may be affected by higher noise levels and discretisation errors, adding further challenges to the operation. As far as voltage signals are concerned, the SG filter should address this issue, by properly selecting the filtering window, in the stream of what has been done for the Oxford dataset analysis in Section 3.5.1.

In combination with the two proposed filtering stages, an accurate selection of a battery monitoring chip, which are typically marketed with voltage resolutions in the order of 1 mV using representations of around 16 bit, will help to mitigate the impact of the reduced quality of the available voltage signal (see, for instance, the ST Microelectronics chip L9963E, [127]).

In the case of current measurement, as the proposed HCIC technique works during the CC charge stage, the accuracy of the Coulomb counting performed for the capacity computation will fully depend on the accuracy of the acquisition hardware, including analog-to-digital converter resolution and the quality of the employed shunt resistors. If the measurement of the constant current is affected by high noise levels, the addition of a moving average filter for the current signal may be considered. Furthermore, in order to increase the reliability of the capacity estimation, the Coulomb counting modules included in high-end battery monitoring devices may be employed. If the method runs on the same device performing a SoC estimation based on feedback voltage signals, it is possible to take advantage of this feedback to reduce or virtually cancel the Coulomb counting errors.

3.6 Conclusions

In this chapter, the IC analysis at 1C current was successfully used for a set of batteries aged using a cycling regime of random nature. The batteries are charged and discharged with randomly selected current levels and pulse durations in various operating conditions and load/charge profiles. Such current levels are referred to as high currents, because they are significantly higher than the ones used in typical IC analyses, in which the batteries are in pseudo-equilibrium condition.

An analysis of the correlation between three peak features extracted from the high current IC curves and the battery full capacity, proves that the most robust capacity indicator is the area under the main peak of the high current IC curve, called PA and computed in a voltage range of 100 mV centred on the IC curve main peak.

The computational aspects related to the extraction of the high-current IC peak features were also reported, with particular attention to the two filtering stages needed in the extraction of the peak features from the rough voltage and current measurements, for which a second-order Savitsky-Golay and a Gaussian Weighted Moving Average filters were adopted.

The computation of the capacity indicator PA was optimised, in the sense that the best integration interval for its computation was found. The PA outperforms other indicators based on the area evaluated under off-peak voltage intervals, and the PA is insensitive to the window of the Gaussian weighted moving average filter used to smooth the IC curve.

The PA is shown to be linearly related to the battery full capacity in the range of the battery first life, that is from 100 % down to 80 % of the battery initial capacity. The square of the correlation coefficient achieved from the fits goes over 0.95 for the large majority of batteries. For batteries belonging to the same group, that is, tested according to similar load and charge profiles, the dispersion of the linear fits is rather low for most of the battery groups, with a standard deviation of the slopes that, in several cases,

goes below 6 %, enabling the generalisation of the relationship from the battery level to the group level, with a single linear equation. A further grouping of battery groups from 4 to 7 could be considered, as the overall standard deviation of the slopes was found to be 5.01 %. This enables the use of the high-current IC PA feature as a general capacity indicator for batteries operating in a well-defined family of operating conditions including random charge profiles. A further proof of the applicability of the high-current IC peak features as capacity indicators was presented by applying the method to another set of batteries, cycled using typical driving profiles. The relationships between PA and the battery SoH is again linear, with a lower scattering among batteries that in the previous case, due to the usage of the same cycling policy for all the cells in the dataset and for the absence of any randomisation of the charging/discharging profile. Then, the method is compared with a ohmic resistance-based SoH assessment approach, showing its advantages in terms of higher generalisation potential.

The IC analysis of the Toyota dataset shows that the peak area PA of the IC curve is a very good indicator to estimate the 4C discharge capacity for batteries cycled with multistep fast charging profiles ending with a 1C CC -CV charge, and, therefore, a good SoH indicator for Lithium-Iron-Phosphate batteries. The non linearity in the PA-Q relationship may be ascribed to the presence of high-current charging steps beyond $5.5C$.

The 1C constant current charging, on which the IC curve was computed in this chapter, is compatible with some charge phases of a battery in an integrated energy system, such as a smart grid or in an EV in a long rest. Moreover, the computational burden required by the procedure is suitable for implementation on low-cost devices, which could be easily embedded in the battery charger or in the BMS. In the perspective of an application in an energy system, where the knowledge of the battery SoH is of paramount importance for an accurate energy management and for the planning of the battery replacement, this will enable the on-board battery health estimation based on the proposed feature, performed any time the IC requirements are met during charge.

Chapter 4

Battery State-of-Health Estimation Based on Multiple Charge and Discharge Features

Features coming from different usage stages are used together in multifeature approaches [84, 85]. Despite their good accuracy, the on-board application of multifeature approaches is very limited at present. An analysis of recent literature on multifeature approaches, reported on Section 1.3.2.2, highlights the following three major limiting factors.

1. Typically, the features used in literature can rarely be extracted during the normal usage of a battery. For instance, the time duration of CC and constant-voltage (CV) phases, or charged capacities in CC and CV.

2. The number of batteries used to train and test the models is very low. Indeed, most of the evaluation processes were performed using 1 to 4 batteries [128, 90].

3. Batteries undergo ageing by using uniform cycling profiles, with simple laboratory CC-CV charge-discharge cycles. Such

cycling profiles are very far from real battery usage profiles in stationary or EV applications.

In order to overcome the aforementioned limitations, a set of simple linear multifeature models are proposed for the capacity estimation and, therefore, for the SoH assessment. Those models are based on features that can easily be extracted during any battery partial charge or discharge. The first advantage of such approach with respect to literature approaches is that neither full charges nor full discharges are required to extract the features. Capacity indicators extracted from two different stages of battery usage data are considered. On th one hand, during partial charges at 1C, the HCIC features introduced in Chapter 3 are computed. On the other hand, during a CC discharge phase, starting from a fixed SoC condition, like full-charge state, dynamic resistances are computed [82, 129]. Employing such features, linear multifeature models are build, by starting with all the available features and applying several features selection methods based on statistical criteria. Then, an analysis of their SoH prediction performance is done in terms of MSE minimisation, while tracking their capability for reducing the multicollinearity among the features used in the model. The features selection aims to keep models easily interpretable and computationally affordable for implementation on embedded battery systems.

Additionally, two datasets are used, including a total of 36 Li-ion batteries, for the evaluation of the models. The batteries are cycled employing specific driving profiles or randomly-built CC profiles, and are grouped in such a way that the validation includes different degrees of cycling uniformity, in deep contrast to the high uniformity of the batteries employed in previous works.

4.1 Reference Datasets and Discharge Capacity Extraction

In order to extract full capacity indicators from partial charge/discharge data, two of the publicly available battery degradation datasets

employed in the previous chapter are considered. Namely, the NASA Random Walk and Oxford Battery Degradation datasets, introduced in Section 3.1 and Section 3.5.1 respectively. Both of them include characterisation stages, made of reference CC charge/discharge cycles, which periodically break battery random or automotive-like cycling.

4.1.1 Grouping

These sets of batteries can be grouped by considering different degrees of uniformity in terms of cycling profile. In the case of the batteries in the NASA dataset, a first subset with a *moderate level of uniformity* is constructed by considering the 16 batteries in the groups from 4 to 7. The batteries in those groups share cycling profile policy, with a fixed charge stage and random discharge. The groups among the subset differ from one another by operating temperature and by the parameters of the discharge current probability distribution, as indicated in Table 3.1.

A second subset with *low level of uniformity* is constructed by considering the whole NASA dataset. The batteries in groups from 1 to 3 have fully random charge and/or discharge profiles during cycling, an so, a much less uniform cycling than groups from 4 to 7, as pointed out in Table 3.1, leading to an overall less uniform subset.

Finally, one single group containing the 8 batteries in the Oxford dataset, which underwent the same cycling profile, constitutes a third subset with a *high level of uniformity*. These three battery subsets will be used throughout this study to evaluate the performance of the SoH models.

4.1.2 Computation of the Full Capacity as a Function of Ageing

The reference discharge cycles at 0.5C and 1C for the NASA and Oxford datasets respectively were used for the computation of Q. As both are CC discharges after a full charge and go down to a

fixed voltage limit, Q can be computed by integrating the current over time. The integral of the current signal was computed by employing a trapezoidal approximation. The process was repeated for all the available reference discharges for the 36 batteries.

Then, for each battery, the SoH was computed as introduced by (1.1). The SoH values, down to 80 % for all batteries, are used from now on as the output of the proposed linear models, selected over Q in order to enable the combination of the data from different batteries for both training and testing procedures. The number of SoH values changes among batteries, due to the differences on available characterisation experiments. Between 4 and 49 SoH values per battery are available, for a total of 499 total data points, after outliers removal based on a moving median approach. This number of available data points is clearly too low for an effective application of complex data-driven strategies to the battery capacity estimation problem.

4.2 Discharged Capacity Indicators

Figure 4.1 shows an example, taken from cycling data of battery RW25 from the NASA dataset, where a partial 1C CC-CV charge is highlighted in between two randomised discharge profiles. Such partial charges could easily be found in normal usage of battery in any application. Therefore, if capacity indicators are extracted on such a stage, the capacity estimation can be performed regularly in a real battery application.

4.2.1 Full-Charge Capacity as Discharged Capacity Indicator

For the LCO and NMC batteries considered in this study, during first life, the charge capacity starting from a full-discharge state is expected to be one of the most straightforward indicators of the capacity available in discharge mode. In order to show this, the charge capacity Q_c is computed during all reference charges in

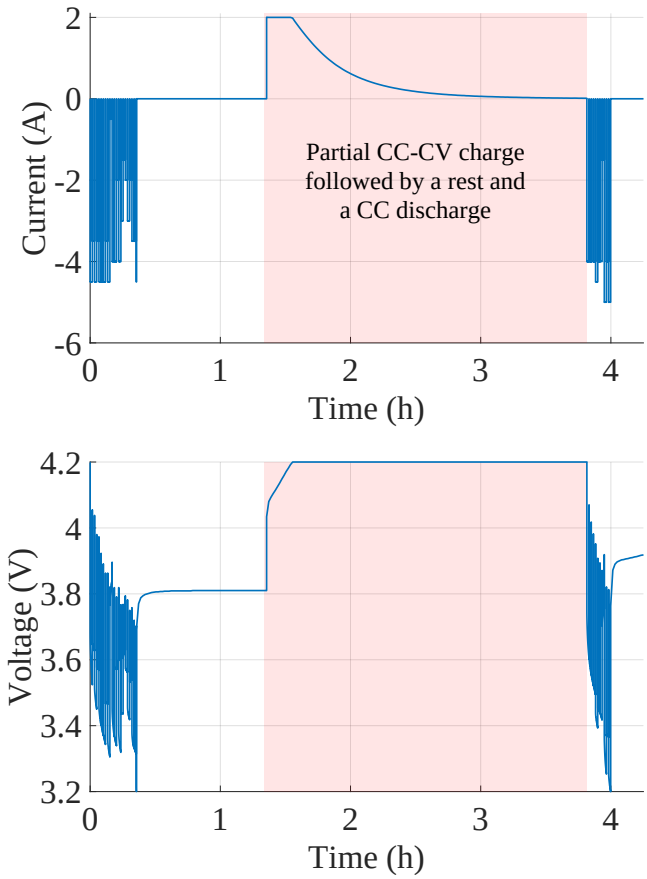

Figure 4.1: Example of a partial CC-CV charge during battery cycling taken from NASA dataset, battery RW25. The charge stage is highlighted. (a) current and (b) voltage as functions of time.

the NASA dataset. Such a charge stage starts from full-discharge state, which was previously detected by reaching the lower voltage threshold; then, a 1C CC charge is applied up to the upper voltage threshold; and, finally, the charge process ends with a CV charge down to C/200 current. The Q_c is normalised with respect to its value at the beginning of life (initial value).

Figure 4.2 shows how good is the correlation among Q_c and SoH for all the batteries in the NASA dataset. The points in the scatter plot are very close to the regression line in the full range of the battery first life (down to 80 %). The percentage error distribution in the inset shows that for over 60 % of the available Q values the approximation with Q_c presents errors under 1 %. Such results confirm that Q_c is a very good capacity indicator, and that it can be considered as an indirect measurement of Q.

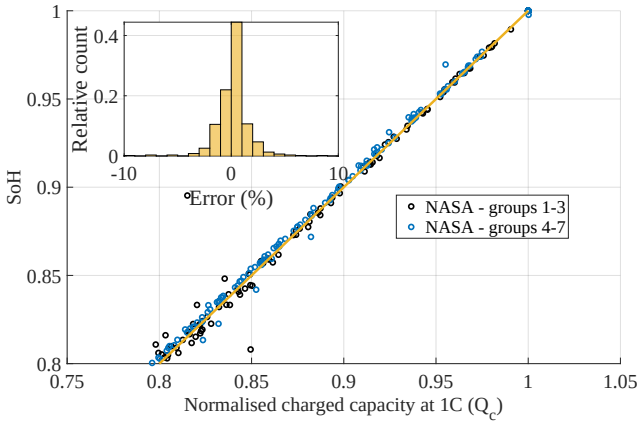

Figure 4.2: Normalised charged capacity as an indicator of the SoH for NASA dataset. The bar plot shows the percentage error distribution for Q_c with respect Q.

Unfortunately, a properly managed battery would rarely reach full discharge. Despite the strong correlation between Q_c and Q, this feature can rarely be computed during real use of a battery. Therefore, it is suggested to use it as a reference or calibration point, when its computation can be performed, rather than as a

SoH indicator.

4.2.2 Battery Capacity Indicators Based on Incremental Capacity

During battery common usage scenarios, the battery often undergoes partial charges, starting from an arbitrary SoC, like the one in Figure 4.1. For the computation of an IC curve, the data from a partial CC charge can be used, starting from an arbitrary SoC value up to the voltage threshold for CV charge. If the current levels approach 1C, then the IC data can be referred as the HCIC curve, computed as detailed in Chapter 3. The HCIC curve can be computed as:

$$\mathrm{IC}(n) = \frac{dq}{dv}(n) \cong \frac{q(n) - q(n-1)}{v(n) - v(n-1)}, \tag{4.1}$$

where n represents a discrete time step, v the battery voltage and q the A h charge (or, alternatively, partial capacity) and is computed by numerically integrating the battery current using a trapezoidal scheme.

Figure 4.3 illustrates that the HCIC curves are characterised by one or more peaks. The information associated to the main peak is typically summarised by three indicators: the peak position (PP), its height (PH), and the area in the neighbourhood of the main peak (A_0). Such indicators, when available, are characterised by a high correlations with Q and, in particular, A_0 has the highest correlation with Q, with reference to the datasets presented in Section 4.1 [16].

By definition, the area under a charge IC curve during a given voltage range is an approximation to the partial capacity charged during that voltage range. Partial capacities during fixed voltage intervals have been used as Q indicators before [88]. Then, in order to increase the number of available HCIC features, two additional areas before the main peak are also considered. The voltage ranges for the computation of such areas are defined using the same voltage variation ΔV value that the one used for A_0. The position

of the two areas is defined with respect the main peak position as illustrated in Figure 4.3, which presents a sample HCIC curve for battery 1 in the Oxford dataset. These additional areas are labelled as A_1 and A_2 for the closest and farthest from the main peak, respectively.

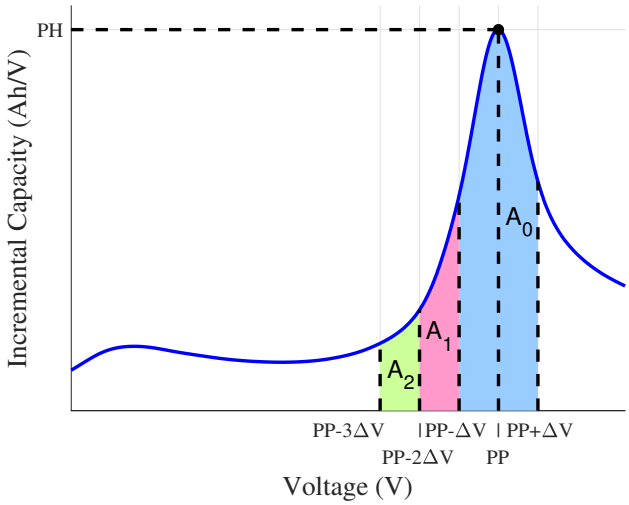

Figure 4.3: Example of an HCIC curve obtained for battery 1 in the Oxford dataset. The HCIC features PP, PH, A_0, A_1 and A_2 are highlighted.

Referring to the NASA and Oxford datasets, the scatter plots in Figure 4.4 show the correlation with SoH for the normalised PP and A_0, for capacity degradation within 20 %. A clear inverse relation between PP and SoH and a direct one when considering A_0 and SoH, for all the batteries in both datasets, can be observed. In both cases, a lower dispersion exists for the batteries in the Oxford dataset (red markers) with respect to those in the NASA dataset. Such a difference should be ascribed to the higher uniformity in the cycling profile for the batteries in the Oxford dataset. Additionally, it is worth highlighting the higher sensitivity to variations in SoH displayed by A_0 when compared to PP, making it more useful as a SoH indicator.

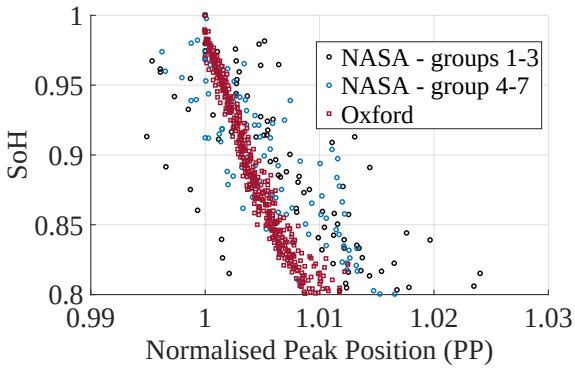

(a)

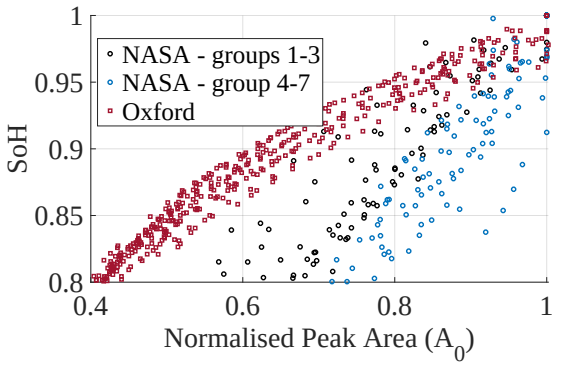

(b)

Figure 4.4: SoH as a function of the HCIC features (a) PP and (b) A_0.

4.2.3 Dynamic Resistance as a Battery Capacity Indicator

In many applications, after a charge phase ending with at a specific SoC value, the battery is often let at rest. Such scenario is, for example, very common for EVs charged at home overnight. This condition is very useful for measuring the dynamic resistance during the first discharge current step after the rest. The resistance $R_{\Delta t}$ can easily be computed within a certain time window Δt, as the ratio among the changes in voltage, ΔV, and the constant current I_d over a given time window:

$$R_{\Delta t} = \frac{\Delta V}{I_d}. \tag{4.2}$$

Such a ratio, having the physical dimensions of a resistance, can be used as a capacity indicator, as often done in literature [125].

The time windows Δt available for the resistance computation are restricted by the data sampling time T_s and the duration of the discharge current step. Although resistances obtained with short Δt values —in the order of milliseconds —are closer to the battery ohmic resistance, their high sensitivity to noise reduces their practical interest. In this work, resistances with higher Δt are evaluated as Q indicators, in order to reduce the effects of noise.

With reference to both NASA and Oxford datasets, the resistances R_s, R_{30} and R_{300} were computed in correspondence to T_s, 30 s, and 300 s, respectively, during CC discharge stages at 1C current. The scatter plots of Figure 4.5 summarise the results of the computations. This figure shows how well the three normalised resistances are linked to Q. For the 3 resistances, an inverse correlation with SoH is observed. This is expected, as the battery impedance at fixed operating conditions tends to increase with ageing [129]. The dispersion of the normalised resistance points among batteries is reduced with the increase in Δt, this is particularly evident for the batteries in the Oxford dataset, highlighting once again the effects of the uniformity in the cycling profiles used for ageing. Hereinafter, a total of 8 features are considered, 5 of

them related to HCIC, and 3 dynamic resistances: PP, PH, A_0, A_1, A_2, R_s, R_{30} and R_{300}.

4.2.4 Correlation Between Capacity Features

The capacity indicators introduced above were extracted only on two data segments, and obviously they are highly correlated among them. Such a correlation can highly reduce the quality of degradation models combining more than one of those features. Figure 4.6 shows the correlation matrices for the three batteries subsets introduced in Section 4.1. Almost all indicators show a high correlation with Q. In particular, PH, A_0 and R_{300} have correlation coefficients ρ with absolute values over 0.8 for the three subsets, when comparing them with Q, as expected. Two main differences between the batteries in the Oxford and NASA datasets appear: the higher correlations among the capacity features in the Oxford dataset, and the change from direct to inverse relationship with Q for A_1 and A_2. The first difference can be explained by the higher uniformity in the cycling profiles employed in the Oxford dataset. These higher correlations between features mean high redundancy in the information available for Q estimation. The change in sign for the ρ values associated to A_1 and A_2, may be related to the difference in battery chemistries included in each dataset, LCO for NASA and NMC for Oxford.

It is worth mentioning that additional features obtained during the CC and CV charge stages were also considered, but their inclusion in this paper would not bring any substantial improvement to the discussion, nor to the results discussed hereinafter.

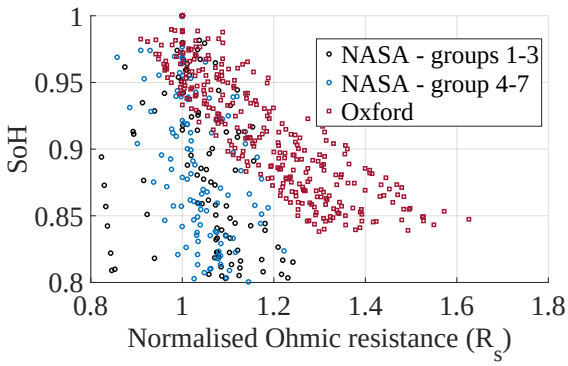

(a)

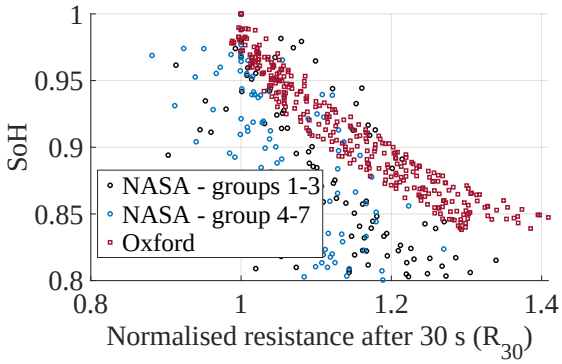

(b)

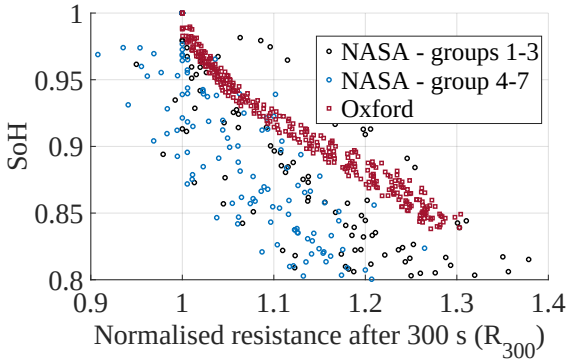

(c)

Figure 4.5: SoH as a function of the considered dynamic resistance features: (a) R_s, (b) R_{30} and (c) R_{300}.

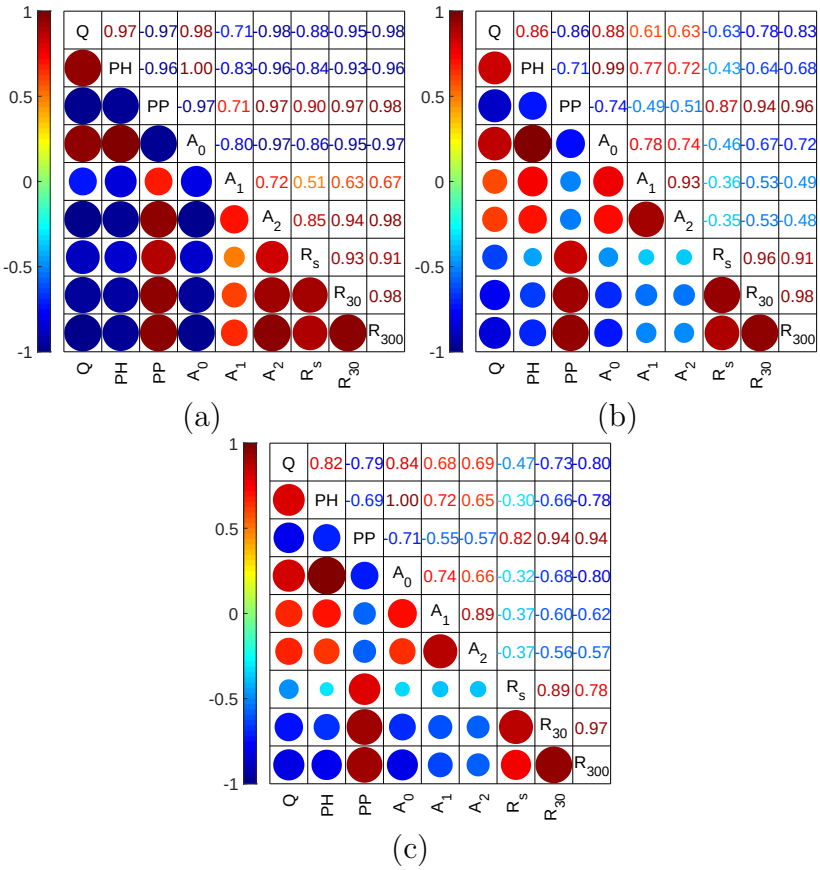

Figure 4.6: Correlation matrices between HCIC and dynamic resistance features for the three subsets: (a) Oxford, (b) NASA 4-7 and (c) full NASA. Red/blue colour stands for direct/inverse correlation; the largest the radius, the highest the correlation.

4.3 Modelling Capacity Degradation Through Partial Charge and Dynamic Resistance Features

Taking as input the subset of 8 features introduced in Section 4.2, and with reference to data related to first life of batteries, linear models were build up to estimate the actual discharge capacity Q of a battery as a function of features f_j, in the shape:

$$Q(f_1, \ldots, f_p) = \beta_0 + \sum_{j=1}^{p} \beta_j f_j, \tag{4.3}$$

where the coefficients β_j must be obtained by minimising the MSE between the model and the available values of Q in the training set.

4.3.1 Linear Models Based on Individual Indicators (Reference Models)

The most simple models, widely used in the literature, are single-feature models. In the following, the single-feature models of interest employ two specific features: the area under the main peak A_0 from the HCIC curve and one dynamic resistance feature, R_{300}. Inference results for individual batteries shown in [16] suggested A_0 as a robust capacity indicator, but its estimation performance, in the sense of prediction capability, needs to be addressed when considering a wide set of batteries. The indicator R_{300} is considered as a representative of the dynamic resistance class of indicators. This choice is motivated by a compromise between its acquisition time, which is compatible with real-world battery usage, and performance of the indicator for Q estimation. So, the linear models based on A_0 and R_{300}, from now on referred as PA and R models, respectively, will be considered as the reference ones for comparison with the multiple-feature models.

4.3.2 Linear Models With a Fixed Number of Features

The full model including all the 8 features, henceforth FL model, lies on the other side of the model complexity scale with respect to single-feature ones. The FL model is considered for the sake of completeness, despite the strong collinearity ($|\rho|$ close to 1) among features. In order to face the collinearity issue, which can compromise the quality of the estimation, and to reduce the computational complexity brought by managing a large number of features, models with intermediate complexity are considered. The first one is obtained by combining the two features considered as reference: A_0 and R_{300}, namely PA-R model.

4.3.3 Linear Model Fitted After a Statistical Features Selection Procedure

An alternative way to reduce the complexity of the models is to start from a given model, such as the FL or a constant value, and then select the features to keep or to add, and exclude the ones that poorly contribute to describe Q, according to a hypothesis test or a given statistical metric. In this work, the main feature selection goals are: first, to reduce the prediction errors with respect to the ones of the individual indicators; second, to reduce the collinearity among the included indicators. Even if both, multiple stepwise and regularisation-based methods were evaluated, only the two best performing approaches are reported, which are simply referred to as Backward stepwise selection (BW) and Belsley approaches (BEL), briefly summarised below. The first approach is a stepwise feature selection, which starts from the FL model and sequentially deletes the feature that has the smallest impact on a predefined statistical metric [130]. In this case, a feature is removed if the decrease in R^2 obtained by its removal is over a threshold. In this work, the threshold of R^2 decrease was fixed at 0.05. Features are removed one by one in an iterative procedure, which is stopped when all the R^2 variations obtained by removing any of the available features

are under the threshold.

The second method is based on the collinearity diagnostic procedure proposed by Belsley et al. in [131]. This diagnostic procedure assess the strength and sources of collinearity among variables in a multiple linear regression model. The diagnostic procedure aims to identify the near dependencies among the columns of the data matrix F defined as:

$$F = \begin{bmatrix} f_1^{(1)} & f_2^{(1)} & \cdots & f_8^{(1)} \\ f_1^{(2)} & f_2^{(2)} & \cdots & f_8^{(2)} \\ \vdots & \vdots & \ddots & \vdots \\ f_1^{(N)} & f_2^{(N)} & \cdots & f_8^{(N)} \end{bmatrix}, \tag{4.4}$$

where column j contains the N observations for the f_j feature. In this work, each column is scaled by its first value. The diagnostic is done by identifying the singular values of F with a high condition index. The number of conditions indexes deemed high, over 30 in this work, corresponds to the number of possible near dependencies among the features. Then, for each possible near dependency, the variance-decomposition proportions of all the features are checked: if two or more features have values over a threshold, 0.5 in this work, a near dependency among the involved features is confirmed.

The R^2 values between Q and each feature involved in the most severe near dependency (the one with the highest condition index) are evaluated, and the feature with the lowest value is removed from the model. This process is repeated in an iterative way until no more near dependencies among features are identified.

4.3.4 Framework for the Evaluation of Estimation Performance

For the evaluation procedure, each subset is divided into two parts. The first part, namely the training set, is used to estimate the β_j coefficients by applying the features selection procedure, when required, and ordinary least squares. The remaining data of the subset is used for the evaluation of the estimation performance

in terms of MSE. Additionally, in order to quantify the severity of the linear dependencies between the features in the resulting models, the variance inflation factor (VIF) is employed. The VIF associated to feature f_j, can be computed as:

$$\mathrm{VIF}_j = \frac{1}{1 - R_j^2}, \tag{4.5}$$

where R_j^2 is the coefficient of determination obtained for the linear regression of all the other features on f_j. In the next section, for each model, only the maximum VIF value for the features involved in the model is reported.

The data split is performed as follows.

Subset 1, NASA groups 4-7 Since each group is made of 4 batteries, a leave-one-out strategy is adopted, that is, only 1 battery per group is put in the test set, while the remaining 3 go in the training set. Ending up with 75 % of the batteries in the training set.

Subset 2, Full NASA dataset Same rule as Subset 1.

Subset 3, Oxford dataset To keep the same percentage of batteries in the training set, 6 batteries are used for training and 2 for the test set.

This data split aims to emulate a real fitting and estimation framework, on which models are trained on a given set of batteries, and the estimation is performed on new batteries, once deployed. For each subset (low, moderate, and high uniformity), the features selection and model fitting procedures were performed for *all* the possible battery data splits, thus leading to an exhaustive cross-validation analysis.

4.4 State-of-Health Estimation Results

Initially the evaluation procedure is applied to the batteries in the groups 4-7 of the NASA RW dataset, in order to compare the models performance in the presence of batteries cycled with a

moderated level of uniformity. Then, the analysis is extended to the whole NASA dataset, in order to check and compare the results to a subset with a lower uniformity level. Finally, the Oxford dataset is analysed, whose battery technology and cycling profile differ from the NASA ones but are highly uniform in terms of ageing, because the cycling profile is the same for all batteries.

4.4.1 Subset 1. NASA RW Groups 4-7. Moderate Uniformity Level

The performance of the models for all 256 training/test possible splits is analysed. For all the trained models, the VIF and the minimised number of features are recorded, and their averages μ_{VIF} and p_{av} are computed (when the number of features is fixed, p is reported instead of p_{av}). In order to evaluate the models performance, the MSEs achieved in each test are collected, their average μ_{MSE} and their standard deviation σ_{MSE} are computed. In order to quantify the improvement introduced by each model with respect to the reference ones, the indicator I_{PA} is computed as the relative improvement:

$$I_{\text{PA}} = \frac{\mu_{\text{MSE}}(x) - \mu_{\text{MSE}}(\text{PA})}{\mu_{\text{MSE}}(\text{PA})} \tag{4.6}$$

where $\mu_{\text{MSE}}(\text{PA})$ is the average MSE achieved by using the PA model, $\mu_{\text{MSE}}(x)$ is the average MSE achieved by the model x. Similarly, the indicator I_{R} is defined by a comparison with the model R.

Table 4.1 summarises the results achieved for subset 1. In terms of MSE, all multiple features models improve the average estimation capability by reducing the average MSE with respect to both single feature reference models. In this case the best single-feature model is PA, the one based on HCIC. The best performance is obtained by the Backward selection-based model BW, with more than 50 % improvement with respect to R and more than 35 % improvement with respect to PA. All the other models with an average of around 2 features (BEL and PA-R) showed similar performance, despite

Method	μ_{MSE} (10^{-4})	σ_{MSE} (10^{-4})	$\frac{\sigma_{\text{MSE}}}{\mu_{\text{MSE}}}$ (%)	p_{av}	μ_{VIF}	I_{PA} (%)	I_{R} (%)
PA	9.352	6.111	65.35	1	–	–	26.64
R	12.748	4.166	32.68	1	–	-36.31	–
PA-R	6.766	5.731	84.70	2	2.532	27.65	46.92
BW	5.992	4.984	83.17	1.992	2.645	35.92	52.99
BEL	7.412	5.534	74.66	1.996	2.685	20.75	41.86
FL	6.583	4.150	63.05	8.000	611.291	29.61	48.36

Table 4.1: Average results over 256 tests for subset 1. Light green highlights improvements with respect to reference models, while dark green highlights the best result.

not an optimal one, keeping the maximum VIF values under 5. Such a threshold is often considered the warning threshold for significant collinearity [132]. Even if the FL model presented a good average performance in terms of MSE, the high value of average maximum VIF indicates severe multicollinearity issues, which may become a problem when trying to generalise this result.

Figure 4.7 plots the MSE values for all the considered 256 battery splits. To improve the readability of the plot, the tests are sorted to obtain an increasing MSE for reference PA model. The higher performance of the multiple features models with respect to the reference ones is confirmed by the plot, as lower MSE values are observed for the multiple regression models in the majority of the data splits. Figure 4.7 clearly shows that the MSE values step up around the 190th test. A check of the data splits revealed that battery RW25 was always used for training before this step, and for testing after it. With this analysis it can stated that battery RW25 should be considered as a peculiar statistical unit, and even if the correlation among the features and Q is still high, the data points are the ones farthest from the average tendency. Its exclusion from the dataset improves all results on average, as shown in Table 4.2. In this case, the overall best result in terms of average MSE is achieved by the PA-R model. This model reaches a reasonable compromise between features reduction (fixed at 2), low maximum VIF below the warning threshold, and "augmented" information.

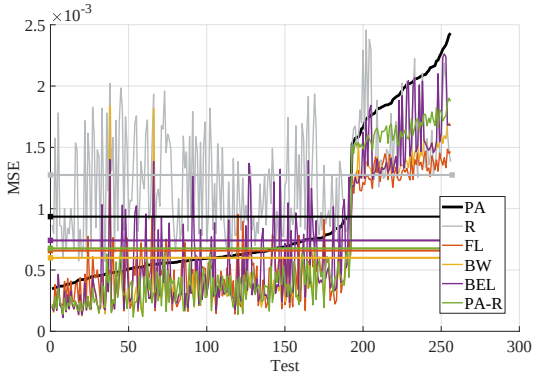

Figure 4.7: Summary of MSE results on the groups 4-7 from the NASA dataset for all the possible splits of batteries.

Method	μ_{MSE} (10^{-4})	σ_{MSE} (10^{-4})	$\frac{\sigma_{\text{MSE}}}{\mu_{\text{MSE}}}$ (%)	p_{av}	μ_{VIF}	I_{PA} (%)	I_{R} (%)
PA	5.849	1.650	28.21	1	–	–	48.92
R	11.451	3.632	31.72	1	–	-95.77	–
PA-R	3.112	1.473	47.33	2	2.536	46.79	72.82
BW	3.663	1.945	53.10	1.969	2.546	37.37	68.01
BEL	4.027	2.238	55.58	1.964	2.700	31.15	64.83
FL	4.380	1.933	44.13	8	472.398	25.11	61.75

Table 4.2: Average results over 192 tests for subset 1 with RW25 removed. Colours: see Table 4.1.

In order to illustrate how these average results translate into individual SoH estimation cases, an specific example is presented. Figure 4.8 depicts the estimation of SoH on some batteries belonging to the test set, where all models have been fitted using data from the remaining ones. The figure shows how multifeature approaches improve the estimation with respect to both single-feature models, depicted with hidden grey lines as a reference. Evident errors affecting single-feature models, like those ones for RW19 and 28, are compensated by all the multifeature approaches, improving the reliability of the estimation. BW and PA-R models, that is two-variables models, outperform FL, being closer to the experimental curve (for instance, see the results for RW19). This result could be ascribed to the strong maximum VIF characterising the FL model. It is worth remarking that the BEL model, which results are similar to the BW ones, has not been plotted for the sake of figure readability.

4.4.2 Subset 2. Full NASA RW Dataset. Low Uniformity Level

In order to test the SoH estimation capabilities of the multifeature models in the least uniform subset of batteries in terms of cycling profiles, the NASA RW dataset is analysed as a whole. Here, the effects of multicollinearity are expected to be mitigated by the lower uniformity of the battery set.

Method	μ_{MSE} (10^{-4})	σ_{MSE} (10^{-4})	$\frac{\sigma_{\text{MSE}}}{\mu_{\text{MSE}}}$ (%)	p_{av}	μ_{VIF}	I_{PA} (%)	I_{R} (%)
PA	11.775	4.225	35.879	1	–	–	13.671
R	13.639	4.089	29.979	1	–	-15.836	–
PA-R	9.986	4.542	45.480	2	4.327	15.19	26.79
BW	12.089	5.665	46.858	2.229	15.979	-2.669	11.37
BEL	11.667	5.401	46.294	2.173	3.134	0.92	14.46
FL	9.181	3.553	38.695	8	739.064	22.02	32.68

Table 4.3: Average results over 16384 tests for subset 2. Colours: see Table 4.1

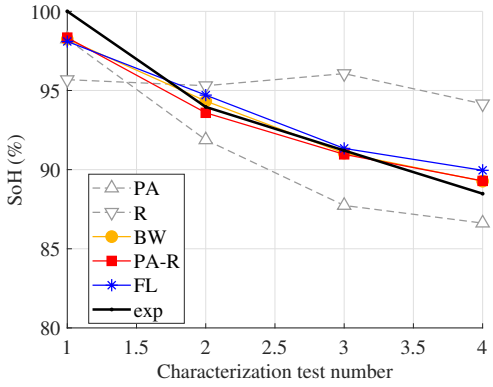

battery RW19

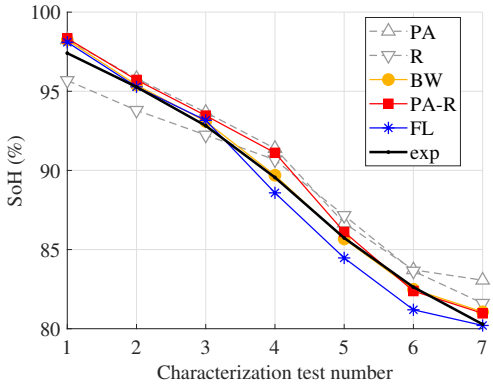

battery RW21

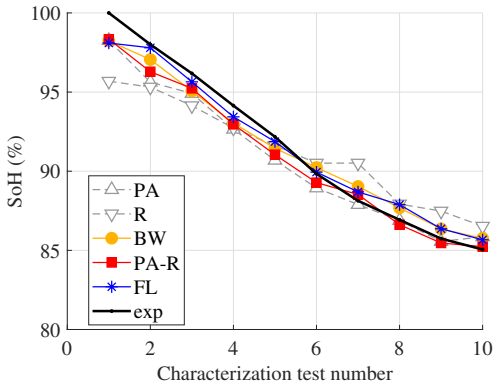

battery RW28

Figure 4.8: Example of SoH estimation for a particular training-test batteries split. Test set: {RW14, RW19, RW21, RW28}

Table 4.3 summarises the average results. The averaged results show that the model with the highest improvement in terms of MSE with respect the reference models is the FL one, despite high values of maximum VIF, which highlight collinearity issues. The statistical features selection does not help in this case, indeed the BW approach no longer improves with respect to the PA model. The best two-features model keeps being PA-R, always mixing information from partial charge and dynamic resistances.

4.4.3 Subset 3. Oxford Dataset. High Uniformity Level in the Presence of Cycling Through a Fixed Driving Profile

A different cycling profile, and highly uniform tests, may impact the performance of the models. In order to test this, the Oxford dataset is analysed, where all 8 batteries were cycled using the same regularly-repeated driving profile discharge and a fixed charge policy. Significant collinearity issues are expected, which should yield poor performance for the FL model in particular.

Table 4.4 summarises the average results obtained in the 28 tests. In this scenario, the FL model does not outperform the R approach, which seems very good in this case. Indeed, similar bad results are achieved by methods with reduced number of features, because the statistical selection procedure does not help to reduce the maximum VIF below the severe collinearity threshold, that is equal to 10 [132]. An acceptable compromise is represented by the PA-R model, which is a minimal-order, low-VIF multifeature approach by nature. It outperforms both reference indicators. In this particular case, a single indicator obtained during common usage training may be enough for an accurate SoH estimation. However, such scenario is rarely met in practice.

Nevertheless, it is worth highlighting that the PA-R model is the only one whose average MSE reduces with respect both PA and R reference models, for all datasets.

In general, under the studied prediction framework, which deeply differs from inference, features selection procedures do not

Method	μ_{MSE} (10^{-4})	σ_{MSE} (10^{-4})	$\frac{\sigma_{\text{MSE}}}{\mu_{\text{MSE}}}$ (%)	p_{av}	μ_{VIF}	I_{PA} (%)	I_{R} (%)
PA	1.118	0.757	67.710	1	–	–	-32.622
R	0.843	0.288	34.164	1	–	24.597	–
PA-R	0.747	0.477	63.855	2	19.975	33.184	11.388
BW	1.0461	0.483	46.171	1	–	6.431	-24.093
BEL	0.971	0.547	56.334	3.82	131.204	13.148	-15.184
FL	1.029	0.628	61.030	8	2721.2	7.961	-22.064

Table 4.4: Mean results over 28 tests for subset 3. Colours: see Table 4.1

bring any substantial advantage. On average, the most reliable choice is to combine two strong indicators, such as the peak area A_0 and the dynamic resistance R_{300}, in the PA-R model to obtain best results.

4.5 Conclusions

This chapter presented the performance evaluation for battery SoH estimation of linear models based on multiple capacity indicators, suitable for on-board implementation in battery systems. The charge-capacity, associated to a complete constant current charge from empty state, was identified as a strong indicator in terms of SoH prediction capability. However, the requirement of a full charge process is clearly unpractical. Then, the multifeature models, based on 8 indicators coming from high current IC and dynamic resistances data, were fitted and tested using a wide set of data collected on 36 batteries from two different publicly available battery degradation datasets.

A single-feature model can be enough for capacity estimation in very homogeneous cycling conditions. In this case, batteries in the test set behave similarly to the batteries in the training set. For this scenario, adding new features may degrade the estimation performance due to the collinearity among features. On such case, the models using the 8 features (FL) and features selection failed

to outperform the single-feature models. In order to improve the estimation in very homogeneous cycling conditions, a model named PA-R is proposed by combining the best performing features: the main peak area A_0 from IC analysis, and the dynamic resistance R_{300}. With this model, looking at the mean squared errors, an improvement of the estimation was achieved, namely 33.184 % and 11.388 % with respect the single feature models using only A_0 (PA) or R_{300} (R), respectively, despite moderate collinearity issues.

Linear multifeature models improve the SoH estimation in the presence of random cycling and moderate variations in temperatures and current levels. Two-features models introduced a major reduction on the MSE of the SoH estimation (over 30 % and 60 % with respect the PA and R models respectively), keeping low collinearity among the employed features, with average variance inflation factor (VIF) values under 2.7. Such a value is definitely below the so-called warning threshold. The FL model also improved the estimation over the reference models, but with high VIF values, over 400, which is beyond the limits for a reliable estimation.

Furthermore, even when considering a set of batteries with high heterogeneity in terms of cycling profiles, the PA-R model keeps improving the SoH estimation performance with low VIF values and improvements similar to the obtained by the FL model.

Collecting the results, the simple two-features model PA-R, combining A_0 and R_{300}, can be considered as the best linear multifeature model to improve the estimation of SoH. The choice is motivated by several factors: first, its capability to outperform single-feature models in any considered scenario; second, the wide validation set considered with respect to previous literature works; third, its inherent low maximum VIF; and last but not least, the reduced number of involved features to be used in computations, which is an additional benefit for on-board implementation in any batteries system.

Conclusion

This thesis aimed to address several methodological gaps identified for the implementation of State-of-Health (SoH) estimation on-board energy storage applications. The studies presented in this work focused on experiment and model based approaches. Three main research paths were considered: the proposal of methods for the implementation and identification of impedance fractional order (FO) models in on-board systems from frequency and time domain data, the proposal of 1C Incremental Capacity (IC) features as SoH indicators for batteries aged under randomised, driving profile and fast charging cycling and finally, the development of simple multifeature models reliant on features that can be extracted during the normal usage of the battery.

For the estimation of battery impedance parameters starting from Electrochemical Impedance Spectroscopy (EIS) data, a fitting procedure was presented. This procedure is based on the minimisation of the sum of the squares of the euclidean distances between experimental and approximated values for the impedance points at the frequencies of interest. A proper selection of the initial values of the model parameters, was identified as the most critical issue of the identification process. Hence, a procedure for an initial estimation of such values from the available EIS data was proposed. The method uses the values of the impedance at critical points, namely local maximum and minimum values, and employs the analytical equations for the real and imaginary parts of the battery impedance as functions of the frequency for establishing initial

approximations to the values of the resistances and constant phase elements in the model. When compared with fixed initial values, the proposed initialisation method guaranties the convergence of the identification algorithm.

Approximations with maximum relative distances to the experimental values under 2% were obtained, when the procedure with the proposed initial conditions was tested using experimental EIS results from the "Sandia Cell EIS Testing Data" repository.

Such method can be integrated to a characterisation process oriented to identifying the evolution of the impedance parameters over time. This would require a dataset including the ageing of multiple batteries under different conditions with periodic EIS characterisation tests, over which the identification of parameters using the proposed method could be applied and used for establishing relations with SoH and ageing mechanism. Furthermore, with current research trends aiming to implement EIS acquisition on-board, the availability of frequency domain data during rest periods of the battery may also enable the implementation of on-board SoH estimation and ageing diagnosis based on parameters fitted from EIS data.

When considering the issue of implementation of Fractional Order Models (FOMs) on-board, this work established that the selection of an implementation method can be addressed as follows: On the one hand, if the interest is only in the battery response simulation, the multiple RC (mRC) approach offers the best accuracy–complexity compromise, which is desirable for real-time simulations oriented towards the validation of energy management algorithms. On the other hand, if the application requires accurate identification of the impedance parameters from time-domain measurements, the Oustaloup (OU) approach offers the best compromise among identifying the impedance model parameters, the complexity and the accuracy requirements.

Subsequent efforts in this front should be aimed to the implementation of FOMs using the OU approach on embedded systems for the identification of impedance parameters using normal usage data of Li-ion batteries or for the online estimation of State-of-

Charge (SoC) and SoH when used in conjunction with Extended Kalman Filters or any other observer adapted to FOMs.

Aiming to identify SoH indicators that could be obtained during a Constant Current (CC) charge of a Li-ion battery, this work analysed the correlation between three peak features extracted from the high current IC curves and the battery full capacity, proving that the most robust capacity indicator is the area under the main peak of the high current IC curve, called PA and computed in a voltage range of 100 mV centred on the IC curve main peak.

The computational aspects related to the extraction of the high-current IC peak features were also reported, with particular attention to the two filtering stages needed in the extraction of the peak features from the rough voltage and current measurements, for which a second-order Savitsky-Golay and a Gaussian Weighted Moving Average filters were adopted.

The computation of the capacity indicator PA was optimised, in the sense that the best integration interval for its computation was found. It was also proven that the PA outperforms other indicators based on the area evaluated under off-peak voltage intervals, and that the PA is insensitive to the window of the Gaussian weighted moving average filter used to smooth the IC curve.

The PA is shown to be linearly related to the battery full capacity in the range of the battery first life, that is from 100 % down to 80 % of the battery initial capacity.

Further proofs of the applicability of the high-current IC peak features as capacity indicators were presented by applying the method to other sets of batteries, cycled using typical driving and fast charging profiles. In the first case the relationships between PA and the battery SoH was again linear, with a lower scattering among batteries that in the previous case, due to the usage of the same cycling policy for all the cells in the dataset and for the absence of any randomisation of the charging/discharging profile. Under a fast charging framework non-linear relationships were found on most cases, due to the higher charge currents employed before the 1C CC charge used for the IC analysis. Finally, the method was

compared with a ohmic resistance-based SoH assessment approach, showing its advantages in terms of higher generalisation potential.

Further evaluation of the applicability of this method needs to be performed. In particular the effects of the temperature during the CC charge and both the SoC and rest time before the interest CC charge need to be fully understood in order to make the SoH estimation obtained with 1C IC more robust. Such task will require of specific datasets with batteries cycled considering variations on the mentioned variables during charge.

The study of models employing multiple common usage features, allowed to identify a simple two-features model PA-R, combining the area under the main peak of a 1C IC curve, A_0, and a resistance computed after 300 seconds in discharge, R_{300}, as the best linear multifeature model to improve the estimation of SoH. The choice is motivated by several factors: first, its capability to outperform single-feature models in any considered scenario; second, the wide validation set considered with respect to previous literature works; third, its inherent low maximum VIF; and last but not least, the reduced number of involved features to be used in computations, which is an additional benefit for on-board implementation in any batteries system.

A next step for the development of multifeature models for SoH estimation should be oriented towards the identification and inclusion of new features coming from other sections of normal usage profiles of the batteries, this may include categorical features describing the distribution of critical variables during discharge of the battery, such as SoC, temperature and current. Another potential set of features may come from the parameters of impedance models identified on-board using the identification methods proposed in this work.

For both the IC and multifeature approaches validation steps with implementations on embedded systems need to be conducted during battery cycling experiments.

Bibliography

[1] V. Masson-Delmotte, P. Zhai, H.-O. Pörtner, D. Roberts, J. Skea, P. R. Shukla, A. Pirani, W. Moufouma-Okia, C. Péan, R. Pidcock, S. Connors, J. B. Robin Matthews, Y. Chen, X. Zhou, M. I. Gomis, E. Lonnoy, T. Maycock, M. Tignor, and T. Waterfield, "Global warming of 1.5°C," Intergovernmental Panel on Climate Change, Tech. Rep., 2018. [Online]. Available: https://www.ipcc.ch/site/assets/uploads/sites/2/2019/06/SR15_Full_Report_Low_Res.pdf

[2] G. Kamiya, S. Hassid, and P. Gonzalez, "Energy Storage - Tracking report November 2021," International Energy Agency, Paris, Tech. Rep., 2021. [Online]. Available: https://www.iea.org/reports/energy-storage

[3] G. L. Plett, *Battery Management Systems, Volume 1: Battery Modeling*, 1st ed. Artech House, 2015.

[4] L. Lu, X. Han, J. Li, J. Hua, and M. Ouyang, "A review on the key issues for lithium-ion battery management in electric vehicles," *Journal of Power Sources*, vol. 226, pp. 272–288, 2013. [Online]. Available: http://dx.doi.org/10.1016/j.jpowsour.2012.10.060

[5] S. M. Rezvanizaniani, Z. Liu, Y. Chen, and J. Lee, "Review and recent advances in battery health monitoring and prognostics technologies for electric vehicle (EV) safety and mobility," *Journal of Power Sources*, vol. 256, pp. 110–124, 2014. [Online]. Available: http://dx.doi.org/10.1016/j.jpowsour.2014.01.085

[6] R. Xiong, L. Li, and J. Tian, "Towards a smarter battery management system: A critical review on battery state of health

monitoring methods," *Journal of Power Sources*, vol. 405, pp. 18 – 29, 2018. [Online]. Available: http://www.sciencedirect.com/science/article/pii/S037877531831111X

[7] Z. Wang, S. Zeng, J. Guo, and T. Qin, "State of health estimation of lithium-ion batteries based on the constant voltage charging curve," *Energy*, vol. 167, pp. 661–669, 2019. [Online]. Available: https://www.sciencedirect.com/science/article/pii/S0360544218322126

[8] S. B. Sarmah, P. Kalita, A. Garg, X. D. Niu, X. W. Zhang, X. Peng, and D. Bhattacharjee, "A Review of State of Health Estimation of Energy Storage Systems: Challenges and Possible Solutions for Futuristic Applications of Li-Ion Battery Packs in Electric Vehicles," *Journal of Electrochemical Energy Conversion and Storage*, vol. 16, no. 4, 2019.

[9] A. Jossen, "Fundamentals of battery dynamics," *Journal of Power Sources*, vol. 154, no. 2, pp. 530–538, 2006.

[10] X. Lai, W. Yi, Y. Cui, C. Qin, X. Han, T. Sun, L. Zhou, and Y. Zheng, "Capacity estimation of lithium-ion cells by combining model-based and data-driven methods based on a sequential extended kalman filter," *Energy*, vol. 216, p. 119233, 2021. [Online]. Available: https://www.sciencedirect.com/science/article/pii/S0360544220323409

[11] Z. G. Wei, J. Hu, H. He, Y. Li, and B. Xiong, "Load current and state of charge co-estimation for current sensor-free lithium-ion battery," *IEEE Transactions on Power Electronics*, pp. 1–1, 2021.

[12] Z. Lyu, R. Gao, and L. Chen, "Li-Ion Battery State of Health Estimation and Remaining Useful Life Prediction through a Model-Data-Fusion Method," *IEEE Transactions on Power Electronics*, vol. 36, no. 6, pp. 6228–6240, 2021.

[13] V. M. Nagulapati, H. Lee, D. W. Jung, B. Brigljevic, Y. Choi, and H. Lim, "Capacity estimation of batteries: Influence of training dataset size and diversity on data driven prognostic models," *Reliability Engineering and System Safety*, vol. 216, no. June, p. 108048, 2021. [Online]. Available: https://doi.org/10.1016/j.ress.2021.108048

[14] Y. Choi, S. Ryu, K. Park, and H. Kim, "Machine Learning-Based Lithium-Ion Battery Capacity Estimation Exploiting Multi-Channel Charging Profiles," *IEEE Access*, vol. 7, pp. 75 143–75 152, 2019.

[15] S. Jenu, A. Hentunen, J. Haavisto, and M. Pihlatie, "State of health estimation of cycle aged large format lithium-ion cells based on partial charging," *Journal of Energy Storage*, vol. 46, no. August 2021, p. 103855, 2022. [Online]. Available: https://doi.org/10.1016/j.est.2021.103855

[16] B. O. Agudelo, W. Zamboni, and E. Monmasson, "Application domain extension of incremental capacity-based battery soh indicators," *Energy*, p. 121224, 2021. [Online]. Available: https://www.sciencedirect.com/science/article/pii/S0360544221014729

[17] N. Noura, L. Boulon, and S. Jemeï, "A review of battery state of health estimation methods: Hybrid electric vehicle challenges," pp. 1–20, 12 2020.

[18] S. Park, J. Ahn, T. Kang, S. Park, Y. Kim, I. Cho, and J. Kim, "Review of state-of-the-art battery state estimation technologies for battery management systems of stationary energy storage systems," *Journal of Power Electronics*, vol. 20, no. 6, pp. 1526–1540, 2020. [Online]. Available: https://doi.org/10.1007/s43236-020-00122-7

[19] D. Andre, M. Meiler, K. Steiner, C. Wimmer, T. Soczka-Guth, and D. U. Sauer, "Characterization of high-power lithium-ion batteries by electrochemical impedance spectroscopy. I. Experimental investigation," *Journal of Power Sources*, vol. 196, no. 12, pp. 5334–5341, 2011. [Online]. Available: https://doi.org/10.1016/j.jpowsour.2010.12.102

[20] A. Eddahech, O. Briat, E. Woirgard, and J. M. Vinassa, "Remaining useful life prediction of lithium batteries in calendar ageing for automotive applications," *Microelectronics Reliability*, vol. 52, no. 9-10, pp. 2438–2442, 2012. [Online]. Available: http://dx.doi.org/10.1016/j.microrel.2012.06.085

[21] A. Zenati, P. Desprez, H. Razik, A. Zenati, P. Desprez, H. Razik, and L. Ampere, "Estimation of the SOC and the SOH of Li-ion

Batteries , by combining Impedance Measurements with the Fuzzy Logic Inference," in *36th Annual Conference on IEEE Industrial Electronics Society IECON 2010*. Glendale, AZ, USA: IEEE, 2010.

[22] H. Wang, L. He, J. Sun, S. Liu, and F. Wu, "Study on correlation with SOH and EIS model of Li-ion battery," *Proceedings of the 6th International Forum on Strategic Technology, IFOST 2011*, vol. 1, no. 12511104, pp. 261–264, 2011.

[23] D. Andre, M. Meiler, K. Steiner, H. Walz, T. Soczka-Guth, and D. U. Sauer, "Characterization of high-power lithium-ion batteries by electrochemical impedance spectroscopy. II: Modelling," *Journal of Power Sources*, vol. 196, no. 12, pp. 5349–5356, 2011. [Online]. Available: http://dx.doi.org/10.1016/j.jpowsour.2010.07.071

[24] E. Barsoukov and J. R. Macdonald, *Impedance Spectroscopy Theory, Experiment, and Applications*, 2nd ed. Hoboken, New Jersey, USA: Wiley-Interscience, 2005.

[25] X. Li, Q. Wang, Y. Yang, and J. Kang, "Correlation between capacity loss and measurable parameters of lithium-ion batteries," *International Journal of Electrical Power and Energy Systems*, vol. 110, no. March, pp. 819–826, 2019. [Online]. Available: https://doi.org/10.1016/j.ijepes.2019.03.046

[26] L. Vichard, A. Ravey, P. Venet, F. Harel, S. Pelissier, and D. Hissel, "A method to estimate battery soh indicators based on vehicle operating data only," *Energy*, vol. 225, p. 120235, 2021. [Online]. Available: https://www.sciencedirect.com/science/article/pii/S0360544221004849

[27] M. Galeotti, L. Cinà, C. Giammanco, S. Cordiner, and A. Di Carlo, "Performance analysis and SOH (state of health) evaluation of lithium polymer batteries through electrochemical impedance spectroscopy," *Energy*, vol. 89, pp. 678–686, 2015.

[28] J. Li, K. Adewuyi, N. Lotfi, R. Landers, and J. Park, "A single particle model with chemical/mechanical degradation physics for lithium ion battery state of health (soh) estimation,"

Applied Energy, vol. 212, pp. 1178–1190, 2018. [Online]. Available: https://www.sciencedirect.com/science/article/pii/S0306261918300114

[29] R. Xiong, F. Sun, X. Gong, and C. Gao, "A data-driven based adaptive state of charge estimator of lithium-ion polymer battery used in electric vehicles," *Applied Energy*, vol. 113, pp. 1421–1433, 2014. [Online]. Available: http://dx.doi.org/10.1016/j.apenergy.2013.09.006

[30] A. Lievre, A. Sari, P. Venet, A. Hijazi, M. Ouattara-Brigaudet, and S. Pelissier, "Practical online estimation of lithium-ion battery apparent series resistance for mild hybrid vehicles," *IEEE Transactions on Vehicular Technology*, vol. 65, no. 6, pp. 4505–4511, 2016.

[31] X. Shu, G. Li, J. Shen, Z. Lei, Z. Chen, and Y. Liu, "A uniform estimation framework for state of health of lithium-ion batteries considering feature extraction and parameters optimization," *Energy*, vol. 204, p. 117957, 2020. [Online]. Available: https://www.sciencedirect.com/science/article/pii/S0360544220310641

[32] L. Yao, Z. Fang, Y. Xiao, J. Hou, and Z. Fu, "An intelligent fault diagnosis method for lithium battery systems based on grid search support vector machine," *Energy*, vol. 214, p. 118866, 2021. [Online]. Available: https://www.sciencedirect.com/science/article/pii/S0360544220319733

[33] D. Zhou, W. Zheng, S. Chen, P. Fu, H. Zhu, B. Song, X. Qu, and T. Wang, "Research on state of health prediction model for lithium batteries based on actual diverse data," *Energy*, vol. 230, p. 120851, 2021. [Online]. Available: https://www.sciencedirect.com/science/article/pii/S0360544221010999

[34] R. R. Richardson, C. R. Birkl, M. A. Osborne, and D. A. Howey, "Gaussian process regression for in situ capacity estimation of lithium-ion batteries," *IEEE Transactions on Industrial Informatics*, vol. 15, no. 1, pp. 127–138, 2019.

[35] A. Zenati, P. Desprez, and H. Razik, "Estimation of the SOC and the SOH of Li-ion batteries, by combining impedance meas-

urements with the fuzzy logic inference," *IECON Proceedings (Industrial Electronics Conference)*, pp. 1773–1778, 2010.

[36] Q.-K. Wang, Y.-J. He, J.-N. Shen, Z.-F. Ma, and G.-B. Zhong, "A unified modeling framework for lithium-ion batteries: An artificial neural network based thermal coupled equivalent circuit model approach," *Energy*, vol. 138, pp. 118–132, 2017. [Online]. Available: https://www.sciencedirect.com/science/article/pii/S0360544217312100

[37] K. A. Severson, P. M. Attia, N. Jin, N. Perkins, B. Jiang, Z. Yang, M. H. Chen, M. Aykol, P. K. Herring, D. Fraggedakis, M. Z. Bazant, S. J. Harris, W. C. Chueh, and R. D. Braatz, "Data-driven prediction of battery cycle life before capacity degradation," *Nature Energy*, vol. 4, no. 5, pp. 383–391, May 2019. [Online]. Available: https://doi.org/10.1038/s41560-019-0356-8

[38] Z. Fei, F. Yang, K.-L. Tsui, L. Li, and Z. Zhang, "Early prediction of battery lifetime via a machine learning based framework," *Energy*, vol. 225, p. 120205, 2021. [Online]. Available: https://www.sciencedirect.com/science/article/pii/S0360544221004540

[39] X. Zheng and X. Deng, "State-of-Health Prediction for Lithium-Ion Batteries with Multiple Gaussian Process Regression Model," *IEEE Access*, vol. 7, pp. 150 383–150 394, 2019.

[40] D. Liu, X. Yin, Y. Song, W. Liu, and Y. Peng, "An on-line state of health estimation of lithium-ion battery using unscented particle filter," *IEEE Access*, vol. 6, pp. 40 990–41 001, 2018.

[41] Z. Yun and W. Qin, "Remaining useful life estimation of lithium-ion batteries based on optimal time series health indicator," *IEEE Access*, vol. 8, pp. 55 447–55 461, 2020.

[42] B. Ospina Agudelo, A. Massi Pavan, W. Zamboni, R. Todd, A. Forsyth, E. Monmasson, and G. Spagnuolo, "Experimental analysis of capacity degradation in lithium-ion battery cells with different rest times," in *2020 2nd IEEE International Conference on Industrial Electronics for Sustainable Energy Systems (IESES)*, vol. 1, 2020, pp. 44–49.

[43] Y. Li, K. Liu, A. M. Foley, A. Zülke, M. Berecibar, E. Nanini-Maury, J. Van Mierlo, and H. E. Hoster, "Data-driven health estimation and lifetime prediction of lithium-ion batteries: A review," *Renewable and Sustainable Energy Reviews*, vol. 113, no. April, 2019.

[44] C. Pastor-Fernández, K. Uddin, G. H. Chouchelamane, W. D. Widanage, and J. Marco, "A comparison between electrochemical impedance spectroscopy and incremental capacity-differential voltage as li-ion diagnostic techniques to identify and quantify the effects of degradation modes within battery management systems," *Journal of Power Sources*, vol. 360, pp. 301 – 318, 2017. [Online]. Available: http://www.sciencedirect.com/science/article/pii/S0378775317303269

[45] Environmental Idaho National Engineering and Laboratory, "FreedomCAR Battery Test Manual For Power-Assist Hybrid Electric Vehicles," Tech. Rep., 2003. [Online]. Available: https://avt.inl.gov/sites/default/files/pdf/battery/freedomcar_manual_04_15_03.pdf

[46] L. Merkle, M. Pöthig, and F. Schmid, "Estimate e-golf battery state using diagnostic data and a digital twin," *Batteries*, vol. 7, pp. 1–22, 2021.

[47] M. Brand, D. Quinger, G. Walder, A. Jossen, and M. Lienkamp, "Evs26 international battery, hybrid and fuel cell electric vehicle symposium ageing inhomogeneity of long-term used bev-batteries and their reusability for 2 nd-life applications," 2012.

[48] K. Chen, S. Laghrouche, and A. Djerdir, "Prognosis of fuel cell degradation under different applications using wavelet analysis and nonlinear autoregressive exogenous neural network," *Renewable Energy*, vol. 179, pp. 802–814, 12 2021.

[49] Carlucci, "Battery state of health and state of charge estimation: comparison between classical and machine learning techniques," 2021.

[50] G. L. Plett, *Battery Management Systems, Volume 2: Equivalent-Circuit Methods*, 1st ed. Artech House, 2016.

[51] T. Bruen and J. Marco, "Modelling and experimental evaluation of parallel connected lithium ion cells for an electric vehicle battery system," *Journal of Power Sources*, vol. 310, pp. 91–101, 4 2016.

[52] E. Schaltz, D. I. Stroe, K. Norregaard, L. S. Ingvardsen, and A. Christensen, "Incremental capacity analysis applied on electric vehicles for battery state-of-health estimation," *IEEE Transactions on Industry Applications*, vol. 57, pp. 1810–1817, 3 2021.

[53] B. Ji, X. G. Song, W. P. Cao, and V. Pickert, "Active temperature control of li-ion batteries in electric vehicles," 2013.

[54] C. Weng, X. Feng, J. Sun, and H. Peng, "State-of-health monitoring of lithium-ion battery modules and packs via incremental capacity peak tracking," *Applied Energy*, vol. 180, pp. 360–368, 10 2016.

[55] C. Pastor-Fernández, "Phd thesis: Degradation diagnostics of lithium-ion batteries for automotive applications," 2019. [Online]. Available: http://wrap.warwick.ac.uk/134097

[56] L. Song, K. Zhang, T. Liang, X. Han, and Y. Zhang, "Intelligent state of health estimation for lithium-ion battery pack based on big data analysis," *Journal of Energy Storage*, vol. 32, 12 2020.

[57] H. Johnsson, "A neural network approach to absolute state-of-health estimation in electric vehicles battery degradation study based on fleet data," 2018.

[58] Q. Huo, Z. Ma, X. Zhao, T. Zhang, and Y. Zhang, "Bayesian network based state-of-health estimation for battery on electric vehicle application and its validation through real-world data," *IEEE Access*, vol. 9, pp. 11 328–11 341, 2021.

[59] J. I. Hidalgo-Reyes, J. F. Gómez-Aguilar, R. F. Escobar-Jiménez, V. M. Alvarado-Martínez, and M. G. López-López, "Classical and fractional-order modeling of equivalent electrical circuits for supercapacitors and batteries, energy management strategies for hybrid systems and methods for the state of charge estimation: A state of the art review," *Microelectronics Journal*, vol. 85, no. February, pp. 109–128, 2019. [Online]. Available: https://doi.org/10.1016/j.mejo.2019.02.006

[60] D. Qin, J. Li, T. Wang, and D. Zhang, "Modeling and Simulating a Battery for an Electric Vehicle Based on Modelica," *Automotive Innovation*, vol. 2, no. 3, pp. 169–177, 2019. [Online]. Available: https://doi.org/10.1007/s42154-019-00066-0

[61] Q. Ouyang, Z. Wang, K. Liu, G. Xu, and Y. Li, "Optimal charging control for lithium-ion battery packs: A distributed average tracking approach," *IEEE Transactions on Industrial Informatics*, vol. 16, no. 5, pp. 3430–3438, 2020.

[62] S. M. Alavi, C. R. Birkl, and D. A. Howey, "Time-domain fitting of battery electrochemical impedance models," *Journal of Power Sources*, vol. 288, pp. 345–352, 2015. [Online]. Available: http://dx.doi.org/10.1016/j.jpowsour.2015.04.099

[63] U. Krewer, F. Röder, E. Harinath, R. D. Braatz, B. Bedürftig, and R. Findeisen, "Review-Dynamic Models of Li-Ion Batteries for Diagnosis and Operation: A Review and Perspective," *Journal of The Electrochemical Society*, vol. 165, no. 16, pp. A3656–A3673, 2018.

[64] J. P. Tian, R. Xiong, W. X. Shen, and F. C. Sun, "Fractional order battery modelling methodologies for electric vehicle applications: Recent advances and perspectives," *Science China Technological Sciences*, vol. 63, no. 11, pp. 2211–2230, 2020.

[65] Y. Li, C. Zou, M. Berecibar, E. Nanini-Maury, J. C. Chan, P. van den Bossche, J. Van Mierlo, and N. Omar, "Random forest regression for online capacity estimation of lithium-ion batteries," *Applied Energy*, vol. 232, no. September, pp. 197–210, 2018.

[66] E. Riviere, A. Sari, P. Venet, F. Meniere, and Y. Bultel, "Innovative incremental capacity analysis implementation for c/lifepo 4 cell state-of-health estimation in electrical vehicles," *Batteries*, vol. 5, no. 2, 2019.

[67] Y. Li, M. Abdel-Monem, R. Gopalakrishnan, M. Berecibar, E. Nanini-Maury, N. Omar, P. van den Bossche, and J. Van Mierlo, "A quick on-line state of health estimation method for Li-ion battery with incremental capacity curves processed by

Gaussian filter," *Journal of Power Sources*, vol. 373, no. June 2017, pp. 40–53, 2018.

[68] Y. Jiang, J. Jiang, C. Zhang, W. Zhang, Y. Gao, and N. Li, "State of health estimation of second-life LiFePO4 batteries for energy storage applications," *Journal of Cleaner Production*, vol. 205, pp. 754–762, 2018.

[69] Y. C. Zhang, O. Briat, J. Y. Delétage, C. Martin, N. Chadourne, and J. M. Vinassa, "Efficient state of health estimation of Li-ion battery under several ageing types for aeronautic applications," *Microelectronics Reliability*, vol. 88-90, no. May, pp. 1231–1235, 2018. [Online]. Available: https://doi.org/10.1016/j.microrel.2018.07.038

[70] A. Fly and R. Chen, "Rate dependency of incremental capacity analysis (dQ/dV) as a diagnostic tool for lithium-ion batteries," *Journal of Energy Storage*, vol. 29, no. February, p. 101329, 2020. [Online]. Available: https://doi.org/10.1016/j.est.2020.101329

[71] E. Riviere, P. Venet, A. Sari, F. Meniere, and Y. Bultel, "LiFePO4 Battery State of Health Online Estimation Using Electric Vehicle Embedded Incremental Capacity Analysis," *2015 IEEE Vehicle Power and Propulsion Conference, VPPC 2015 - Proceedings*, 2015.

[72] I. Bloom, A. N. Jansen, D. P. Abraham, J. Knuth, S. A. Jones, V. S. Battaglia, and G. L. Henriksen, "Differential voltage analyses of high-power, lithium-ion cells 1. Technique and application," *Journal of Power Sources*, vol. 139, no. 1-2, pp. 295–303, 2005.

[73] M. Dubarry, C. Truchot, and B. Y. Liaw, "Synthesize battery degradation modes via a diagnostic and prognostic model," *Journal of Power Sources*, vol. 219, pp. 204–216, 2012. [Online]. Available: http://dx.doi.org/10.1016/j.jpowsour.2012.07.016

[74] M. Ouyang, Z. Chu, L. Lu, J. Li, X. Han, X. Feng, and G. Liu, "Low temperature aging mechanism identification and lithium deposition in a large format lithium iron phosphate battery for different charge profiles," *Journal of Power Sources*, vol. 286, pp. 309–320, 2015. [Online]. Available: http://dx.doi.org/10.1016/j.jpowsour.2015.03.178

[75] W. Wu, W. Wu, X. Qiu, and S. Wang, "Low-temperature reversible capacity loss and aging mechanism in lithium-ion batteries for different discharge profiles," *International Journal of Energy Research*, vol. 43, no. 1, pp. 243–253, 2019.

[76] X. Tang, C. Zou, K. Yao, G. Chen, B. Liu, Z. He, and F. Gao, "A fast estimation algorithm for lithium-ion battery state of health," *Journal of Power Sources*, vol. 396, no. April, pp. 453–458, 2018. [Online]. Available: https://doi.org/10.1016/j.jpowsour.2018.06.036

[77] J. Tang, Q. Liu, S. Liu, X. Xie, J. Zhou, and Z. Li, "A Health Monitoring Method Based on Multiple Indicators to Eliminate Influences of Estimation Dispersion for Lithium-Ion Batteries," *IEEE Access*, vol. 7, pp. 122 302–122 314, 2019.

[78] X. Li, C. Yuan, X. Li, and Z. Wang, "State of health estimation for Li-Ion battery using incremental capacity analysis and Gaussian process regression," *Energy*, vol. 190, p. 116467, 2020. [Online]. Available: https://doi.org/10.1016/j.energy.2019.116467

[79] X. Li, C. Yuan, and Z. Wang, "State of health estimation for li-ion battery via partial incremental capacity analysis based on support vector regression," *Energy*, vol. 203, p. 117852, 2020. [Online]. Available: https://www.sciencedirect.com/science/article/pii/S0360544220309592

[80] L. Zheng, J. Zhu, D. D.-C. Lu, G. Wang, and T. He, "Incremental capacity analysis and differential voltage analysis based state of charge and capacity estimation for lithium-ion batteries," *Energy*, vol. 150, pp. 759–769, 2018. [Online]. Available: https://www.sciencedirect.com/science/article/pii/S0360544218304213

[81] C. Lin, J. Xu, M. Shi, and X. Mei, "Constant current charging time based fast state-of-health estimation for lithium-ion batteries," *Energy*, vol. 247, p. 123556, 2022. [Online]. Available: https://doi.org/10.1016/j.energy.2022.123556

[82] X. Tan, Y. Tan, D. Zhan, Z. Yu, Y. Fan, J. Qiu, and J. Li, "Real-Time State-of-Health Estimation of Lithium-Ion Batteries Based on the Equivalent Internal Resistance," *IEEE Access*, vol. 8, pp. 56 811–56 822, 2020.

[83] Y. Zhang, Y. Liu, J. Wang, and T. Zhang, "State-of-health estimation for lithium-ion batteries by combining model-based incremental capacity analysis with support vector regression," *Energy*, vol. 239, p. 121986, 2022. [Online]. Available: https://doi.org/10.1016/j.energy.2021.121986

[84] Z. Lyu, G. Wang, and R. Gao, "Li-ion battery prognostic and health management through an indirect hybrid model," *Journal of Energy Storage*, vol. 42, no. June, p. 102990, 2021. [Online]. Available: https://doi.org/10.1016/j.est.2021.102990

[85] Y. F. Guo, K. Huang, and X. Y. Hu, "A state-of-health estimation method of lithium-ion batteries based on multi-feature extracted from constant current charging curve," *Journal of Energy Storage*, vol. 36, no. November 2020, p. 102372, 2021. [Online]. Available: https://doi.org/10.1016/j.est.2021.102372

[86] S. Saxena, C. Hendricks, and M. Pecht, "PL Sample CALCE Dataset," College Park, MD, USA, 2016. [Online]. Available: https://calce.umd.edu/data#PL

[87] W. He, N. Williard, M. Osterman, and M. Pecht, "CS2 Battery CALCE Dataset," College Park, MD, USA, 2011. [Online]. Available: https://calce.umd.edu/data#CS2

[88] J. Wu, L. Fang, J. Meng, M. Lin, and G. Dong, "Optimized multi-source fusion based state of health estimation for lithium-ion battery in fast charge applications," *IEEE Transactions on Energy Conversion*, vol. 8969, no. c, 2021.

[89] K. A. Severson, P. M. Attia, N. Jin, N. Perkins, B. Jiang, Z. Yang, M. H. Chen, M. Aykol, P. K. Herring, D. Fraggedakis, M. Z. Bazant, S. J. Harris, W. C. Chueh, and R. D. Braatz, "Data-driven prediction of battery cycle life before capacity degradation," *Nature Energy*, vol. 4, pp. 383–391, 2019. [Online]. Available: http://dx.doi.org/10.1038/s41560-019-0356-8

[90] Y. Ni, J. Xu, C. Zhu, and L. Pei, "Accurate residual capacity estimation of retired LiFePO4 batteries based on mechanism and data-driven model," *Applied Energy*, vol. 305, no. May 2021, p. 117922, 2022. [Online]. Available: https://doi.org/10.1016/j.apenergy.2021.117922

[91] P. Guo, Z. Cheng, and L. Yang, "A data-driven remaining capacity estimation approach for lithium-ion batteries based on charging health feature extraction," *Journal of Power Sources*, vol. 412, no. November 2018, pp. 442–450, 2019. [Online]. Available: https://doi.org/10.1016/j.jpowsour.2018.11.072

[92] B. Saha and K. Goebel, "Battery Data Set," Moffett Field, CA, 2007. [Online]. Available: https://ti.arc.nasa.gov/tech/dash/groups/pcoe/prognostic-data-repository/#battery

[93] M. Lin, D. Wu, J. Meng, J. Wu, and H. Wu, "A multi-feature-based multi-model fusion method for state of health estimation of lithium-ion batteries," *Journal of Power Sources*, vol. 518, no. August 2021, 2022.

[94] C. Birkl, "Oxford Battery Degradation Dataset 1," 2017. [Online]. Available: https://ora.ox.ac.uk/objects/uuid:03ba4b01-cfed-46d3-9b1a-7d4a7bdf6fac

[95] R. Xiong, J. Tian, H. Mu, and C. Wang, "A systematic model-based degradation behavior recognition and health monitoring method for lithium-ion batteries," *Applied Energy*, vol. 207, pp. 372–383, 2017. [Online]. Available: https://doi.org/10.1016/j.apenergy.2017.05.124

[96] X. Hu, H. Yuan, C. Zou, Z. Li, and L. Zhang, "Co-Estimation of State of Charge and State of Health for Lithium-Ion Batteries Based on Fractional-Order Calculus," *IEEE Transactions on Vehicular Technology*, vol. 67, no. 11, pp. 10 319–10 329, 2018.

[97] C. Zou, X. Hu, S. Dey, L. Zhang, and X. Tang, "Nonlinear Fractional-Order Estimator With Guaranteed Robustness and Stability for Lithium-Ion Batteries," *IEEE Transactions on Industrial Electronics*, vol. 65, no. 7, pp. 5951–5961, 2018.

[98] S. Buller, "Impedance-based simulation models for energy storage devices in advanced automotive power systems," Ph.D. dissertation, RWYH Aachen University, Aachen, 2003.

[99] B. Wang, S. E. Li, H. Peng, and Z. Liu, "Fractional-order modeling and parameter identification for lithium-ion batteries,"

Journal of Power Sources, vol. 293, pp. 151–161, 2015. [Online]. Available: http://dx.doi.org/10.1016/j.jpowsour.2015.05.059

[100] H. M. Barkholtz, A. Fresquez, B. R. Chalamala, and S. R. Ferreira, "Sandia National Laboratories Battery Cell Testing Data Archive," 2017. [Online]. Available: https://www.sandia.gov/energystorage safety-ssl/research-development/research-data-repository/

[101] Y. Ma, X. Zhou, B. Li, and H. Chen, "Fractional modeling and SOC estimation of lithium-ion battery," *IEEE/CAA Journal of Automatica Sinica*, vol. 3, no. 3, pp. 281–287, 2016.

[102] A. Nasser Eddine, B. Huard, J. D. Gabano, and T. Poinot, "Initialization of a fractional order identification algorithm applied for Lithium-ion battery modeling in time domain," *Communications in Nonlinear Science and Numerical Simulation*, vol. 59, pp. 375–386, 2018. [Online]. Available: https: //doi.org/10.1016/j.cnsns.2017.11.034

[103] A. Oustaloup, F. Levron, B. Mathieu, and F. M. Nanot, "Frequency-band complex noninteger differentiator: Characterization and synthesis," *IEEE Transactions on Circuits and Systems I: Fundamental Theory and Applications*, vol. 47, no. 1, pp. 25–39, 2000.

[104] I. Podlubny, *Fractional differential equations.* San Diego, California USA: Acadamic Press, 1999.

[105] L. Gagneur, A. L. Driemeyer-Franco, C. Forgez, and G. Friedrich, "Modeling of the diffusion phenomenon in a lithium-ion cell using frequency or time domain identification," *Microelectronics Reliability*, vol. 53, no. 6, pp. 784–796, 2013. [Online]. Available: http://dx.doi.org/10.1016/j.microrel.2013.03.009

[106] H. Ren, Y. Zhao, S. Chen, and L. Yang, "A comparative study of lumped equivalent circuit models of a lithium battery for state of charge prediction," *International Journal of Energy Research*, vol. 43, no. 13, pp. 7306–7315, 2019.

[107] P. Schröer, E. Khoshbakht, T. Nemeth, M. Kuipers, H. Zappen, and D. U. Sauer, "Adaptive modeling in the frequency and

time domain of high-power lithium titanate oxide cells in battery management systems," *Journal of Energy Storage*, vol. 32, no. October, 2020.

[108] Y. Zou, S. E. Li, B. Shao, and B. Wang, "State-space model with non-integer order derivatives for lithium-ion battery," *Applied Energy*, vol. 161, pp. 330–336, 2016. [Online]. Available: http://dx.doi.org/10.1016/j.apenergy.2015.10.025

[109] J. Baranowski, W. Bauer, M. Zagorowska, T. Dziwinski, and P. Piatek, "Time-domain Oustaloup approximation," *2015 20th International Conference on Methods and Models in Automation and Robotics, MMAR 2015*, pp. 116–120, 2015.

[110] S. Pooseh, R. Almeida, and D. F. Torres, "Discrete direct methods in the fractional calculus of variations," *Computers and Mathematics with Applications*, vol. 66, no. 5, pp. 668–676, 2013. [Online]. Available: http://dx.doi.org/10.1016/j.camwa.2013.01.045

[111] N. Maamri and J. C. Trigeassou, "A comparative analysis of two algorithms for the simulation of fractional differential equations," *International Journal of Dynamics and Control*, vol. 8, no. 1, pp. 302–311, 2019. [Online]. Available: https://doi.org/10.1007/s40435-019-00547-4

[112] I. Podlubny, "Mittag-Leffler function," 2012. [Online]. Available: https://www.mathworks.com/matlabcentral/fileexchange/8738-mittag-leffler-function

[113] Y. Wang, M. Li, and Z. Chen, "Experimental study of fractional-order models for lithium-ion battery and ultra-capacitor: Modeling, system identification, and validation," *Applied Energy*, vol. 278, no. December 2019, p. 115736, 2020. [Online]. Available: https://doi.org/10.1016/j.apenergy.2020.115736

[114] H. Dai, B. Jiang, and X. Wei, "Impedance characterization and modeling of lithium-ion batteries considering the internal temperature gradient," *Energies*, vol. 11, no. 1, 2018.

[115] Matlab, "particleswarm Documentation," accessed: 2021-06-25. [Online]. Available: https://it.mathworks.com/help/gads/particle-swarm-optimization-algorithm.html

[116] Z. Wei, G. Dong, X. Zhang, J. Pou, Z. Quan, and H. He, "Noise-immune model identification and state-of-charge estimation for lithium-ion battery using bilinear parameterization," *IEEE Transactions on Industrial Electronics*, vol. 68, no. 1, pp. 312–323, 2021.

[117] B. Bole, C. Kulkarni, and M. Daigle, "Randomized battery usage data set, nasa ames prognostics data repository," http://ti.arc.nasa.gov/project/prognostic-data-repository, 2014, "NASA Ames Research Center, Moffett Field, CA".

[118] T. Nemeth, P. Schröer, M. Kuipers, and D. U. Sauer, "Lithium titanate oxide battery cells for high-power automotive applications - electro-thermal properties, aging behavior and cost considerations," *Journal of Energy Storage*, vol. 31, p. 101656, 2020. [Online]. Available: https://www.sciencedirect.com/science/article/pii/S2352152X20314936

[119] R. W. Schafer, "What is a savitzky-golay filter? [lecture notes]," *IEEE Signal Processing Magazine*, vol. 28, no. 4, pp. 111–117, 2011.

[120] C. Turnes, "How does "smoothdata" function using "gaussian" method define the standard deviation for different window size?" 2018. [Online]. Available: https://it.mathworks.com/matlabcentral/answers/406563-how-does-smoothdata-function-using-gaussian-method-define-the-standard-deviation-for-different-w

[121] C. Birkl, "Oxford battery degradation dataset 1," 2017.

[122] ——, "Diagnosis and prognosis of degradation in lithium-ion batteries," Ph.D. dissertation, University of Oxford, 2017.

[123] M. Petit, E. Prada, and V. Sauvant-Moynot, "Development of an empirical aging model for li-ion batteries and application to assess the impact of vehicle-to-grid strategies on battery lifetime," *Applied Energy*, vol. 172, pp. 398–407, 2016. [Online]. Available: http://dx.doi.org/10.1016/j.apenergy.2016.03.119

[124] K. Uddin, T. Jackson, W. D. Widanage, G. Chouchelamane, P. A. Jennings, and J. Marco, "On the possibility of extending the lifetime of lithium-ion batteries through optimal v2g facilitated by an integrated vehicle and smart-grid system," *Energy*, vol. 133, pp. 710–722, 2017. [Online]. Available: https://www.sciencedirect.com/science/article/pii/S0360544217306825

[125] A. Barai, K. Uddin, W. D. Widanage, A. McGordon, and P. Jennings, "A study of the influence of measurement timescale on internal resistance characterisation methodologies for lithium-ion cells," *Scientific Reports*, vol. 8, no. 1, pp. 1–13, 2018. [Online]. Available: http://dx.doi.org/10.1038/s41598-017-18424-5

[126] Dataset TOYOTA. [Online]. Available: https://data.matr.io/1/

[127] ST-Microelectronics, "L9963e: Automotive chip for battery management applications with daisy chain up to 31 devices," 2021, accessed: 7th June 2021. [Online]. Available: https://www.st.com/en/automotive-analog-and-power/l9963e.html

[128] X. Li, C. Yuan, and Z. Wang, "Multi-time-scale framework for prognostic health condition of lithium battery using modified Gaussian process regression and nonlinear regression," *Journal of Power Sources*, vol. 467, no. May, p. 228358, 2020. [Online]. Available: https://doi.org/10.1016/j.jpowsour.2020.228358

[129] A. Guarino, W. Zamboni, and E. Monmasson, "A battery residual capacity indicator based on the battery internal resistance: An experimental study," *Proceedings - 2020 2nd IEEE International Conference on Industrial Electronics for Sustainable Energy Systems, IESES 2020*, pp. 15–20, 2020.

[130] T. Hastie, R. Tibshirani, and J. Friedman, *The Elements of Statistical Learning*, 2nd ed. Stanford, CA, USA: Springer, 2009.

[131] D. A. Belsley, E. Kuh, and R. E. Welsch, *Regression diagnostics - identifying influential data and sources of collinearity.* Hoboken, NJ, USA: John Wiley & Sons, 1980.

[132] T. Hastie, R. Tibshirani, G. James, and D. Witten, *An introduction to statistical learning*, 2nd ed. New York, NY, USA: Springer, 2021.